Fall 12-10-2019

# Dark Matter Production Beyond the Thermal WIMP Paradigm: an exploration of early matter domination scenarios

Jacek Ksawery Osinski
*University of New Mexico*

Jacek Ksawery Osiński

*Candidate*

Physics and Astronomy

*Department*

This dissertation is approved, and it is acceptable in quality and form for publication:

*Approved by the Dissertation Committee:*

Rouzbeh Allahverdi , Chairperson

Dinesh Loomba

James Dent

Huaiyu Duan

Akimasa Miyake

# Dark Matter Production Beyond the Thermal WIMP Paradigm: an exploration of early matter domination scenarios

by

**Jacek Ksawery Osiński**

B.S., Astrophysics, University of New Mexico, 2013
M.S., Physics, University of New Mexico, 2016

DISSERTATION

Submitted in Partial Fulfillment of the
Requirements for the Degree of

Doctor of Philosophy
Physics

The University of New Mexico

Albuquerque, New Mexico

May, 2020

# Dedication

*For my family*

# Acknowledgments

Upon completion of the degree related to this dissertation, I will have been at UNM PandA for 12 years, spread across three degrees. In that time, I have interacted with many people and would like to thank all of them for their unique contributions to our department and to my experience in it.

Specific to this dissertation, I would like to thank my advisor, Rouzbeh Allahverdi, for guiding my research these past few years; my committee, Rouzbeh, Dinesh Loomba, James Dent, Huaiyu Duan, and Akimasa Miyake, for reading this document and hopefully providing useful comments (and Sudhakar Prasad who served on my candidacy committee); Ylva Pihlström, Director of the Campus Observatory, who let me use the observatory computers for my numerical calculations - the work that went into this dissertation would otherwise have taken at least five to seven times longer; Michael Graesser and the T2 group at Los Alamos National Laboratory for hosting me during my six month DOE SCGSR program there; Patrick Brown, who's undergraduate thesis treated the continuous distribution scenarios mentioned in the concluding chapter - we hope to continue this work in the coming months; and Alisa Gibson, Steve Portillo, Gary Harrison, Sandra Ortiz, Michael Martinez, Tom Hess, Julie Morrison, Leanne Yanabu, and all of the current and past PandA staff members for keeping our department running.

Throughout my graduate studies, I have been funded by various sources which I will acknowledge here: my Research Assistanships with Rouzbeh through the National Science Foundation Grant No. PHY-1720174; my time at LANL through the U. S. Department of Energy, Office of Science, Office of Workforce Development for Teachers and Scientists, Office of Science Graduate Student Research (SCGSR) program - the SCGSR program is administered by the Oak Ridge Institute for Science and Education (ORISE) for the DOE - ORISE is managed by ORAU under contract number DE-SC0014664; and many Teaching Assistantships from the UNM Department of Physics and Astronomy (often working with Rich Rand) which have supported me for the majority of my time as a graduate student.

Finally, I would especially like to thank my family and friends for being helpful, supportive, and reasonable human beings.

# Dark Matter Production Beyond the Thermal WIMP Paradigm: an exploration of early matter domination scenarios

by

**Jacek Ksawery Osiński**

B.S., Astrophysics, University of New Mexico, 2013
M.S., Physics, University of New Mexico, 2016

Ph.D., Physics, University of New Mexico, 2020

## Abstract

In the standard thermal history of the Universe, the energy density is dominated by radiation throughout the postinflationary era, until matter-radiation equality after big bang nucleosynthesis (BBN). However, we currently do not have any observational probes of the pre-BBN period, and radiation domination (RD) is therefore an assumption. Generic early Universe models predict the presence of additional components in the postinflationary Universe which can lead to periods of nonstandard evolution before the onset of BBN. A prominent example of such a period is a phase of early matter domination (EMD) in which the Universe undergoes matter-dominated

expansion for a time, before transitioning to the standard RD phase. The pre-BBN era is additionally the natural time for the production of dark matter (DM), which is a necessary component for the later evolution of the Universe. Furthermore, the production of DM is highly sensitive to the thermal history of the Universe, and can therefore serve as a probe of the pre-BBN era as ongoing and future searches continue to explore the DM parameter space. As a consequence of current searches, the prevailing scenario, in which weakly interacting massive particles (WIMPs) are thermally produced in the standard thermal history, is coming under increasing pressure. In this dissertation, we will study DM production beyond the thermal WIMP paradigm, focusing on the effects of EMD eras in the pre-BBN Universe.

# Contents

**List of Figures** **xi**

**Abbreviations** **xvii**

**1 Introduction** **1**

1.1 Dark matter and thermal history overview . . . . . 1

1.2 Cosmological preliminaries . . . . . 3

1.3 Freeze-out during radiation domination . . . . . 4

1.4 Freeze-in during radiation domination . . . . . 8

1.5 Summary . . . . . 9

**2 Dark Matter Production in Early Matter Domination** **11**

2.1 Freeze-out during standard early matter domination . . . . . 14

2.2 Freeze-in during standard early matter domination . . . . . 14

2.3 Summary . . . . . 15

**3 Dark Matter Production in Two-Field Early Matter Domination** **17**

3.1 Introduction . . . . . 17

3.2 The two-field scenario of early matter domination . . . . . 18

3.3 Dark matter production in the two-field scenario . . . . . 22

3.4 Results . . . . . 24

3.5 Discussion and conclusion . . . . . 29

**4 Dark Matter Production Prior to Early Matter Domination 31**

4.1 Introduction . . . . . 31

4.2 Dark matter abundance in the freeze-in scenario . . . . . 33

4.2.1 The standard lore . . . . . 34

4.2.2 Production prior to early matter domination . . . . . 35

4.3 Results . . . . . 39

4.4 Early-equilibrium regime: a closer look . . . . . 44

4.4.1 Connection to observables . . . . . 46

4.4.2 An example . . . . . 48

4.5 Discussion and conclusion . . . . . 49

**5 Nonthermal Dark Matter from Primordial Black Holes 52**

5.1 Introduction . . . . . 52

5.2 PBH formation in early matter domination . . . . . 54

5.3 Nonthermal dark matter production from PBH evaporation . . . . . 57

5.4 Results . . . . . 60

5.5 Discussion and conclusion . . . . . 63

**6 Topological Dark Matter Involving Early Matter Domination 66**

6.1 Introduction . . . . . 66

6.2 Monopole production involving early matter domination - part 1 . . . 68

6.3 A thermal history interlude . . . . . 70

6.4 Monopole production involving early matter domination - part 2 . . . 72

6.5 Early matter domination by a modulus . . . . . 79

6.6 Early matter domination by a heavy decoupled particle . . . . . 84

6.7 Discussion and conclusion . . . . . 91

**7 Conclusion 93**

7.1 Summary . . . . . 93

7.2 Future work . . . . . 95

**A Additional Introductory Material 98**

A.1 Freeze-in during RD and standard EMD . . . . . 98

A.2 Regimes of $\langle \sigma_{\rm ann} v \rangle_{\rm f}$ for freeze-out/in during RD and standard EMD . 102

A.3 EMD from an oscillating scalar . . . . . 103

A.4 Relativistic degrees of freedom . . . . . 106

**B Additional Details for Chapter 3 107**

B.1 Temperature during the transition regime . . . . . 107

B.2 Freeze-in during the transition regime . . . . . 109

**C Additional Details for Chapter 4** **111**

C.1 Regimes of pre-EMD freeze-in production . . . . . 111

**D Additional Details for Chapter 5** **115**

D.1 Number of relevant $e$-folds . . . . . 115

D.2 Integrating over PBHs in an extended mass range . . . . . 116

**E Additional Details for Chapter 6** **118**

E.1 The factors $f_{\mathrm{R}}$ and $e_{\mathrm{f}}$ . . . . . 118

E.2 Decoupling of $\Phi$ from either sector via freeze-out . . . . . 119

E.3 Decoupling of $\Phi$ from either sector via freeze-in . . . . . 121

E.4 Additional parameter constraints for decoupled $\Phi$ . . . . . 122

**References** **124**

# List of Figures

1.1 Analytical approximations for freeze-out (right/blue) and freeze-in (left/red) production of DM in RD from Eqs. (1.11) and (1.12) respectively. The horizontal dashed line marks $\Omega_\chi h^2 = 0.12$, while the vertical dashed line marks the nominal WIMP annihilation rate of $\langle \sigma_{\rm ann} v \rangle_{\rm f} = 3 \times 10^{-26}\,{\rm cm}^3\,{\rm s}^{-1}$. . . . . 9

2.1 Analytical approximations for freeze-out (right) and freeze-in (left) production of DM in standard EMD from Eqs. (2.6) and (2.7) respectively, with DM mass $m_\chi = 100\,{\rm GeV}$. The top two lines correspond to a reheat temperature of $T_{\rm R} = 10\,{\rm GeV}$, while the bottom two correspond to $T_{\rm R} = 1\,{\rm GeV}$. The horizontal and vertical dashed lines are as in Figure 1.1. . . . . 15

3.1 Evolution of the energy density of the dominant field $\phi$ (purple/top), the subdominant field $\varphi$ (red/middle), and radiation (green/bottom) in a two-field scenario with $f = 10^{-4}$, $\alpha = 10^8$, and $T_{\rm R} = 10$ GeV. Regions 1, 2, and 3 correspond to the two-field, transition, and single-field regimes respectively. The dashed line that extrapolates region 3 denotes the single-field scenario with the same $T_{\rm R}$. . . . . 21

3.2 Evolution of the temperature in the two-field scenario of Figure 3.1. The temperature is enhanced by a factor of $(\alpha f)^{1/4} \approx 10$ in region 1, approaches that of the single-field scenario in region 2, and coincides with it in region 3. . . . . 21

3.3 Curves represent points in the $m_\chi - \langle\sigma_{\rm ann} v\rangle_{\rm f}$ plane where the two-field scenario yields the correct DM abundance. We have chosen $\alpha = 10^8$ and varied $f$ between $10^{-2}$ (pink/top) and $f = 10^{-5}$ (blue/bottom) in this figure. The single-field scenario is shown at the very bottom for comparison. The left (right) panel corresponds to $T_{\rm R} = 10$ GeV ($T_{\rm R} = 1$ GeV). The DM abundance is set during the two-field regime, transition regime, and single-field regime in regions 1, 2, and 3 respectively. The left and right sides of the curves correspond to freeze-in and freeze-out production respectively. . . . . 26

3.4 The same as Figure 3.3, but we have chosen $f = 10^{-4}$ and varied $\alpha$ between $10^8$ (blue/top) and $10^5$ (cyan/bottom) in this figure. . . . . 26

4.1 Temperature of the Universe as a function of the Hubble expansion rate showing the postinflationary history we are considering. The curve begins at the top left corner, when $H \approx H_{\rm reh}$, with an early period of RD. The EMD period lasts from $H \approx H_0$ to $H \approx H_{\rm R}$, with $H_{\rm tran} \lesssim H \lesssim H_0$ corresponding to the memory phase, and $H_{\rm R} \lesssim H \lesssim H_{\rm tran}$ to the entropy-producing phase. The Universe returns to a RD phase after the end of EMD, where $H < H_{\rm R}$. . . . 37

4.2 Values of $m_\chi$ and $\langle\sigma_{\rm ann}v\rangle_{\rm f}$ that yield the DM relic abundance of $\Omega_\chi h^2 \approx 0.12$, obtained by numerical solution of the Boltzmann equations in Eq. (4.8). The solid curve corresponds to production during the entire thermal history shown in Figure 4.1, while the dashed curve depicts the freeze-in side of the corresponding baseline curve from production in the entropy-generating phase of EMD alone. In region 1, the DM relic abundance is dominated by the late EMD contribution, while the early-equilibrium and decoupling regimes of the pre-EMD contribution dominate in regions 2 and 3, respectively. The transition to freeze-out of the baseline curve is seen to begin at the top-right corner. . . . . 40

4.3 Variation of the curve from Figure 4.2 for different values of $T_{\rm R}$ and $T_0$. Left: variation of $T_0$ for constant $T_{\rm reh}$ and $T_{\rm R}$. Right: variation of $T_{\rm R}$ for constant $T_{\rm reh}$ and $T_0$. Note the appearance of the freeze-out side, at the top right corner, which merges with the peak of the corresponding baseline curve. . . . . 41

4.4 Variation of the curve from Figure 4.2 for different values of $T_{\rm reh}$ while holding $T_{\rm R}$ and $T_0$ constant. . . . . 42

4.5 Variation of $T_{\rm R}$, with constant $T_{\rm reh}$ and $T_0$, for values that display the transition between the horizontal gap and vertical gap behavior described in the text. For the larger two values of $T_{\rm R}$, the solid curves are separated into a freeze-in part on the left and a freeze-out part on the right (which we do not show apart from the top right corner). For the two smaller values, the curves are split into a lower part that follows the baseline curve and an upper part that connects the freeze-in and freeze-out sides. . . . . 44

4.6 Contours of the upper bound on $m_\chi$ in the $T_0 - T_\mathrm{R}$ plane, in order to not overproduce DM in the early-equilibrium regime. The solid lines are obtained numerically from region 2 shown in previous figures, while the thin lines correspond to Eq. (4.9). . . . . 45

4.7 Upper bound on the DM mass $m_\chi$ for a given modulus mass $m_\phi$ in the case of modulus-driven EMD. The curve is obtained numerically from the early-equilibrium regime. . . . . 49

5.1 The solid line corresponds to the theoretical expression for $\beta(M_\mathrm{max})$ from Eq. (5.2) as a function of the enhancement factor $f_\mathrm{enh}$ in the scalar power spectrum at scales relevant for PBH formation. The shaded band shows the observational constraint on $\beta(M_\mathrm{max})$ from Eq. (5.14) for $\mathrm{Br}_\chi = 1$ in the mass range $m_\chi = 100\,\mathrm{GeV} - 1\,\mathrm{TeV}$ (left), and $m_\chi = 1\,\mathrm{TeV}$ with branching fraction between $\mathrm{Br}_\chi = 10^{-2} - 1$ (right). Larger values of $m_\chi$ or $\mathrm{Br}_\chi$ extend the band toward smaller values of $\beta$. . . . . 61

5.2 The shaded band in the $\alpha_\mathrm{s} - \beta_\mathrm{s}$ plane corresponds to the intersection region in the left panel of Figure 5.1. The 68% confidence ellipse from Planck 2015 [146] on the running of the scalar spectral index is outlined by the red dashed line. . . . . 62

6.1 Numerical evolution of the background energy density components with scale factor. EMD begins once $\rho_\Phi$ dominates over both radiation components, and lasts until $\Phi$ decays. Top panel: initial RD by the HS. Bottom panel: initial RD by the VS. . . . . 81

6.2 Solid curves are obtained from numerical evolution of the background while dashed lines are analytical. The red dashed line in all panels marks the purely RD equivalent scenario. Black dashed lines indicate production at the start and end of EMD. Solid blue curves correspond to (from top to bottom in each panel): $\Phi_{\rm i} = 10^{-3} M_{\rm P}$, $10^{-2} M_{\rm P}$, and $10^{-1} M_{\rm P}$ (top panels); $T_{\rm R}^{(\rm vis)} = 10^5\,{\rm GeV}$, $10^4\,{\rm GeV}$, and $10^3\,{\rm GeV}$ (middle panels); $\nu = \mu = 0.5$ and 1 (bottom panels). Left panels: initial RD by the HS. Right panels: initial RD by the VS. . . . . 83

6.3 Diagram of particle $\Phi$ decoupling from either sector while always reheating to the VS. . . . . 85

6.4 Background energy densities vs scale factor in the case of EMD by a decoupled particle. Values of $\langle \sigma_\Phi v \rangle$ are chosen to correspond to relativistic freeze-out, thus yielding the longest possible EMD phase in each panel. Left panels: initial RD by the HS. Right panels: initial RD by the VS. Top panels: $\Phi$ decoupling from the dominant sector. Bottom panels: $\Phi$ decoupling from the subdominant sector. . . . . 86

6.5 As in Figure 6.2: solid curves are obtained from numerical evolution of the background, while dashed lines are analytical. The red dashed line in all panels marks the purely RD equivalent scenario. Black dashed lines indicate production at the start and end of EMD. Solid curves correspond to (from top to bottom in each panel): $\langle\sigma_\Phi v\rangle = 10^{-31}\,\mathrm{GeV}^{-2}$, $10^{-25}\,\mathrm{GeV}^{-2}$, and $10^{-28}\,\mathrm{GeV}^{-2}$ (top panels); $\langle\sigma_\Phi v\rangle = 10^{-24}\,\mathrm{GeV}^{-2}$ and $10^{-26.5}\,\mathrm{GeV}^{-2}$ (bottom panels). Left panels: initial RD by the HS. Right panels: initial RD by the VS. Top panels: $\Phi$ decoupling from the dominant sector. Bottom panels: $\Phi$ decoupling from the subdominant sector. The curves with the largest monopole mass correspond to relativistic freeze-out of $\Phi$ in each panel. The dependence on $T_{\mathrm{R}}^{(\mathrm{vis})}$ and the critical exponents $\nu$ and $\mu$ is the same as in Figure 6.2. . . . . 90

A.1 Numerical evolution of the energy density in a scalar field as it begins to oscillate. The oscillating curve corresponds to the energy density of the scalar field in all panels, while the other curve depicts the radiation energy density. Top Panels show the onset of oscillation and matter-like redshift of the field in detail. Bottom panels show the entire evolution through eventual decay for the same parameters. Left panels correspond to a Planckian initial amplitude, while in the right panels it is smaller. . . . . 105

A.2 Relativistic degrees of freedom in the SM, $g_*(T)$ as a function of temperature. . . . . 106

# Abbreviations

| | |
|---|---|
| BBN | big bang nucleosynthesis |
| CMB | cosmic microwave background |
| DM | dark matter |
| EMD | early matter domination |
| HS | hidden sector |
| lhs | left-hand side on an equation |
| MD | matter domination |
| PBH | primordial black hole |
| RD | radiation domination |
| rhs | right-hand side of an equation |
| SM | standard model of particle physics |
| VS | visible sector |
| WIMP | weakly interacting massive particle |

# Chapter 1

# Introduction

## 1.1 Dark matter and thermal history overview

In our current understanding of the Universe, dark matter (DM) makes up about 85% of all matter. While the standard cosmological model is quite successful in explaining cosmological observations, the identity and properties of DM, one of its main ingredients, are completely unknown. The existence of DM is supported by various observations and the identification of its properties has long been the focus of many theoretical, observational, and experimental investigations (see [1] for a review, and [2] for a historical perspective). In the absence of discovery, a wealth of possible DM candidates has emerged, spanning many orders of magnitude in DM mass, from $10^{-5}\,\mathrm{eV}$ for typical axion models, all the way up to $100\,M_\odot \approx 10^{57}\,\mathrm{eV}$ in the heaviest primordial black hole scenarios [2, 3].[1] Though the possibility of primordial black holes constituting the majority of DM has seen a significant increase in interest with the recent advent of gravitational wave astronomy, most DM candidates are a proposed new type of particle beyond the standard model of particle physics (SM).

[1] Even masses as low as $10^{-22}\,\mathrm{eV}$ are sometimes considered as the lightest possible DM mass [4].

One of the most promising classes of DM candidates is weakly interacting massive particles (WIMPs), which have long been the focus of major direct, indirect, and collider searches, and have guided many theoretical investigations concerning the origin of DM [5]. The mass of such particles is typically within 10-1000 GeV, and they annihilate with a weak-scale rate near $\langle \sigma_{\rm ann} v \rangle \approx 10^{-26}\,{\rm cm}^3\,{\rm s}^{-1}$, where we have used the usual parameterization of the annihilation rate as the thermally averaged product of the annihilation cross-section and relative particle velocity [5, 6].

Analysis of the cosmic microwave background (CMB) power spectrum as well as the details of big bang nucleosynthesis (BBN) indicate that DM was already the dominant form of matter at these two epochs [7, 8]. This suggests that its abundance was established prior to the start of BBN, when the Universe was less than 1 second old. However, as with the properties of DM itself, this period is beyond the reach of current observations. Along with primordial gravitational waves from inflation and their imprints on the CMB, DM can provide a useful probe of the pre-BBN Universe through the mechanisms which produce it. As we will see in detail in the next section and in Chapter 2, DM production is strongly dependent on the thermal history of the early Universe, which can be characterized as the relation between the temperature of the universe $T$ and the Hubble expansion rate $H$.

In the standard thermal history of the Universe, the energy density prior to BBN, when the temperature of the Universe is much greater than MeV, is assumed to be dominated by radiation (i.e. relativistic particles). This is a natural assumption because the era of inflation typically ends with a period of "reheating" where the decay of the inflaton populates the Universe with a large amount of radiation. Furthermore, radiation domination (RD) is necessary during BBN in order to get the right elemental abundances (the key parameter of BBN is the baryon-to-photon ratio, which is on the order of $10^{-10}$ [8]). This standard assumption of RD, along with the added assumption of thermal equilibrium among relativistic particle species of interest, accommodates a production mechanism know as thermal freeze-out that is

largely responsible for the success of WIMPs as a DM candidate. As we will see in the next section, thermal freeze-out of particles which annihilate with a weak-scale rate in a RD Universe before BBN leads to the correct relic abundance of DM observed today for a range of DM masses of about five orders of magnitude [5]. This is referred to as the "WIMP miracle" and has motivated many searches for WIMP-like DM.

We will next review the standard freeze-out production mechanism in detail, as well as mention a typical deviation from it.

## 1.2 Cosmological preliminaries

We will begin with a brief overview of the relevant cosmology that we will need for further calculations. Assuming the standard Friedmann-Lemaître-Robertson-Walker metric based on homogeneity and isotropy, the Einstein equations lead to a simple equation governing the expansion of the Universe. Neglecting spatial curvature (current observations indicate a nearly flat Universe [9]) and dark energy (which is subdominant in the early Universe even though it is dominant today), this equation takes the form

$$3H^2 M_{\rm P}^2 = \rho_{\rm tot} \tag{1.1}$$

where the Hubble expansion rate $H$ is defined in relation to the scale factor of the Universe $a$ by $aH \equiv da/dt$, $\rho_{\rm tot}$ is the total energy density in the Universe, and $M_{\rm P} \approx 2.4 \times 10^{18}\,\text{GeV}$ is the reduced Planck mass [2]. We see that the expansion of the Universe is determined by the dominant form of energy density, which can itself change with time. The energy density of radiation decreases as $\rho_{\rm r} \propto a^{-4}$ (three powers for volume expansion, one for energy redshift), while that of matter decreases as $\rho_{\rm m} \propto a^{-3}$, resulting in different expansion rates if either of these is dominant. In

[2]Throughout this dissertation, we will adopt "natural units" where $c = \hbar = k_{\rm B} = 1$. The remaining unit that will describe the size of most quantities presented will be GeV.

RD we have $H \propto a^{-2}$, and in MD we have $H \propto a^{-3/2}$. From the definition of $H$, we can also express the expansion rate in terms of time as $H = 1/(2t)$ in RD, and $H = 2/(3t)$ in MD. Finally, we note that the value of the scale factor today is defined to be equal to one.

The temperature of the Universe is defined in terms of the radiation energy density through

$$\rho_{\rm r} = \frac{\pi^2}{30} g_* T^4 \tag{1.2}$$

where $g_*$ tracks the number of relativistic degrees of freedom and is thus a function of temperature itself. In the early Universe, when temperatures are high and essentially all SM particles are relativistic and in thermal equilibrium, we need only track one temperature, and $g_*$ is given by [3]

$$g_* = \sum \left( g_{\rm B} + \frac{7}{8} g_{\rm F} \right) \tag{1.3}$$

where the sum is over all relativistic particle species, B denotes bosons, and F fermions. For numerical calculations, we will use a continuous function for $g_*(T)$ shown in Appendix A. Using Eqs. (1.1) and (1.2), we can obtain the relation between temperature and expansion rate during a period of RD:

$$H^{(\rm RD)} = \left( \frac{\pi^2}{90} g_* \right)^{1/2} \frac{T^2}{M_{\rm P}} \,. \tag{1.4}$$

## 1.3 Freeze-out during radiation domination

We will now consider DM production in a RD Universe via thermal freeze-out, which is the standard production mechanism for WIMPs. In general, the evolution of the number density of a particle species $\chi$ whose number can be changed by annihilations and pair production in the presence of an expanding background can be described

[3] To account for different temperatures, each $g$ factor should be accompanied by $(T_i/T)^4$.

by the Boltzmann equation (see [10] for details):

$$\frac{dn_\chi}{dt} + 3Hn_\chi = \langle\sigma_{\rm ann}v\rangle \left(n_{\chi,\rm eq}^2 - n_\chi^2\right) \,, \tag{1.5}$$

where the term involving $H$ accounts for expansion and the right-hand side (rhs) describes the coupling to the thermal bath through all annihilation channels. The total annihilation rate is parameterized by the thermally averaged product of the annihilation cross-section and relative particle velocity $\langle\sigma_{\rm ann}v\rangle$, which we will typically assume to be independent of temperature.[4] The equilibrium number density is given by the integral over the distribution function

$$n_{\chi,\rm eq} = \frac{g_\chi}{2\pi^2}\int_{m_\chi}^\infty \frac{\sqrt{E^2-m_\chi^2}}{e^{E/T}\pm 1}EdE \tag{1.6}$$

where $g_\chi$ counts the internal degrees of freedom, the plus is for fermions, and the minus is for bosons. In the relativistic ($m_\chi \ll T$) and nonrelativistic ($m_\chi \gg T$) limits, the equilibrium number density becomes

$$n_{\chi,\rm eq} = \begin{cases} \dfrac{\zeta(3)}{\pi^2}g_\chi T^3 & m_\chi \ll T, \quad \text{bosons} \\ \dfrac{3\zeta(3)}{4\pi^2}g_\chi T^3 & m_\chi \ll T, \quad \text{fermions} \\ g_\chi\left(\dfrac{m_\chi T}{2\pi}\right)^{3/2} e^{-m_\chi/T} & m_\chi \gg T \end{cases} \tag{1.7}$$

where $\zeta(3)$ is the Riemann zeta function of 3. For simplicity, we will often use the expression for bosons when discussing generic relativistic DM particles because the fermionic factor of 3/4 hardly causes any changes in our results.

We will initially assume the annihilation rate is strong enough to bring DM particles into thermal equilibrium with the relativistic background, resulting in an equilibrium number density that dilutes as $n_\chi \propto a^{-3}$, as expected. This means that the annihilation rate $\Gamma_{\rm ann} = n_{\chi,\rm eq}\langle\sigma_{\rm ann}v\rangle$, which governs the interactions that keep $\chi$ in equilibrium, is greater than the Hubble expansion rate $H$. If equilibrium is

[4]Discussions of the effects of including temperature dependence will be included in subsequent chapters when relevant.

maintained while the particles are nonrelativistic, the exponential factor will quickly result in a very small relic abundance and we are therefore interested in the case where $T \gtrsim m_\chi$ in order to be left with a sizable amount of DM. As the Universe expands, the annihilation rate decreases as $\Gamma_{\rm ann} \propto a^{-3}$ for relativistic particles (and exponentially for nonrelativistic), while the Hubble rate in a RD Universe decreases as $H \propto a^{-2}$. Eventually, the annihilation rate will drop below the expansion rate and the number-changing interactions will become inefficient compared to expansion. The number density is then "frozen" and only changes due to redshift (which is another name for the dilution due to expansion). This happens when $n_{\chi,\rm eq}(T_{\rm f}) \langle\sigma_{\rm ann} v\rangle_{\rm f} = H(T_{\rm f})$, where $T_{\rm f}$ marks the freeze-out temperature. We have included a subscript 'f' on the annihilation rate to indicate its value at the freeze-out temperature in the case that it has temperature dependence.

The production of a cold nonrelativistic relic abundance corresponds to taking the nonrelativistic expression of the equilibrium number density at $T = T_{\rm f}$. Using this along with $H(T)$ during RD yields an expression that can be solved for $T_{\rm f}$:

$$x_{\rm f} = \ln\left(\frac{3\sqrt{5} g_\chi}{2\pi^{5/2} g_{*\rm f}^{1/2}} \langle\sigma_{\rm ann} v\rangle_{\rm f} M_{\rm P} m_\chi x_{\rm f}^{1/2}\right) \tag{1.8}$$

where $x_{\rm f} \equiv m_\chi / T_{\rm f}$, and $g_{*\rm f}$ is the value of $g_*$ at $T = T_{\rm f}$. [5] Note that this expression in general has two solutions, though only one of them corresponds to the nonrelativistic case of $x_{\rm f} > 1$. Typical values of $x_{\rm f}$ are around a few tens [6].

A useful quantity in calculating today's abundance is the entropy density, which is given by [6]

$$s = \frac{2\pi^2}{45} h_* T^3 \tag{1.9}$$

and is conserved in a comoving volume (if there are no significant sources of entropy

[5] Whenever $g_*$ appears with an additional subscript, that will indicate its value at the corresponding temperature.

[6] To be precise, the number of relativistic degrees of freedom for entropy $h_*$ can slightly differ from that for energy density $g_*$, but at high temperatures they are essentially the same and the difference at low temperatures is quite small [10, 11].

such as particle decays) [10]. Because both number and entropy density redshift as $a^{-3}$, their ratio remains constant apart from small changes due to the temperature dependence of the relativistic degrees of freedom. We can therefore obtain the relic abundance to a very good approximation by considering $n_\chi/s$ at the time of freeze-out.

The standard way to express the DM abundance is as $\Omega_\chi h^2$, where $\Omega_\chi \equiv \rho_\chi/\rho_\mathrm{c}$ is the ratio of the DM energy density to the critical energy density $\rho_\mathrm{c} = 3H_0^2 M_\mathrm{P}^2$ (the density that results in a flat Universe), and $h \equiv H_0/(100\,\mathrm{km\,s^{-1}\,Mpc^{-1}})$ is the reduced Hubble constant. This abundance can be related to $n_\chi/s$ through

$$\Omega_\chi h^2 = \frac{4h_{*0}m_\chi}{3g_{*0}T_0}\left(\frac{n_\chi}{s}\right)_\mathrm{f}\Omega_\mathrm{r}h^2 \tag{1.10}$$

where the present values of the various quantities are $g_{*0} = 3.36$, $h_{*0} = 3.9$, $T_0 \approx 2.73\,\mathrm{K} = 2.35\times10^{-13}\,\mathrm{GeV}$, and $\Omega_\mathrm{r}h^2 = 4.27\times10^{-5}$ [9, 11]. Choosing some typical values of the parameters, we get

$$\left(\Omega_\chi h^2\right)^{(\mathrm{RD})}_{\text{freeze-out}} = 0.096\left(\frac{x_\mathrm{f}}{25}\right)\left(\frac{80}{g_{*\mathrm{f}}}\right)^{1/2}\left(\frac{3\times10^{-26}\,\mathrm{cm^3\,s^{-1}}}{\langle\sigma_\mathrm{ann}v\rangle_\mathrm{f}}\right) \tag{1.11}$$

which is about a factor of 1.2 below the observed value of $\Omega_\chi h^2 \approx 0.12$ [9] for the particular values chosen. Note that the freeze-out abundance is inversely proportional to $\langle\sigma_\mathrm{ann}v\rangle_\mathrm{f}$. Stronger interactions therefore result in a later decoupling, and a smaller abundance as we track along the exponentially suppressed equilibrium number density. Various forms of this calculation exist, with different normalizations, but the important point is that the typical rates needed to reproduce the observed value are of the order of the weak interaction strength [1, 5, 6, 12]. A particle with mass within a few orders of magnitude of 100 GeV, with a weak-scale annihilation rate can then account for the observed DM abundance through the natural production mechanism of particle decoupling.

However, as DM searches continue, the parameter space for WIMP DM is coming under increasing pressure. For example, Fermi-LAT's results from observations of

dwarf spheroidal galaxies [13] and newly discovered Milky Way satellites [14] have placed upper bounds on the annihilation rate that are below the nominal WIMP value for certain annihilation products. Based on these results, a recent analysis has ruled out thermal DM with a mass below 20 GeV in a model-independent way (unless there is P-wave annihilation or co-annihilation) [15]. For specific annihilation channels, thermal DM with a mass up to 100 GeV can be excluded. Such pressure motivates a departure from the thermal WIMP paradigm, particularly from the weak-scale value of the annihilation rate. If the DM annihilation rate is significantly smaller than that of a typical WIMP, the approximation of thermal equilibrium may not hold and DM production proceeds via a process known as freeze-in rather than the standard freeze-out.

## 1.4 Freeze-in during radiation domination

If $\langle \sigma_{\rm ann} v \rangle_{\rm f}$ is much weaker than the weak scale, such that the pair production rate cannot bring the DM particles into thermal equilibrium with radiation, the DM abundance can still be obtained through a process called "freeze-in." The calculation of freeze-in abundances is a bit more involved than for freeze-out, and we therefore include the details in Appendix A.

While freeze-out production occurs when the temperature is near the DM mass, freeze-in production during RD peaks at the highest temperature. The temperature at the beginning of RD therefore sets the DM abundance in this case. In the standard thermal history, this temperature is established by inflationary reheating and can be much larger than typical WIMP masses. The relic abundance from freeze-in is given by (derived in Appendix A)

$$\left(\Omega_\chi h^2\right)^{\rm (RD)}_{\text{freeze-in}} \approx \frac{117\, g_\chi^2}{g_{*\rm f}^{1/4}\, g_{*\rm reh}^{5/4}} \left(\frac{T_{\rm reh}}{10^{10}\,{\rm GeV}}\right) \left(\frac{m_\chi}{100\,{\rm GeV}}\right) \left(\frac{\langle \sigma_{\rm ann} v \rangle_{\rm reh}}{2\times 10^{-53}\,{\rm cm}^3\,{\rm s}^{-1}}\right) , \quad (1.12)$$

where we have taken the initial time to correspond to the end of inflationary reheat-

ing, and $g_{*\mathrm{f}}$ indicates its value once the DM number density is frozen shortly after. For the values chosen in each term, this yields the correct relic abundance of DM.

An important distinction between freeze-out and freeze-in production is the dependence on the annihilation rate. While stronger rates decrease the final abundance for freeze-out, freeze-in results in a larger abundance as pair production becomes more efficient. Theses two regimes merge once $\langle\sigma_{\mathrm{ann}}v\rangle_{\mathrm{f}}$ is sufficiently large to bring $\chi$ into thermal equilibrium, but not so large that they enter the nonrelativistic regime while still in equilibrium. The two expressions in Eqs. (1.11) and (1.12) are shown in Figure 1.1 as a function of $\langle\sigma_{\mathrm{ann}}v\rangle_{\mathrm{f}}$ using typical values of the other parameters.

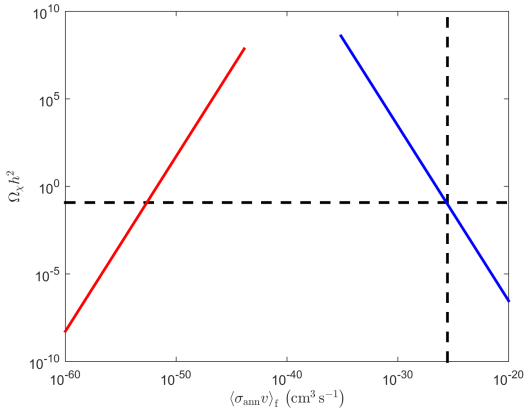


Figure 1.1: Analytical approximations for freeze-out (right/blue) and freeze-in (left/red) production of DM in RD from Eqs. (1.11) and (1.12) respectively. The horizontal dashed line marks $\Omega_\chi h^2 = 0.12$, while the vertical dashed line marks the nominal WIMP annihilation rate of $\langle\sigma_{\mathrm{ann}}v\rangle_{\mathrm{f}} = 3 \times 10^{-26}\,\mathrm{cm}^3\,\mathrm{s}^{-1}$.

## 1.5 Summary

Dark matter is a crucial component of the Universe for much of its evolution, and is likely to have formed within the first second. Commonly explored production mechanisms for DM include thermal freeze-out and freeze-in, in which the relic abundance of DM produced is determined by the thermal history of the Universe prior to BBN.

One of the strongest classes of DM candidates, WIMPs, exemplifies this dependence on the thermal background. Thermal freeze-out of WIMPs in a RD Universe, produces the correct abundance of DM for annihilation-rates near the weak scale and a range of DM masses. Although this is a very promising feature of WIMPS, there is increasing pressure on this standard picture, particularly regarding the weak-scale annihilation rate. In light of this pressure, examining WIMP-like DM with smaller annihilation rates in the standard thermal history leads to a freeze-in scenario that can also obtain the correct DM abundance. However, the annihilation rates for freeze-in production in the standard history are extremely small and are beyond the reach of current and upcoming detection capabilities. We will therefore explore alternatives to the standard thermal history of the Universe in order to determine what other areas of the relevant parameter space are opened up by an era of nonstandard expansion in the thermal history. As we will see in the next chapter, nonstandard thermal histories where the expansion rate differs from RD are theoretically well motivated and can accommodate a wide range of DM masses and annihilation rates.

# Chapter 2

# Dark Matter Production in Early Matter Domination

In addition to the observational/experimental motivations to look beyond standard WIMPs, theoretical considerations of the early Universe provide their own motivation for departures from the standard scenario. Well before the onset of BBN, the dominant energy density component need not be radiation, and the thermal history can thus change. Perhaps the most notable example of a deviation from RD concerns the end of inflation itself. During inflationary reheating, the period at the end of inflation that results in a RD Universe, the energy density of the oscillating inflaton can mimic the equation of state of matter, leading to a matter dominated (MD) phase (see [16, 17] for reviews). As the inflaton decays, it transfers its energy density to radiation, and RD ensues. This is an example of how an oscillating scalar field can lead to a period of early matter domination (EMD) in the period before BBN.

In the context of early Universe models and high-energy extensions of the SM, the postinflationary Universe can be accompanied by a host of fields that can lead to nonstandard thermal histories where the expansion of the Universe deviates from RD for a time. Such deviations must complete before the onset of BBN in order to avoid

spoiling its success, but are otherwise unconstrained by current observations. One of the most prominent examples of a nonstandard postinflationary thermal history is an EMD period caused by a long-lived scalar field called a modulus. The presence of such fields in the early Universe is a generic feature of models arising from string theory constructions (see [18] for a review), and they can lead to EMD in the following way. During inflation, moduli are displaced from the minimum of their potential and subsequently oscillate around it, acquiring a matter equation of state (see Appendix A for more details). As a matter component, the energy density of the field redshifts slower than radiation and can thus dominate the energy density of the Universe soon after oscillations begin. Eventually, moduli decay leaving the Universe in a RD state similar to the end of inflationary reheating. Aside from string moduli, periods of EMD can be generically established by oscillating scalar fields or by heavy decoupled particles (see [19, 20, 21, 22] for examples), with constraints on the mass and decay rates such that EMD does not happen too late.

If the thermal history of the Universe includes a phase of EMD, the details of freeze-out/in production change and the values of the parameters that result in the current DM abundance shift (see [23, 24] for examples). The reason for this is that the relation between $H$ and $T$ is different due to the source of radiation from the decay of the dominating matter component.

As the dominant component, which we will call $\phi$, continuously decays at the rate $\Gamma_\phi$, its contribution to the radiation energy density will eventually become more important than simple redshift and will drive the evolution of radiation (see Chapter 4 for details). This period lasts until the decay completes with reheating at $H_{\rm R} \equiv \Gamma_\phi$, and RD subsequently ensues as the energy density gets transferred to the relativistic decay products. [1] The temperature at reheating is given by

[1] Though reheating is not an instantaneous process, the approximation of RD beginning near $H \approx \Gamma_\phi$ is nevertheless a good one. Numerical calculations show that RD typically begins shortly after this time, as we will see in later chapters.

$$T_{\rm R} = \left(\frac{90}{\pi^2 g_{*\rm R}}\right)^{1/4} \left(\Gamma_\phi M_{\rm P}\right)^{1/2} . \tag{2.1}$$

The Boltzmann equation for the evolution of radiation is (neglecting any contribution from the annihilations of DM for the time being, which is subdominant anyway)

$$\frac{d\rho_{\rm r}}{dt} + 4H\rho_{\rm r} = \Gamma_\phi \rho_\phi \, . \tag{2.2}$$

During EMD, $\rho_\phi$ dominates the energy density of the Universe and determines the expansion rate through Eq. (1.1). After multiplying by $a^4$, converting $dt$ to $dH$, and using $a \propto H^{-2/3}$, this gives

$$\frac{d(a^4\rho_{\rm r})}{dH} = -\frac{2a_{\rm i}^4 H_{\rm i}^{8/3} \Gamma_\phi M_{\rm P}^2}{H^{8/3}} \, . \tag{2.3}$$

Integrating this expression and assuming negligible initial radiation yields an expression that describes the period where decays of $\phi$ govern the evolution of radiation:

$$H^{(\text{late EMD})} = \left(\frac{5\pi g_*}{6\sqrt{10} g_{*\rm R}^{1/2}}\right) \frac{T^4}{T_{\rm R}^2 M_{\rm P}} \, . \tag{2.4}$$

This deviates from Eq. (1.4) because of the source of relativistic particles from $\phi$ decay, and characterizes the latter part of any generic EMD period. We will refer to this phase of EMD by a few names which describe its properties, such as the entropy-producing or late phase, as well as simply the standard phase of EMD because Eq. (2.4) is often the feature of interest when discussing such phases (for example see [23]). However, as we will see in later chapters, a generic EMD period can be more complex than this, with various different phases.

## 2.1 Freeze-out during standard early matter domination

If DM freeze-out occurs during this period of EMD (if $T_{\rm f} > T_{\rm R}$), the final abundance will be different than in the RD case. Proceeding with the same freeze-out calculation for the relic DM abundance as in the RD case, but now using the equation above for $H(T)$, results in

$$x_{\rm f} = \ln\left(\frac{3 g_\chi g_{*\rm R}^{1/2}}{\sqrt{5}\pi^{5/2} g_{*\rm f}} \left\langle\sigma_{\rm ann} v\right\rangle_{\rm f} \frac{M_{\rm P} T_{\rm R}^2}{m_\chi} x_{\rm f}^{5/2}\right). \tag{2.5}$$

The value of $x_{\rm f}$ is still typically near 20 [24]. Because the dominant component is decaying, the comoving entropy density is not constant and we must wait until reheating completes for the ratio $n_\chi/s$ to be fixed. We therefore redshift the number density from the time of freeze-out to the time of reheating using $n_\chi \propto H^2$ during EMD for a frozen number density. Now, we can calculate $\Omega_\chi h^2$ as before and get

$$\left(\Omega_\chi h^2\right)^{(\text{late EMD})}_{\text{freeze-out}} \approx \frac{1.3\, g_{*\rm R}^{1/2}}{g_{*\rm f}} \left(\frac{x_{\rm f}}{20}\right)^4 \left(\frac{T_{\rm R}}{1\,\text{GeV}}\right)^3 \left(\frac{100\,\text{GeV}}{m_\chi}\right)^3 \left(\frac{5\times 10^{-29}\,\text{cm}^3\,\text{s}^{-1}}{\left\langle\sigma_{\rm ann} v\right\rangle_{\rm f}}\right). \tag{2.6}$$

A key difference between this expression and the RD equivalent is the dependence on the DM mass and the new parameter $T_{\rm R}$.

## 2.2 Freeze-in during standard early matter domination

If $\langle\sigma_{\rm ann} v\rangle$ is too small to establish equilibrium, we will again have a freeze-in scenario. The details of the calculation are shown in Appendix A.

The main distinction between freeze-in during RD and the late phase of EMD is that the peak-production temperature in EMD occurs at $T \approx m_\chi/4$ rather than the

highest temperature. The prior history is therefore not relevant for production in this phase and once the DM parameters are chosen, the abundance only depends on the reheat temperature $T_{\rm R}$ at the end of EMD.[2] The relic abundance from freeze-in during the late phase of EMD is given by

$$\left(\Omega_\chi h^2\right)^{(\text{late EMD})}_{\text{freeze-in}} \approx \frac{213\, g_\chi^2 g_{*\rm R}^{3/2}}{g_{*\rm f}^3} \left(\frac{T_{\rm reh}}{1\,\text{GeV}}\right)^7 \left(\frac{100\,\text{GeV}}{m_\chi}\right)^5 \left(\frac{\langle\sigma_{\rm ann} v\rangle_{\rm reh}}{10^{-31}\,\text{cm}^3\,\text{s}^{-1}}\right) . \quad (2.7)$$

Figure 2.1 shows the expressions in Eqs. (2.6) and (2.7) for freeze-out and freeze-in production of DM in standard EMD, using typical parameter choices.

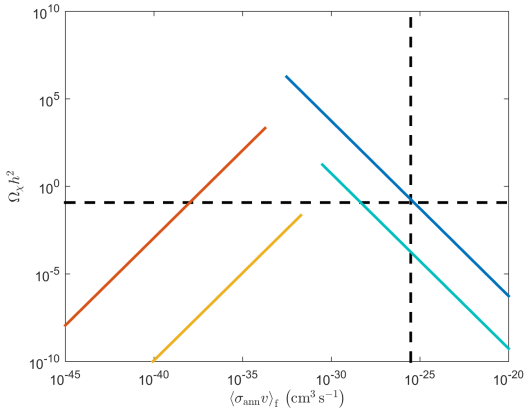


Figure 2.1: Analytical approximations for freeze-out (right) and freeze-in (left) production of DM in standard EMD from Eqs. (2.6) and (2.7) respectively, with DM mass $m_\chi = 100\,\text{GeV}$. The top two lines correspond to a reheat temperature of $T_{\rm R} = 10\,\text{GeV}$, while the bottom two correspond to $T_{\rm R} = 1\,\text{GeV}$. The horizontal and vertical dashed lines are as in Figure 1.1.

## 2.3 Summary

Thermal freeze-out of WIMPs in a standard thermal history of RD between the end of inflation and beginning of BBN naturally leads to the correct relic abundance of DM

[2] In Chapter 4, we will discuss how the prior history and the onset of EMD are actually important for freeze-in production of DM because production at earlier times can dominate over the late EMD contribution in large regions of the relevant parameter space.

for weak-scale annihilations. However, periods of nonstandard evolution are generic predictions of early Universe models and can significantly alter the DM production parameter space. Departures from the standard assumptions of the thermal WIMP scenario are well motivated by both experimental and theoretical considerations, and can lead to interesting new possibilities for DM production in the early Universe.

In this dissertation, we will explore thermal histories involving periods of EMD and the effects they have on DM production. Particularly, as generic thermal histories involving EMD can be more complex than the standard entropy-producing phase presented above, we will study a scenario where two matter components are simultaneously present in Chapter 3, and the details of the onset of an EMD period and its prior history in Chapter 4. We will then move to consider applications of EMD to more exotic scenarios involving DM production from the evaporation of primordial black holes in Chapter 5, and topological DM consisting of hidden-sector magnetic monopoles in Chapter 6. We will briefly touch on possible directions for future work in the concluding chapter, and we include various calculational details for each chapter in the appendix.

# Chapter 3

# Dark Matter Production in Two-Field Early Matter Domination

## 3.1 Introduction

We have seen in the previous chapter that a period of EMD caused by a single decaying matter component can significantly affect the freeze-out/in production of DM. However, string constructions involve many modulus fields that can lead to multiple stages of EMD separated by phases of RD [18]. In the standard picture, each period of EMD is driven by a single field with the last one being the most relevant for DM production due to the previous dilution events. Furthermore, it is possible that two (or more) fields are simultaneously present during the last epoch of EMD. In this chapter, we study such a "two-field" scenario and show that the presence of a second field, even if it constitutes a tiny fraction of the energy density of the Universe and decays very quickly, can significantly enhance the temperature of the Universe during EMD.[1] We calculate the abundance of DM particles produced

[1]The contents of this chapter are published in a modified form as R. Allahverdi and J. K. Osiński, Phys. Rev. D 99, 083517 (2019), and are used with permission [25].

via freeze-out/in under such a modification and find that it opens up the allowed parameter space toward considerably larger DM masses. As a result, PeV-scale DM can be comfortably accommodated by an EMD phase that reheats the Universe to a temperature at or below 10 GeV.

The rest of this chapter is organized as follows. In Section 3.2, we discuss the thermal history in a two-field scenario for EMD and its various regimes. In Section 3.3, we cover DM production via thermal freeze-out/in during this modified history. In Section 3.4, we present the main results of such a scenario. We conclude with a discussion in Section 3.5, and include details of our calculations in Appendix B.

## 3.2 The two-field scenario of early matter domination

We consider a situation where two fields $\phi$ and $\varphi$, with corresponding energy densities $\rho_\phi$ and $\rho_\varphi$, are simultaneously present, and collectively drive a period of EMD. We begin by defining the following parameters:

$$f \equiv \frac{\rho_{\varphi,\mathrm{i}}}{\rho_{\phi,\mathrm{i}}} \qquad , \qquad \alpha \equiv \frac{\Gamma_\varphi}{\Gamma_\phi} \,. \tag{3.1}$$

where, $\Gamma_\phi$ and $\Gamma_\varphi$ are the decay rates of each field respectively, and $\rho_{\phi,\mathrm{i}}$ and $\rho_{\varphi,\mathrm{i}}$ denote the initial energy densities.

We are interested in a situation where both $\phi$ and $\varphi$ are present during an epoch of EMD as opposed to two separate phases of EMD driven by $\phi$ and $\varphi$ respectively. Therefore, without loss of generality, we consider the case where $f < 1$ and $\alpha > 1$, with $\alpha f \gg 1$.[2] As we will see shortly, the case where $\alpha f \approx 1$ aligns the energy

[2]The case with $f > 1$ and $\alpha < 1$ leads to a similar scenario with the roles of $\phi$ and $\varphi$ exchanged. On the other hand, the case with $f > 1$ and $\alpha > 1$ results in successive phases of EMD driven by $\varphi$ and $\phi$ respectively, and the case with $f < 1$ and $\alpha < 1$ leads to a similar scenario with $\varphi$ and $\phi$ again switching roles.

densities and decay rates such that the effect of the second field is no longer felt.

In order to find the instantaneous temperature of the thermal bath, we must solve the following system of Boltzmann equations [10]:

$$\begin{aligned} \frac{d\rho_\phi}{dt} + 3H\rho_\phi &= -\Gamma_\phi \rho_\phi \,, \\ \frac{d\rho_\varphi}{dt} + 3H\rho_\varphi &= -\Gamma_\varphi \rho_\varphi \,, \\ \frac{d\rho_{\rm r}}{dt} + 4H\rho_{\rm r} &= \Gamma_\phi \rho_\phi + \Gamma_\varphi \rho_\varphi \,. \end{aligned} \tag{3.2}$$

The first two equations describe the exponential decay of the energy densities of $\phi$ and $\varphi$, respectively, in an expanding background, while the last one describes the evolution of the radiation energy density due to Hubble expansion as well as feeding from the decay of both $\phi$ and $\varphi$. In the absence of the second field (i.e. $\rho_\varphi = 0$), the situation is reduced to the standard EMD scenario with a single field $\phi$.

The evolution of radiation in the two-field scenario of EMD has three different regimes:

**(1) Two-field regime** ($H \gg \Gamma_\varphi$) – In this regime, both of the $\phi$ and $\varphi$ fields are present. The right-hand side of the last equation in Eq. (3.2) is modified from the single-field case in Eq. (2.4) by an additional factor of $(1 + \alpha f)$. Thus, assuming that both fields decay to relativistic particles in the same sector, the instantaneous temperature of the thermal bath for $H \gg \Gamma_\varphi$ is given by:

$$T \approx \left( \frac{6\sqrt{10} g_{*\rm R}^{1/2}}{5\pi g_*} \right)^{1/4} \left( H T_{\rm R}^2 M_{\rm P} \right)^{1/4} (1 + \alpha f)^{1/4} \,, \tag{3.3}$$

The important point is that even though the field $\phi$ dominates the energy density, the decay of the second field $\varphi$ determines the temperature due to its larger decayed fraction since $\alpha f \gg 1$. As a result, $T$ is enhanced in this regime compared to the single-field scenario of Eq. (2.4) by a factor of $\sim (\alpha f)^{1/4}$.

**(2) Transition regime** ($H_{\rm tran} < H \lesssim \Gamma_\varphi$) – In this regime, the subdominant field $\varphi$ has completely decayed while $\phi$ is still present. Since $\alpha f \gg 1$, the amount of

radiation produced by the decay of $\varphi$ dominates over that continuously produced by decays of $\phi$. The instantaneous temperature of the thermal bath is given by (see Appendix B):

$$T \approx \left(\frac{22.5}{g_{*\mathrm{R}}^{1/3} g_*}\right)^{1/4} \left(\frac{H^2 M_{\mathrm{P}}^2}{T_{\mathrm{R}}}\right)^{1/3} \alpha^{-1/6} f^{1/4} \,. \tag{3.4}$$

We note the different scaling of temperature in the transition regime $T \propto H^{2/3} \propto a^{-1}$, which implies that the temperature is simply redshifted due to the expansion of the Universe. While the field $\varphi$ is absent in this regime, its memory still persists in the form of radiation that its decay produced. As shown in Appendix B, one can estimate $H_{\mathrm{tran}}$ to be:

$$H_{\mathrm{tran}} \simeq 0.5 \left(\frac{\pi^2 g_{*\mathrm{R}}}{90}\right)^{1/2} \frac{T_{\mathrm{R}}^2}{M_{\mathrm{P}}} \alpha^{2/5} f^{-3/5} \,. \tag{3.5}$$

**(3) Single-field regime** ($\Gamma_\phi < H \lesssim H_{\mathrm{tran}}$ ) – The memory of the second field is erased in this regime and the Universe is in the standard EMD phase where the temperature is given by the expression in Eq. (2.4).

The important point to note is that the two-field scenario can yield much higher temperatures than that in the single-field scenario as long as $\alpha f \gg 1$. To demonstrate this, we have numerically solved the Boltzmann equations in Eq. (3.2) to find the evolution of the energy densities in the dominant and subdominant fields, $\phi$ and $\varphi$ respectively, as well as radiation. The initial conditions correspond to the onset of the late phase of EMD, and hence the initial radiation energy density is negligible. We will treat the importance of substantial initial radiation in Chapter 4.

In Figure 3.1, we show the evolution of the three energy densities, as a function of the scale factor $a$, in a two-field scenario with $f = 10^{-4}$, $\alpha = 10^8$, and $T_{\mathrm{R}} = 10$ GeV. We depict the temperature of the Universe in this scenario in Figure 3.2 and compare it to a single-field scenario (i.e. $f = 0$) with the same $T_{\mathrm{R}}$. We see that in the two-field regime (region 1), the temperature is enhanced by a factor of $(\alpha f)^{1/4}$ as expected. The temperature starts approaching the single-field case during

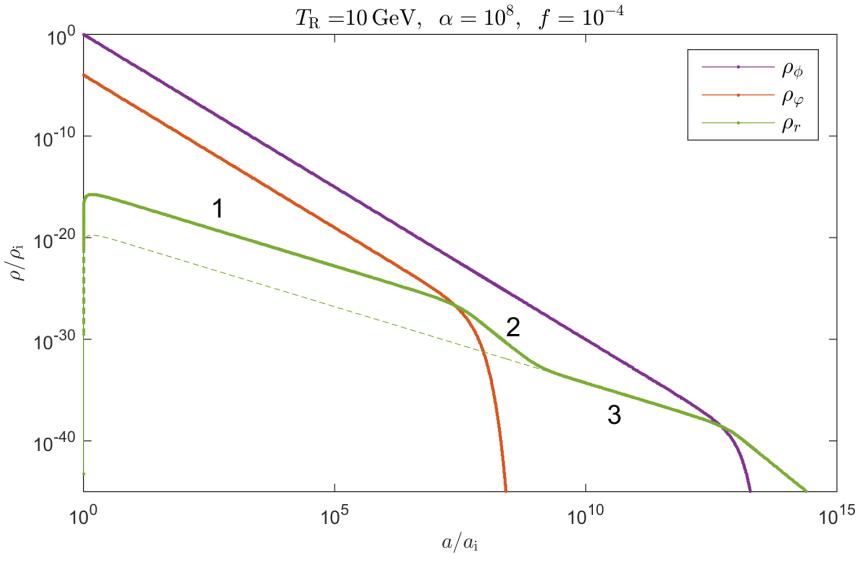


Figure 3.1: Evolution of the energy density of the dominant field $\phi$ (purple/top), the subdominant field $\varphi$ (red/middle), and radiation (green/bottom) in a two-field scenario with $f = 10^{-4}$, $\alpha = 10^8$, and $T_{\rm R} = 10$ GeV. Regions 1, 2, and 3 correspond to the two-field, transition, and single-field regimes respectively. The dashed line that extrapolates region 3 denotes the single-field scenario with the same $T_{\rm R}$.

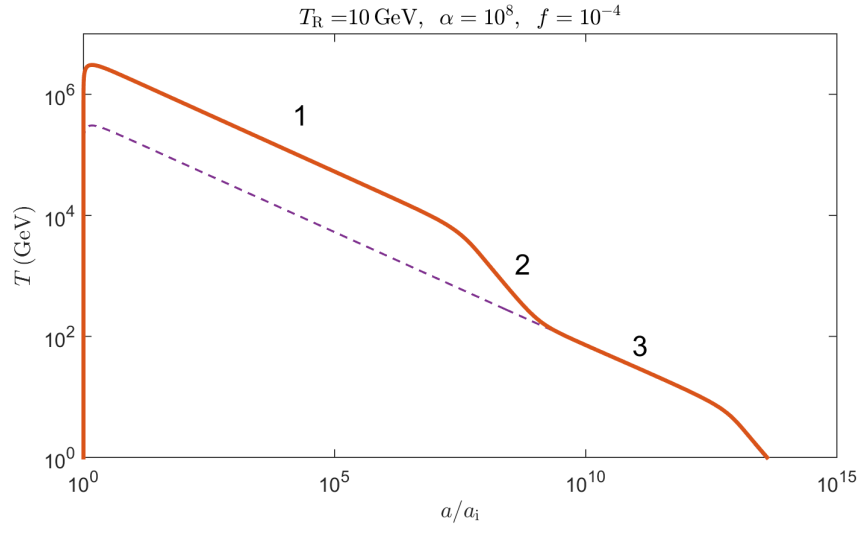


Figure 3.2: Evolution of the temperature in the two-field scenario of Figure 3.1. The temperature is enhanced by a factor of $(\alpha f)^{1/4} \approx 10$ in region 1, approaches that of the single-field scenario in region 2, and coincides with it in region 3.

the transition regime (region 2) as the memory of the second field is being erased. Eventually, this transition completes as the Universe enters the single-field regime (region 3).

We would like to reiterate that the temperature enhancement depends on the product of $\alpha$ and $f$ instead of their individual values. Therefore, as long as $\alpha f \gg 1$, a subdominant field ($f \ll 1$) that decays very early ($\alpha \gg 1$) can indeed significantly enhance the instantaneous temperature at early stages of EMD.

## 3.3 Dark matter production in the two-field scenario

In this section, we discuss production of DM via thermal freeze-out/in in the two-field scenario of EMD. We particularly show how the temperature enhancement in the two-field and transition regimes, discussed in the previous section, affects the DM relic abundance.

In order to calculate the DM relic abundance in the two-field scenario, one needs to solve the equations in Eq. (3.2) together with the following one:

$$\frac{dn_\chi}{dt} + 3Hn_\chi = \langle\sigma_{\rm ann}v\rangle_{\rm f}\left(n_{\chi,\rm eq}^2 - n_\chi^2\right) , \tag{3.6}$$

where $n_{\chi,\rm eq}$ denotes the thermal equilibrium value of the DM number density at a given temperature. We consider the case where $\langle\sigma_{\rm ann}v\rangle_{\rm f}$ has no temperature dependence (as happens in the case of S-wave dominance). When the annihilation rate is constant, there is no need to have the subscript 'f'. We nevertheless keep it for the sake of generality. The situation is qualitatively similar for temperature-dependent $\langle\sigma_{\rm ann}v\rangle_{\rm f}$, but quantitative differences will arise.

In the case of freeze-out, $n_\chi$ closely follows $n_{\chi,\rm eq}$ down to the freeze-out temperature $T_{\rm f}$. In the case of freeze-in, we always have $n_\chi \ll n_{\chi,\rm eq}$ as DM never reaches

thermal equilibrium. The system of four differential equations can be solved numerically in both cases, which we present in the next section. Here, we provide approximate analytical expressions for the DM abundance in the two-field and transition regimes, where the two-field scenario deviates from the single-field scenario:

**Two-field regime** – Let us first consider freeze-out during the two-field regime. In general, the number density of DM particles at the time of freeze-out follows $n_{\rm f} \propto H_{\rm f}$. The expansion of the Universe between freeze-out and reheating, which is the relevant epoch for calculating the entropy density, dilutes $n_{\rm f}$ by a factor of $H_{\rm R}^2/H_{\rm f}^2$. This implies that $\Omega_\chi h^2 \propto H_{\rm f}^{-1}$, which can be seen from Eqs. (2.4) and (2.6) in the single-field case. Therefore, after taking into account the additional factor of $(\alpha f)^{1/4}$ in the relation between $T$ and $H$ in the two-field regime (Eq. (3.3)), we arrive at:

$$\left(\Omega_\chi h^2\right)^{\text{(2-field)}}_{\text{freeze-out}} \approx \alpha f \left(\Omega_\chi h^2\right)^{\text{(1-field)}}_{\text{freeze-out}} , \tag{3.7}$$

where $(\Omega_\chi h^2)^{\text{(1-field)}}_{\text{freeze-out}}$ is given in Eq. (2.6). Due to the same functional dependence of $H$ on $T$, the value of $m_\chi/T_{\rm f}$ is almost the same as that in the single-field case up to a logarithmic term in $\alpha f$.

Next, we consider freeze-in during the two-field regime. Since $H \propto T^4$, as in the standard scenario, the bulk of DM particles are produced within one Hubble time of $T_{\rm f} \sim m_\chi/4$. The number density of DM particles at the time of freeze-in is $n_{\rm f} \propto H_{\rm f}^{-1}$ and the dilution factor due to expansion between freeze-in and reheating is $H_{\rm R}^2/H_{\rm f}^2$. This implies that $\Omega_\chi h^2 \propto H_{\rm f}^{-3}$ in this case, which after using Eq. (3.3) results in:

$$\left(\Omega_\chi h^2\right)^{\text{(2-field)}}_{\text{freeze-in}} \approx (\alpha f)^3 \left(\Omega_\chi h^2\right)^{\text{(1-field)}}_{\text{freeze-in}} , \tag{3.8}$$

where $(\Omega_\chi h^2)^{\text{(1-field)}}_{\text{freeze-in}}$ is given in Eq. (2.7).

We note that the DM relic abundance is enhanced in the two-field regime for both the freeze-out and freeze-in cases above, with the latter being more significant. It is then seen from Eqs. (2.6) and (2.7) that, for fixed $T_{\rm R}$ and $\langle\sigma_{\rm ann} v\rangle_{\rm f}$, the parameter space that produces the correct DM abundance is shifted toward larger values of $m_\chi$.

**Transition regime** – In the case of freeze-out, the relic abundance of DM particles at reheating follows the usual scaling $\Omega_\chi h^2 \propto H_{\rm f}^{-1}$. However, in the transition regime the relation between $H$ and $T$ is given by the expression in Eq. (3.4). Comparing to (2.4), we find:

$$\left(\Omega_\chi h^2\right)^{\rm (tran)}_{\text{freeze-out}} \approx 0.15 \left(\frac{g_{*\rm f}}{g_{*\rm R}}\right)^{5/8} \left(\frac{T_{\rm f}}{T_{\rm R}}\right)^{5/2} \alpha^{-1/4} f^{3/8} \left(\Omega_\chi h^2\right)^{\rm (1\text{-}field)}_{\text{freeze-out}} . \tag{3.9}$$

Due to the different relation between $H$ and $T$, the value of $m_\chi/T_{\rm f}$ differs from that in the two-field regime and the single-field case by logarithmic corrections.

However, the situation is very different in the case of freeze-in. The comoving number density of DM particles produced via freeze-in is proportional to $\int n^2_{\chi,\rm eq} a^3 dt$. Starting at a temperature $T \gg m_\chi$, we have $n_{\chi,\rm eq} \propto T^3$. In both the two-field regime and the single-field scenario, the $H \propto T^4$ relation causes the integral to be dominated by the lowest relevant $H$, which corresponds to $T \sim m_\chi/4$ [23, 24]. On the other hand, in the transition regime, see Eq. (3.4), we have $H \propto T^{3/2}$. As a result, as shown in Appendix B, the integral is now controlled by the largest value of $H$ in the transition regime, namely $H \simeq \Gamma_\varphi$. Up to an overall proportionality factor, see Appendix B, the freeze-in DM abundance is then found to be:

$$\left(\Omega_\chi h^2\right)^{\rm (tran)}_{\text{freeze-in}} \propto f^{3/2} (T_{\rm R} M_{\rm P}) \left(\frac{m_\chi}{1\,\text{GeV}}\right) \langle \sigma_{\rm ann} v \rangle_{\rm f} . \tag{3.10}$$

An interesting point to note is that the DM abundance in this case has a milder dependence on $m_\chi$ and $T_{\rm R}$ as compared to the two-field regime and the single-field scenario. This is because freeze-in production mainly occurs at the onset of the transition regime regardless of the value of $m_\chi$.

## 3.4 Results

In this section, we present our results. We have numerically solved the coupled system of four Boltzmann equations in Eqs. (3.2) and (3.6) to obtain the DM relic

abundance. The initial conditions are set such that we begin well within the EMD phase, but also long before either of the $\phi$ or $\varphi$ fields decay, so that the initial radiation energy density is negligible. This allows us to obtain the behavior due to the decay of the two fields, as opposed to the residual effects at the start of EMD. Decayed energy densities are tracked until they are sufficiently small to be unimportant for the subsequent evolution and are then dropped to facilitate faster numerical calculation. We have taken the detailed temperature dependence of the $g_*$ factor into account down to below $T_{\rm R}$, as shown in Appendix A. In order to calculate the DM relic abundance, we have normalized the DM number density with the entropy density long after decay of the dominant field $\phi$ completes.

We investigate the parameter space, in the $m_\chi - \langle\sigma_{\rm ann}v\rangle_{\rm f}$ plane that yields the correct DM abundance via freeze-out/in for various values of $f$ and $\alpha$, as well as $T_{\rm R}$. Each $T_{\rm R}$ has a corresponding single-field scenario ($f = 0$) that we use as a baseline for comparison. In Figures 3.3 and 3.4, we show curves in the $m_\chi - \langle\sigma_{\rm ann}v\rangle_{\rm f}$ plane that represent individual choices of the three varied parameters that reproduce the correct abundance. We vary $f$ for constant $\alpha$ in Figure 3.3, and $\alpha$ for constant $f$ in Figure 3.4. The left and right panels in each figure correspond to $T_{\rm R} = 10$ GeV and $T_{\rm R} = 1$ GeV respectively. For a given set of parameters, DM is underproduced (overproduced) above/outside (under/inside) each curve. The peak of each curve marks the transition between freeze-in (on the left) and freeze-out (on the right).

The curves, in general, consist of three distinct regions that correspond to DM production in regions 1, 2, or 3 of Section 3.2. The central region that encompasses the peak of each curve, mimics the shape of the single-field curve while being offset toward higher DM masses and slightly smaller annihilation rates. This distinguishes the part of the parameter space where DM production happens well within the two-field regime (region 1). The curves then move into a near-vertical transition region on both the freeze-in and freeze-out sides, which is identified with DM production in the transition regime (region 2). The two ends of each curve finally merge with the

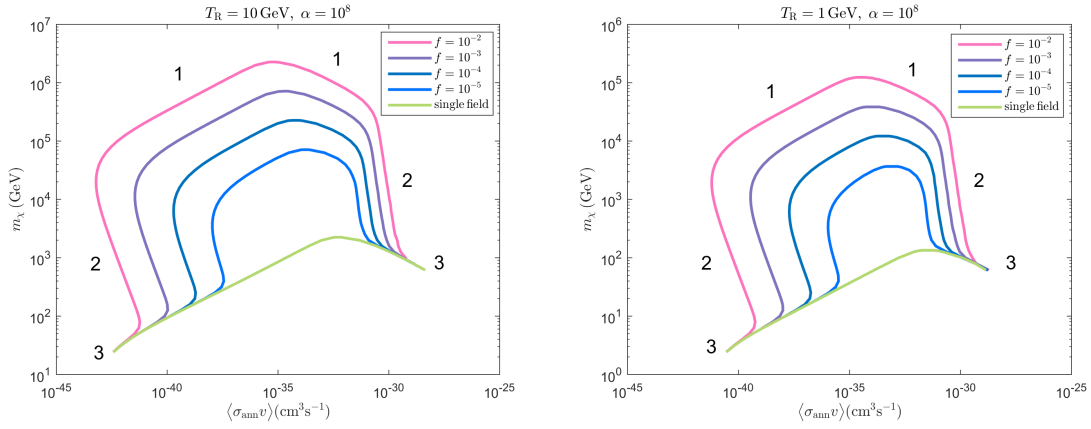


Figure 3.3: Curves represent points in the $m_\chi - \langle\sigma_{\mathrm{ann}}v\rangle_{\mathrm{f}}$ plane where the two-field scenario yields the correct DM abundance. We have chosen $\alpha = 10^8$ and varied $f$ between $10^{-2}$ (pink/top) and $f = 10^{-5}$ (blue/bottom) in this figure. The single-field scenario is shown at the very bottom for comparison. The left (right) panel corresponds to $T_{\mathrm{R}} = 10$ GeV ($T_{\mathrm{R}} = 1$ GeV). The DM abundance is set during the two-field regime, transition regime, and single-field regime in regions 1, 2, and 3 respectively. The left and right sides of the curves correspond to freeze-in and freeze-out production respectively.

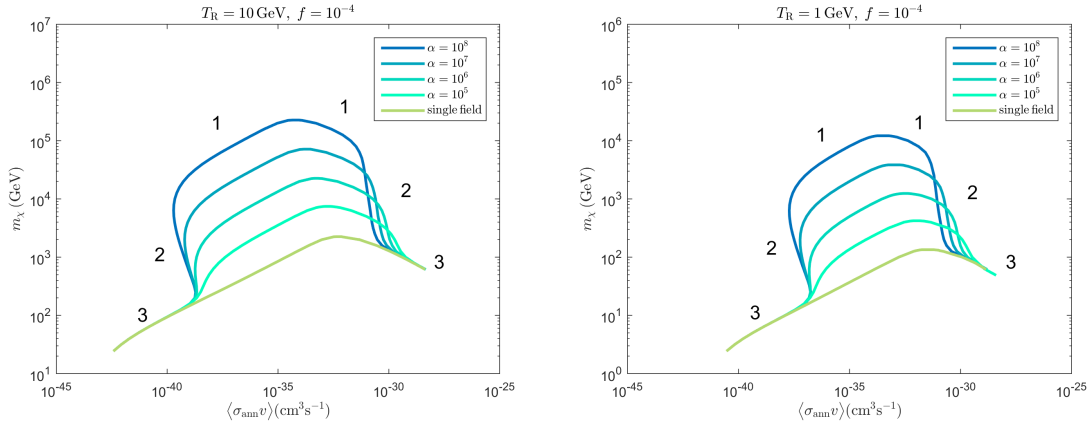


Figure 3.4: The same as Figure 3.3, but we have chosen $f = 10^{-4}$ and varied $\alpha$ between $10^8$ (blue/top) and $10^5$ (cyan/bottom) in this figure.

single-field curve, where DM production occurs in the single-field regime after the memory of the second field has been erased (region 3). The following main features are observed in the figures:

**(i)** The peak, corresponding to region 1, is more significant for larger values of $f$ and $\alpha$. For fixed values of $f$ and $\alpha$, the shape of the peak does not depend on $T_{\rm R}$, but for higher $T_{\rm R}$ it occurs at a larger $m_\chi$.

**(ii)** As $f$ increases for constant $\alpha$, see Figure 3.3, region 1 broadens, pushing out region 2 toward smaller (larger) values of $\langle\sigma_{\rm ann}v\rangle_{\rm f}$ on the freeze-in (freeze-out) side. The change is larger on the freeze-in side.

**(iii)** As $\alpha$ increases for constant $f$, see Figure 3.4, the points where regions 2 and 3 meet are independent of $\alpha$ on the freeze-in side, and only have a mild $\alpha$-dependence on the freeze-out side, moving toward smaller $\langle\sigma_{\rm ann}v\rangle_{\rm f}$. The width of region 1 changes slightly.

These features can be qualitatively explained by using the relations that we derived in Section 3.3. Let us start with point (i) from above. As mentioned earlier, the position of the peak can be estimated by setting the freeze-out and freeze-in DM abundances equal. Using Eqs. (3.7) and (3.8) for the two-field regime (region 1), we find that $m_\chi \propto (\alpha f)^{1/2}$ and $\langle\sigma_{\rm ann}v\rangle_{\rm f} \propto (\alpha f)^{-1/2}$ at the peak. This explains why the peak moves toward larger values of $m_\chi$ and smaller values of $\langle\sigma_{\rm ann}v\rangle_{\rm f}$ with increasing $f$ or $\alpha$. It also implies that the peak position depends on the product $\alpha f$. This is confirmed by comparing the curve with $f = 10^{-5}$ in Figure 3.3 to that with $\alpha = 10^7$ in Figure 3.4 (both having $\alpha f = 10^3$). As far as the dependence on $T_{\rm R}$ is concerned, we note that DM production occurs in the two-field regime when $T_{\rm f}$ is larger than the temperature at $H \simeq \Gamma_\varphi \propto T_{\rm R}^{1/2}$. Since $T_{\rm f} \sim m_\chi/4$ for freeze-in and $T_{\rm f} \propto m_\chi$ (up to logarithmic corrections) for freeze-out, higher $T_{\rm R}$ implies larger values of $m_\chi$ in region 1, hence a higher peak.

Regarding points (ii) and (iii), we need to find the points at which regions 2 and

3 meet. On the freeze-in side, this point can be found by setting the expressions in Eqs. (2.7) and (3.10) equal. This results in $m_\chi \propto f^{-1/4}$ and $\langle \sigma_{\rm ann} v \rangle_{\rm f} \propto f^{-5/4}$ at the intersection point, which is independent of $\alpha$. This explains why this point moves down and to the left with increasing $f$ in Figure 3.3 but does not move in Figure 3.4 (where $f$ is kept constant). On the freeze-out side, the intersection point can be found by setting $T_{\rm f} \propto m_\chi$ (up to logarithmic factors) equal to the temperature at $H_{\rm tran}$. After using Eq. (3.4) and (3.5), this results in $m_\chi \propto \alpha^{1/10} f^{-3/20}$ and $\langle \sigma_{\rm ann} v \rangle_{\rm f} \propto \alpha^{-3/10} f^{9/20}$ at the intersection point. This explains why the point moves slowly in Figure 3.3 and very little in Figure 3.4. The opposite signs in the exponents of $\alpha$ and $f$ explain why the curves on the freeze-out side of Figure 3.4 cross while those of Figure 3.3 do not. The points where regions 1 and 2 meet can be found similarly to 2 and 3. We have checked that for these points too, our estimates agree with what is obtained from the figures. Finally, (i) and (ii) imply that decreasing $f$ lowers the peak and makes region 1 narrower. This is expected as the curves must be reduced to that of the single-field scenario in the $f \to 0$ limit.

The main conclusion from our results is that the two-field scenario can yield the correct abundance for much larger DM masses. As seen in Figures 3.3 and 3.4, the maximum DM mass that it can accommodate is larger than that in the single-field scenario by an approximate factor of $(\alpha f)^{1/2}$. This holds even for a very small value of $f$ as long as $\alpha$ is sufficiently large so that $\alpha f \gg 1$.[3] It is indeed interesting that a subdominant field with a tiny fractional energy density that decays very early can affect DM production in a significant way. As seen in Figures 3.3 and 3.4, the two-field scenario with $T_{\rm R} \gtrsim \mathcal{O}(\text{GeV})$ can yield the correct abundance for DM masses up to $\mathcal{O}(\text{PeV})$.

[3]We note that $\alpha$ is bounded from above in order for the second field to not decay before the onset of EMD. This in turn sets a lower limit on the value of $f$ for which the subdominant field can have a significant effect. However, in realistic situations, this lower limit is typically too small to be relevant.

## 3.5 Discussion and conclusion

We have shown how a second field can enhance the temperature of the Universe and thereby affect DM production during EMD. We now briefly discuss some possible realizations of the two-field scenario and reasonable ranges of the $f$ and $\alpha$ parameters that can be expected.

A natural possibility that can arise in string constructions is that $\phi$ and $\varphi$ are both modulus fields. Such models typically contain many moduli with gravitationally suppressed couplings to matter, implying that $\Gamma_\phi \sim m_\phi^3/M_{\rm P}^2$ and $\Gamma_\varphi \sim m_\varphi^3/M_{\rm P}^2$. Assuming that $\phi$ is the lightest modulus, it drives the last phase of EMD relevant for DM production. Obtaining $T_{\rm R} \sim (1-10)$ GeV then requires that $m_\phi \sim (10^6 - 10^7)$ GeV. Explicit string constructions exist in the context of KKLT [26] and large volume [27] flux compactifications where the volume modulus arises as the lightest modulus in the desired mass range [28, 29, 30]. The second field $\varphi$ can then be one of the heavier moduli that decays before $\phi$. The amplitude of moduli at the onset of their oscillations is $\gtrsim \mathcal{O}(0.1\, M_{\rm P})$ (see Appendix A). This implies that $H \sim m_\phi$ at the onset of EMD, which requires $m_\varphi < 10^{14}$ GeV in order for $\varphi$ to decay during EMD. For $m_\varphi \lesssim 10^3 m_\phi$, the $\alpha$ parameter is in the range shown in Figures 3.3 and 3.4. Due to the Planckian size of the initial amplitude of both fields, we can have $f \sim \mathcal{O}(1)$, in which case the effect of the second field will be even more prominent than that shown in the figures.

Another possibility is that the second field $\varphi$ belongs to the visible sector, a notable example of which is supersymmetric flat directions. These are directions in the field space of supersymmetric extensions of the SM along which the supersymmetry conserving part of the potential identically vanishes at the renormalizable level [31, 32, 33]. These fields are typically displaced from the true minimum of their potential in the early Universe. The initial amplitude of their oscillations depends on the level of nonrenormalizable operator that lifts flatness [34], and can be much

smaller than $M_{\rm P}$. One can then naturally obtain the small values of $f$ in Figures 3.3 and 3.4 if $\phi$ is a modulus and $\varphi$ is a supersymmetric flat direction. Since $\varphi$ has gauge and Yukawa couplings to other fields in this case, it induces a large mass for them that is proportional to the amplitude of its oscillations. As a result, $\varphi$ decay is kinematically blocked until the induced mass has dropped below $m_\varphi$. For $m_\phi \sim (10^6 - 10^7)$ GeV (as in the previous case) and $m_\varphi \gtrsim \mathcal{O}(\text{TeV})$ (so that the scale of supersymmetry breaking in the visible sector is not much higher than TeV), the second field decays during EMD and can lead to values of $\alpha$ that are comparable to or higher than those in Figures 3.3 and 3.4.

In passing, we note a more exotic possibility where the subdominant component is not a field but is composed of primordial black holes (PBH). PBH's with a mass $\mathcal{O}(10^8\,\text{g})$ evaporate before BBN and could form during a very early bout of matter domination [35]. A situation could then arise where a population of light PBH's in an extended mass range constitute the subdominant component of energy density during EMD. For more on PBH's, see Chapter 5.

In summary, we have studied a modification of EMD that contains two (or, perhaps more) fields. The presence of a second field may be expected in realistic models and can have important consequences. Even a subdominant field with a tiny fractional energy density that decays much earlier than the dominant field can considerably enhance the temperature of the Universe and affect freeze-out/in production of DM during EMD. We have shown that this two-field scenario can open up new regions of the parameter space with much larger DM masses. Therefore, the details of the EMD epoch should be taken into account for a careful determination of the DM relic abundance.

# Chapter 4

# Dark Matter Production Prior to Early Matter Domination

## 4.1 Introduction

So far, we have discussed EMD in terms of the entropy-generating phase of the standard single-field scenario as well as a modification to it in the presence of a second field. In this chapter, we will consider the entirety of a generic EMD period including its onset after a period of prior RD.[1] The picture that will emerge is that EMD in general has two behaviors depending on the abundance of radiation: the standard behavior of Eq. (2.4) where the evolution of radiation is determined by decay of the matter component, and an additional behavior where radiation simply redshifts as the memory of its initial abundance gets erased.

In general, an EMD epoch is only one of the stages in the post-inflationary history of the Universe. Unless it is driven by oscillations of the inflaton itself, EMD is typically preceded by a RD phase or a period with a more general equation

[1]The contents of this chapter have been submitted for publication to Phys. Rev. D in a modified form, and are used with permission [36].

of state. Thermal freeze-out or freeze-in at these early stages can also contribute to the DM relic abundance (for example, see [37, 38, 39]) and thereby affect the allowed parameter space. Since freeze-out occurs at temperatures below the DM mass $m_\chi$, pre-EMD production will only be relevant for (very) large DM masses in this case. On the other hand, in the case of freeze-in, the main contribution to the DM abundance can arise when DM particles are (ultra) relativistic. Thus, pre-EMD production can have a significant affect on the freeze-in side of the parameter space for values of $m_\chi$ at the weak scale or below. In such cases, an exact calculation of the DM relic abundance requires knowledge of the earlier stages of the nonstandard thermal history.

In this chapter, we perform a detailed study of freeze-in within a nonstandard thermal history that involves a RD phase after inflationary reheating followed by a period of EMD. Such an EMD phase is characterized by two distinct periods: a transition during which the initial radiation energy density redshifts away, which we call the memory phase, and the usual EMD behavior once entropy production becomes significant. We calculate the contributions to the DM relic abundance from production during the prior RD phase as well as the memory phase for the case that $\langle\sigma_{\rm ann}v\rangle_{\rm f}$ is constant over the temperature range of interest. This early contribution to DM production depends on the temperature of the Universe at the onset of the EMD epoch $T_0$ and at the completion of inflationary reheating $T_{\rm reh}$, in addition to that at the end of the EMD epoch $T_{\rm R}$. We show that pre-EMD production can totally dominate the DM relic abundance in large parts of the $m_\chi - \langle\sigma_{\rm ann}v\rangle_{\rm f}$ plane, and the allowed parameter space is highly sensitive to $T_0$ and $T_{\rm R}$. A particularly notable observation is that the relic abundance is virtually independent of $\langle\sigma_{\rm ann}v\rangle_{\rm f}$ for a very broad range of $\langle\sigma_{\rm ann}v\rangle_{\rm f}$, spanning over many decades, where DM particles start in chemical equilibrium in the pre-EMD epoch and decouple later on. In this case, measurement of $m_\chi$ at collider experiments, in combination with other cosmological implications of an EMD epoch, may be used as a potential probe of the elusive freeze-in scenario.

The rest of this chapter is organized as follows. In Section 4.2, we discuss a simple nonstandard thermal history and calculate the pre-EMD contributions to DM production via freeze-in. In Section 4.3, we present our main results including the allowed regions in the $m_\chi - \langle\sigma_{\rm ann}v\rangle_{\rm f}$ plane and their sensitivity to the history prior to EMD. We elaborate on the correlation between $m_\chi$ and $T_0/T_{\rm R}$ in large parts of the parameter space in Section 4.4, and discuss connections to observables as well as implications for a modulus-driven EMD. We conclude with some discussions in Section 4.5, and include details of our calculations in Appendix C.

## 4.2 Dark matter abundance in the freeze-in scenario

As mentioned, a period of EMD naturally arises in a well-motivated class of early Universe models. However, it is typically only one of the stages in the postinflationary history. We consider a simple scenario that starts with a RD phase at the end of inflationary reheating (for reviews, see [16, 40]), followed by an EMD epoch driven by oscillations of a long-lived scalar field, or nonrelativistic quanta produced in the postinflationary Universe [19, 20, 21, 22]. A standard RD Universe is established at the end of EMD and before BBN.

Here, we are mainly interested in the evolution of the temperature and the freeze-in production of DM without delving into the details of inflationary reheating, the specific particle physics origin of EMD, or the explicit models for DM freeze-in (as done, for example, in [41]). This can be done by introducing three parameters: the largest temperature in the RD phase after inflationary reheating $T_{\rm reh}$, the temperature at the onset of EMD $T_0$, and the highest temperature in the subsequent RD phase $T_{\rm R}$. The corresponding Hubble expansion rates are denoted by $H_{\rm reh}$, $H_0$, and $H_{\rm R}$ respectively.

In calculating the DM relic abundance, we consider the case where $\langle\sigma_{\rm ann}v\rangle_{\rm f}$ is constant over the temperature range of interest (namely, $T_{\rm R} \lesssim T \lesssim T_{\rm reh}$). This can be the case, for example, if DM interaction with SM particles is mediated by particles whose mass is above $T_{\rm R}$. Also, without loss of generality, we assume that the DM particle, $\chi$, represents one degree of freedom. In Section 4.5, we will briefly comment on cases with $T$ dependence of $\langle\sigma_{\rm ann}v\rangle_{\rm f}$, and on more general thermal histories involving multiple epochs of EMD separated by RD phases. The details of our calculations can be found in Appendix C.

### 4.2.1 The standard lore

We will briefly recap the case of freeze-in during the late phase of EMD, where decay of the matter component determines the temperature evolution (see Chapter 2). Deep inside the EMD era, $H_{\rm R} \ll H \ll H_0$, there is a subdominant radiation component due to decay of the species that drive EMD. Assuming that the decay products thermalize promptly[2], a thermal bath forms with the instantaneous temperature (see Eq. (2.4)):

$$T \approx \left(\frac{6\sqrt{10}g_{*\rm R}^{1/2}}{5\pi g_*}\right)^{1/4} \left(HT_{\rm R}^2 M_{\rm P}\right)^{1/4} . \tag{4.1}$$

In the freeze-in scenario, $\langle\sigma_{\rm ann}v\rangle_{\rm f}$ is so small that DM particles do not reach thermal equilibrium during EMD, and are produced from annihilations of the SM particles. The main contribution to the DM abundance occurs when $T \sim m_\chi/4$, the reason being that particles produced at higher temperatures are quickly diluted by the Hubble expansion, while production at lower temperatures is Boltzmann suppressed. The relic abundance from freeze-in during this period of EMD is given by (see Eq. (2.7)):

[2]The time scale of thermalization has been estimated, for example, in [42].

$$\left(\Omega_\chi h^2\right)^{(\text{late EMD})}_{\text{freeze-in}} \approx \frac{213\, g_\chi^2 g_{*\text{R}}^{3/2}}{g_{*\text{f}}^3} \left(\frac{T_{\text{reh}}}{1\,\text{GeV}}\right)^7 \left(\frac{100\,\text{GeV}}{m_\chi}\right)^5 \left(\frac{\langle\sigma_{\text{ann}} v\rangle_{\text{reh}}}{10^{-31}\,\text{cm}^3\,\text{s}^{-1}}\right) . \quad (4.2)$$

For a given DM mass, the maximum value of $\langle\sigma_{\text{ann}} v\rangle_{\text{f}}$ in the freeze-in regime can be approximately found by setting the DM number density $n_\chi$ equal to its thermal equilibrium value $n_{\chi,\text{eq}}$ at $T \sim m_\chi/4$. For larger values of $\langle\sigma_{\text{ann}} v\rangle_{\text{f}}$, DM particles reach equilibrium with the thermal bath and production therefore transitions to the freeze-out regime. For $T_{\text{R}} \sim$ (1-10) GeV, the maximum value of $\langle\sigma_{\text{ann}} v\rangle_{\text{f}}$ in the freeze-in regime lies within the range $10^{-33} - 10^{-32}\,\text{cm}^3\,\text{s}^{-1}$ (see Figure 2.1).

### 4.2.2 Production prior to early matter domination

In general, an EMD period can be more complicated than the standard case reviewed above. Particularly, if the abundance of radiation during EMD is ever significantly larger than the contribution from decay, then the relation between $T$ and $H$ will deviate, for a time, from that in Eq. (4.1). The temperature evolution throughout the full EMD era may thus have multiple phases, as we saw in the two-field scenario of Chapter 3. A large abundance of radiation can arise from the presence of additional decaying components (as in Chapter 3), or, more simply, from a RD phase that precedes EMD. In the postinflationary history we are considering, a period of RD is present before EMD resulting in a large abundance of radiation at the onset of EMD[3]. This radiation then redshifts away until the decay contribution becomes dominant, recovering Eq. (4.1). The temperature evolution during the full EMD period therefore has two phases: an initial phase during which the memory of the prior radiation is being erased, followed by the usual decay-driven phase.

We now consider the evolution of the temperature in the two periods prior to the entropy-producing phase of EMD.

[3]The effect of substantial initial radiation at early stages of EMD is explored in [43] in the context of direct production of DM from decays of the dominant component.

**RD phase prior to EMD:** The Universe is in a RD period for $H_0 \lesssim H \lesssim H_{\rm reh}$, during which radiation simply redshifts and temperature is inversely proportional to the scale factor: $T \propto a^{-1}$. This results in the standard relation between $T$ and $H$ (see Eq. (1.4)):

$$T = \left(\frac{90}{\pi^2 g_*}\right)^{1/4} (H M_{\rm P})^{1/2} \ . \tag{4.3}$$

**Memory phase of EMD:** The radiation and matter components have comparable energy densities at $H \approx H_0$, which signals the beginning of the EMD era[4]. Although $H \propto a^{-3/2}$ for $H_{\rm R} \lesssim H \lesssim H_0$, the existing radiation dominates over the contribution from the decaying matter component(s) driving EMD for some time, and continues to redshift. As a result, $T \propto a^{-1}$ for $H_{\rm tran} \lesssim H \lesssim H_0$, where:

$$H_{\rm tran} \simeq \left(\frac{\pi^2 g_{*\rm R}^{3/5} g_{*0}^{2/5}}{90}\right)^{1/2} \frac{T_{\rm R}^{6/5} T_0^{4/5}}{M_{\rm P}}, \tag{4.4}$$

and the relation between $T$ and $H$ is[5]:

$$T \approx \left(\frac{90}{\pi^2 g_*^{3/4} g_{*0}^{1/4}}\right)^{1/3} \left(\frac{H^2 M_{\rm P}^2}{T_0}\right)^{1/3}. \tag{4.5}$$

Once $H \ll H_{\rm tran}$, the memory of the initial radiation is completely erased and the $T$ dependence on $H$ transitions to that of Eq. (4.1) until the end of EMD.

We show the evolution of $T$ in terms of $H$ in Figure 4.1, derived from numerical calculations, through the entire nonstandard thermal history considered here for $T_{\rm reh} = 10^{12}$ GeV, $T_0 = 10^{10}$ GeV, and $T_{\rm R} = 10$ GeV. The evolution during the different stages is in very good agreement with the relations given in Eqs. (4.1), (4.3), and (4.5).

[4]This is, of course, a continuous transition, but the time of comparable energy densities is nevertheless a good approximation to the beginning of EMD.

[5]Eq. (4.5) is easily obtained by evaluating Eq. (4.3) at $T = T_0$ and using the appropriate redshift relation for memory EMD, while Eq. (4.4) makes use of the redshift relations all the way to $T = T_{\rm R}$. One can also approximately obtain Eqs. (4.4) and (4.5) from Eq. (3.5) of Chapter 3 with $f = 1$ and $\alpha = (g_{*0} T_0^4 / g_{*\rm R} T_{\rm R}^4)^{1/2}$ to match the case under consideration here.

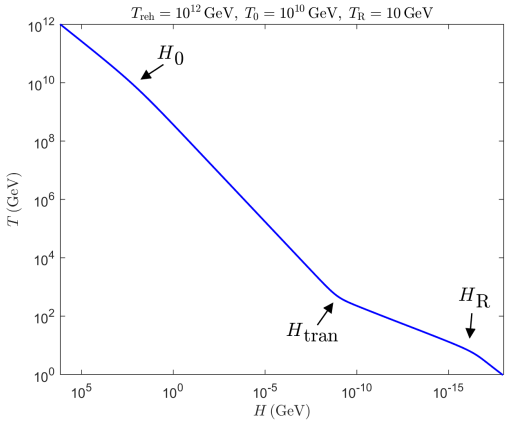


Figure 4.1: Temperature of the Universe as a function of the Hubble expansion rate showing the postinflationary history we are considering. The curve begins at the top left corner, when $H \approx H_{\rm reh}$, with an early period of RD. The EMD period lasts from $H \approx H_0$ to $H \approx H_{\rm R}$, with $H_{\rm tran} \lesssim H \lesssim H_0$ corresponding to the memory phase, and $H_{\rm R} \lesssim H \lesssim H_{\rm tran}$ to the entropy-producing phase. The Universe returns to a RD phase after the end of EMD, where $H < H_{\rm R}$.

As shown in Appendix C, the relation between $T$ and $H$ in these two phases implies that the main contribution to DM production occurs at the highest temperature in each phase. Hence, with $T_{\rm reh} \gg T_0$, the DM relic abundance is set in the pre-EMD epoch. This pre-EMD component of the relic abundance has two distinct regimes based on the value of $\langle\sigma_{\rm ann}v\rangle_{\rm f}$. If it is very small, DM particles will not be able to establish chemical equilibrium throughout the postinflationary history. Production in this "decoupling" regime will dominantly occur at $T \simeq T_{\rm reh}$. If $\langle\sigma_{\rm ann}v\rangle_{\rm f}$ is large enough, then DM particles will reach chemical equilibrium in the pre-EMD phase but can decouple at $H \gtrsim H_{\rm tran}$, which we call the "early-equilibrium" regime. The condition on $\langle\sigma_{\rm ann}v\rangle_{\rm f}$ to be in either of these regimes is given in Eqs. (C.1) and (C.5) of Appendix C:

$$\begin{aligned}
\langle\sigma_{\rm ann}v\rangle_{\rm f} &\ll \frac{\pi^3 g_{*\rm reh}^{1/2}}{\sqrt{90}\zeta(3)M_{\rm P}T_{\rm reh}} \qquad (\textbf{decoupling})\,, \\
\langle\sigma_{\rm ann}v\rangle_{\rm f} &\gtrsim \frac{\pi^3 g_{*\rm reh}^{1/2}}{\sqrt{90}\zeta(3)M_{\rm P}T_{\rm reh}} \qquad (\textbf{early-equilibrium})\,. \qquad (4.6)
\end{aligned}$$

The pre-EMD contribution to the DM abundance follows from Eqs. (C.4) and (C.7):

$$\left(\Omega_\chi h^2\right)^{(\text{pre-EMD})}_{\text{freeze-in}} \simeq \begin{cases} \dfrac{0.028}{g_{*\text{reh}}^{5/4} g_{*0}^{1/4}} \left\langle \sigma_{\text{ann}} v \right\rangle_{\text{f}} M_{\text{P}} \left(\dfrac{m_\chi}{1\,\text{GeV}}\right) \left(\dfrac{10^9 T_{\text{reh}} T_{\text{R}}}{T_0}\right) & (\textbf{decoupling})\,, \\ \dfrac{0.076}{g_{*\text{dec}}} \left(\dfrac{m_\chi}{1\,\text{GeV}}\right) \left(\dfrac{10^9 T_{\text{R}}}{T_0}\right) & (\textbf{early-equilibrium})\,. \end{cases} \tag{4.7}$$

We will now underline some important differences between the pre-EMD and late-EMD components of the relic abundance given in Eqs. (4.7) and (4.2) respectively:

- The pre-EMD component depends on $T_0$ and $T_{\text{reh}}$ in addition to $T_{\text{R}}$. Freeze-in during pre-EMD is most efficient at the highest temperature in that era, which explains the appearance of $T_{\text{reh}}$ in the first expression of Eq. (4.7). Since DM particles start in chemical equilibrium in the early-equilibrium regime, the second expression in Eq. (4.7) is independent of $T_{\text{reh}}$. The factor $T_{\text{R}}/T_0$ appears in both cases indicating dilution by entropy generation during the EMD epoch.

- The pre-EMD component is proportional to $m_\chi$. This can be understood by noting that the bulk of DM production in the pre-EMD phase occurs when $T \gg m_\chi$. Therefore, the resulting DM number density, see Eqs. (C.4) and (C.7), is independent of $m_\chi$.

- The pre-EMD component has no explicit dependence on $\langle \sigma_{\text{ann}} v \rangle_{\text{f}}$ in the early-equilibrium regime because DM particles start in chemical equilibrium. The only role of $\langle \sigma_{\text{ann}} v \rangle_{\text{f}}$ in this case is to determine the decoupling temperature $T_{\text{dec}}$, which results in an implicit dependence through $g_{*\text{dec}}$.

- The pre-EMD component has a much milder dependence on $T_{\text{R}}$ and $m_\chi$ than the late-EMD component. As a result, moderate changes in these parameters can render the latter totally negligible, significantly affecting the allowed parameter space. This will become clear when we present our results in the next section.

## 4.3 Results

We numerically solve the set of Boltzmann equations governing the evolution of radiation, r, the decaying component driving EMD, $\phi$, and DM particles, $\chi$:

$$\begin{aligned}
\dot{\rho}_{\rm r} + 4H\rho_{\rm r} &= \Gamma_\phi \rho_\phi - \langle E_\chi \rangle \langle \sigma_{\rm ann} v \rangle_{\rm f} \left( n_{\chi,{\rm eq}}^2 - n_\chi^2 \right) \\
\dot{\rho}_\phi + 3H\rho_\phi &= -\Gamma_\phi \rho_\phi \\
\dot{n}_\chi + 3Hn_\chi &= \langle \sigma_{\rm ann} v \rangle_{\rm f} \left( n_{\chi,{\rm eq}}^2 - n_\chi^2 \right)
\end{aligned} \tag{4.8}$$

where $\Gamma_\phi$ is the decay rate of $\phi$, $\langle E_\chi \rangle \approx \left( m_\chi^2 + 9T^2 \right)^{1/2}$ is the average energy per DM particle[6], and $n_{\chi,{\rm eq}}$ denotes the thermal equilibrium value of the DM number density. As in the previous chapter, the energy density in $\phi$ is tracked until it is sufficiently small to be unimportant for the subsequent evolution, and is then dropped to facilitate faster numerical calculation. We account for the detailed temperature dependence of the $g_*$ factor as shown in Appendix A. In order to calculate the DM relic abundance, we normalize the DM number density with the entropy density long after the end of the EMD epoch.

As before, we investigate the parameter space in the $m_\chi - \langle \sigma_{\rm ann} v \rangle_{\rm f}$ plane that yields the correct DM abundance for various values of $T_{\rm R}$, $T_0$, and $T_{\rm reh}$. In each case, we use the contribution to the relic abundance from the entropy-producing phase of EMD as a baseline for comparison.

In Figure 4.2, we show the curve that represents points for which $(\Omega_\chi h^2)^{\rm (tot)} = (\Omega_\chi h^2)^{\rm (late\text{-}EMD)} + (\Omega_\chi h^2)^{\rm (pre\text{-}EMD)}$ reproduces the observed DM abundance for $T_{\rm reh} = 10^{12}\,{\rm GeV}$, $T_0 = 10^{10}\,{\rm GeV}$, and $T_{\rm R} = 10\,{\rm GeV}$. The curve consists of three distinct regions, 1, 2, and 3, as follows:

[6]The contribution of this term to the radiation energy density is typically very small, even when $n_{\chi,{\rm eq}} \gg n_\chi$, and hence the exact form of $\langle E_\chi \rangle$ is not important for the overall evolution.

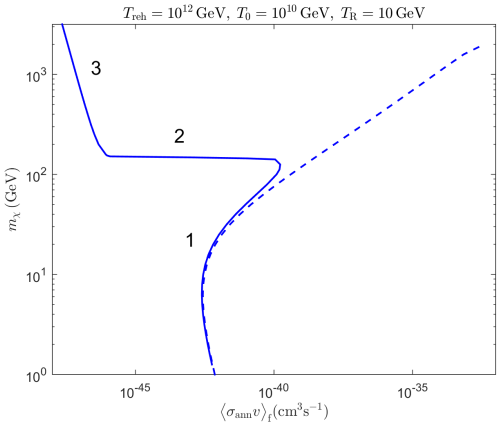


Figure 4.2: Values of $m_\chi$ and $\langle\sigma_{\rm ann}v\rangle_{\rm f}$ that yield the DM relic abundance of $\Omega_\chi h^2 \approx 0.12$, obtained by numerical solution of the Boltzmann equations in Eq. (4.8). The solid curve corresponds to production during the entire thermal history shown in Figure 4.1, while the dashed curve depicts the freeze-in side of the corresponding baseline curve from production in the entropy-generating phase of EMD alone. In region 1, the DM relic abundance is dominated by the late EMD contribution, while the early-equilibrium and decoupling regimes of the pre-EMD contribution dominate in regions 2 and 3, respectively. The transition to freeze-out of the baseline curve is seen to begin at the top-right corner.

(**1**) Region 1 starts at small DM masses and initially follows the baseline curve, but moves above it as $m_\chi$ and $\langle\sigma_{\rm ann}v\rangle_{\rm f}$ increase. This behavior can be understood from the analytical approximations in Eqs. (4.2) and (4.7). The late-EMD component dominates at small masses due to its scaling $\propto m_\chi^{-5}$. As $m_\chi$ and $\langle\sigma_{\rm ann}v\rangle_{\rm f}$ both increase along the baseline curve, the pre-EMD component of Eq. (4.7) becomes more relevant. Obtaining the correct DM abundance then requires a larger $m_\chi$ than the late-EMD component alone, and hence the $(\Omega_\chi h^2)^{(\rm tot)}$ curve goes above the baseline.

(**2**) Region 2 starts at the turning point (the abrupt departure from the baseline curve) and extends to very small values of $\langle\sigma_{\rm ann}v\rangle_{\rm f}$. It is essentially horizontal for the following reason. In this region, the pre-EMD component dominates and $\langle\sigma_{\rm ann}v\rangle_{\rm f}$ is large enough that we are in the early-equilibrium regime. The relic abundance is then given by the second expression in Eq. (4.7), which is

almost independent of $\langle\sigma_{\rm ann}v\rangle_{\rm f}$. However, region 2 is not exactly horizontal as $(\Omega_\chi h^2)^{\rm (late\text{-}EMD)}$ brings in a very mild $m_\chi$ dependence that is too small to be noticeable in the figure.

**(3)** Region 3 starts at the point where $\langle\sigma_{\rm ann}v\rangle_{\rm f} \sim 3g_{*\rm reh}^{1/2}\,(T_{\rm reh}M_{\rm P})^{-1}$ and rises toward larger values of $m_\chi$ as $\langle\sigma_{\rm ann}v\rangle_{\rm f}$ decreases. In this region, $\langle\sigma_{\rm ann}v\rangle_{\rm f}$ is so small that production of DM particles in the pre-EMD phase occurs in the decoupling regime. As a result, the DM relic abundance is dominated by the pre-EMD component and follows the first expression in Eq. (4.7).

Figures 4.3 and 4.4 depict the sensitivity of the allowed parameter space on the postinflationary history. In Figure 4.3, we show variation of the curve from Figure 4.2 for different values of $T_0$ for fixed $T_{\rm R}$ and $T_{\rm reh}$ (left panel), and for different values of $T_{\rm R}$ when $T_0$ and $T_{\rm reh}$ are kept constant (right panel). Figure 4.4, shows the change in the curve when $T_{\rm reh}$ is varied for fixed $T_{\rm R}$ and $T_0$. We observe the following main features in the figures:

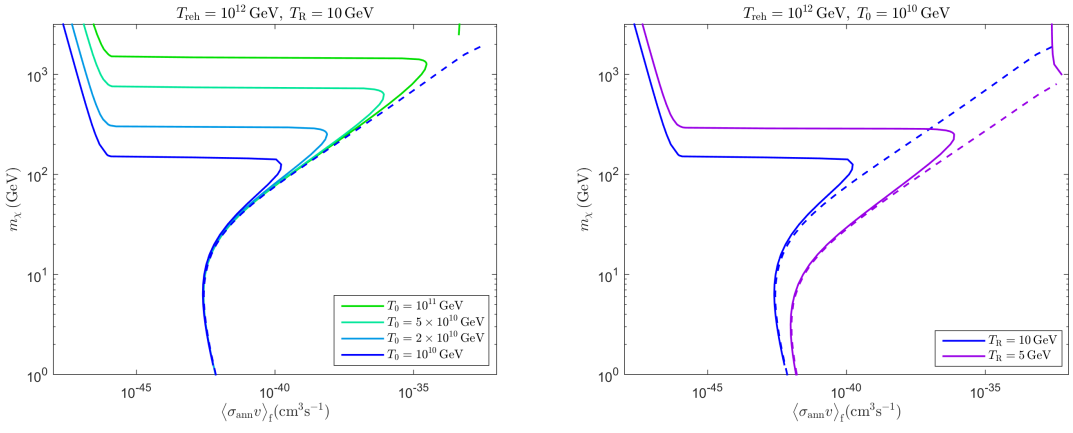


Figure 4.3: Variation of the curve from Figure 4.2 for different values of $T_{\rm R}$ and $T_0$. Left: variation of $T_0$ for constant $T_{\rm reh}$ and $T_{\rm R}$. Right: variation of $T_{\rm R}$ for constant $T_{\rm reh}$ and $T_0$. Note the appearance of the freeze-out side, at the top right corner, which merges with the peak of the corresponding baseline curve.

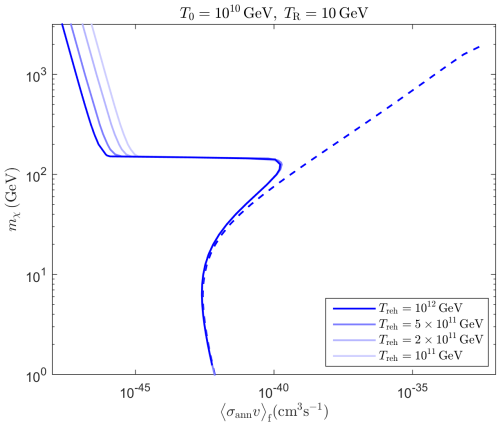


Figure 4.4: Variation of the curve from Figure 4.2 for different values of $T_\mathrm{reh}$ while holding $T_\mathrm{R}$ and $T_0$ constant.

- In Figure 4.3, region 2 moves up with increasing $T_0$ and down with increasing $T_\mathrm{R}$, while there is no change when $T_\mathrm{reh}$ varies in Figure 4.4. Since pre-EMD production in the early-equilibrium regime dominates in this region, we expect $m_\chi \propto T_0/T_\mathrm{R}$, independent of $T_\mathrm{reh}$, which agrees with the figures.
- The turning point is highly dependent on $T_\mathrm{R}$ and $T_0$, as seen in Figure 4.3, but does not change with $T_\mathrm{reh}$ in Figure 4.4. Its position can be estimated by setting the sum of the late-EMD component in Eq. (4.2) and the second expression in Eq. (4.7) equal to the observed DM abundance and finding the local maximum of $\langle\sigma_\mathrm{ann}v\rangle_\mathrm{f}$ in terms of $m_\chi$. As it turns out, $\langle\sigma_\mathrm{ann}v\rangle_\mathrm{f} \propto T_0^5 T_\mathrm{R}^{-12}$ at the turning point. This is in agreement with the considerable horizontal movement (especially when $T_\mathrm{R}$ changes) in Figure 4.3. As expected, the vertical shift follows that of region 2 mentioned above.
- The left end of region 2, where it meets region 3, moves horizontally with changing $T_\mathrm{reh}$ in Figure 4.4, and vertically when $T_0$ and $T_\mathrm{R}$ are varied in Figure 4.3. This point divides the decoupling and early-equilibrium regimes of the pre-EMD contribution, where we have $\langle\sigma_\mathrm{ann}v\rangle_\mathrm{f} \propto T_\mathrm{reh}^{-1}$, which explains the horizontal movement. As expected, the dependence on $T_0$ and $T_\mathrm{R}$ follows that of region 2.

A very important point is that pre-EMD production opens up vast regions of the parameter space at very small $\langle\sigma_{\rm ann}v\rangle_{\rm f}$ that are not allowed when the EMD component alone is considered. In fact, the freeze-in side of the baseline curve does not extend below a certain value of $\langle\sigma_{\rm ann}v\rangle_{\rm f}$. This is because lowering $\langle\sigma_{\rm ann}v\rangle_{\rm f}$ results in a smaller $m_\chi$ in order to obtain the correct relic abundance. However, once $T_{\rm f} \sim m_\chi/4$ drops below $T_{\rm R}$, the contribution to the relic abundance from RD after EMD becomes important. This sets a lower bound on $\langle\sigma_{\rm ann}v\rangle_{\rm f}$, for a given $T_{\rm R}$, beyond which the baseline curve does not extend. Nevertheless, the pre-EMD contribution can still dominate for such small $m_\chi$ and $\langle\sigma_{\rm ann}v\rangle_{\rm f}$, especially for combinations of the parameters that lower region 2, such as $T_{\rm reh} = 10^{12}\,{\rm GeV}$, $T_0 = 10^8\,{\rm GeV}$, and $T_{\rm R} = 10\,{\rm GeV}$.

For the values of $T_0$ and $T_{\rm R}$ in Figures 4.2-4.4, the pre-EMD component leads to a separation of the freeze-in and freeze-out parts of the allowed parameter space by a horizontal gap. Though the freeze-out part is not affected as much as the freeze-in part, and generally lies to the right of the figures, we include a short segment at the top right corner of Figure 4.3 for reference. Decreasing $T_{\rm R}$ and/or increasing $T_0$ results in a growing overlap between region 1 and the baseline curve, and a significant movement of the turning point to the right, making region 2 larger. However, the turning point cannot go beyond the peak of the baseline curve because larger values of $\langle\sigma_{\rm ann}v\rangle_{\rm f}$ actually give rise to freeze-out. Similarly, the freeze-out side moves toward the left and up with decreasing (increasing) $T_{\rm R}$ ($T_0$).

At some point, the freeze-in and freeze-out parts join and region 1 coincides with the freeze-in side of the baseline curve, while region 2 splits away. By further decreasing $T_{\rm R}$ and/or increasing $T_0$, the allowed parameter space is again divided into two disjointed parts that are now separated by a vertical gap. We clearly see this in Figure 4.5 where the smaller two values of $T_{\rm R}$ have fully split from the baseline curve. For these two, region 1 follows the full baseline curve, including the freeze-out side which is not shown. The upper segments include regions 2 and 3, discussed

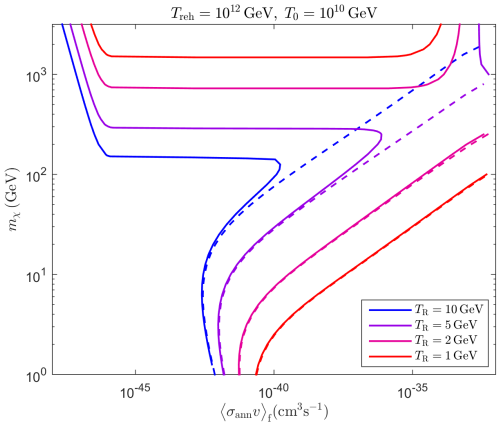


Figure 4.5: Variation of $T_{\rm R}$, with constant $T_{\rm reh}$ and $T_0$, for values that display the transition between the horizontal gap and vertical gap behavior described in the text. For the larger two values of $T_{\rm R}$, the solid curves are separated into a freeze-in part on the left and a freeze-out part on the right (which we do not show apart from the top right corner). For the two smaller values, the curves are split into a lower part that follows the baseline curve and an upper part that connects the freeze-in and freeze-out sides.

above, that make a smooth transition to the freeze-out regime rising up on the right side. In summary, at higher $T_{\rm R}$ and/or lower $T_0$, the effect of pre-EMD production of DM is to disconnect the allowed parameter space into the freeze-in and freeze-out parts, while for lower $T_{\rm R}$ and/or higher $T_0$, it gives rise to a new curve that smoothly interpolates between the freeze-in and freeze-out regimes but is situated at larger values of $m_\chi$ compared to the baseline curve.

## 4.4 Early-equilibrium regime: a closer look

A remarkable feature observed in Figures 4.2-4.5 is that the DM relic abundance is essentially independent from $\langle\sigma_{\rm ann}v\rangle_{\rm f}$ in large parts of the parameter space. This is due to the fact that DM particles start in chemical equilibrium during the pre-EMD phase for a broad range of $\langle\sigma_{\rm ann}v\rangle_{\rm f}$. This range, corresponding to the early-equilibrium regime, spans over many orders of magnitude extending from a minimum

value determined by $T_{\rm reh}$, see Eq. (C.5), to a maximum value that depends on $T_0$ and $T_{\rm R}$ and can be as large as that at the peak of the baseline curve. This feature can be considered as the freeze-in analogue to the WIMP miracle in a complementary way: while the relic abundance mainly depends on $\langle\sigma_{\rm ann}v\rangle_{\rm f}$ for the latter, it is mostly dependent on $m_\chi$ in this case.

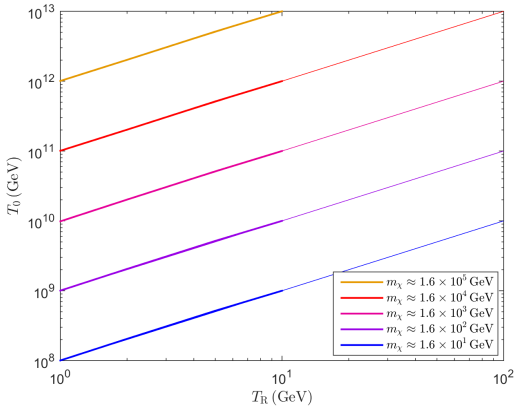


Figure 4.6: Contours of the upper bound on $m_\chi$ in the $T_0 - T_{\rm R}$ plane, in order to not overproduce DM in the early-equilibrium regime. The solid lines are obtained numerically from region 2 shown in previous figures, while the thin lines correspond to Eq. (4.9).

The DM abundance in this case is given by the second expression in Eq. (4.7). This is at most equal to the observed relic abundance as, in general, there exist other sources that contribute to the total abundance. Most notably, DM particles may be directly produced in the decay of the field(s) driving the EMD epoch [44, 45, 46, 47]. As a result, we find the following inequality in order to not overproduce DM:

$$m_\chi \lesssim 1.6\, g_{*\rm dec} \left(\frac{T_0}{10^9 T_{\rm R}}\right) (1\,{\rm GeV})\,. \tag{4.9}$$

In Figure 4.6, we show the contours corresponding to the maximum allowed value of $m_\chi$ in the $T_0 - T_{\rm R}$ plane. The thick line segments are from full numerical calculations, while the thin lines represent the rhs of Eq. (4.9). In the latter, we have taken $g_{*\rm dec} = 106.75$, the value for the SM, which is a very good approximation for

the range of $T_{\rm R}$ and $T_0$ shown in the figure. The numerical and analytical results agree very well for the range of parameters chosen.

### 4.4.1 Connection to observables

If the two sides of Eq. (4.9) can be connected to experiments, then the inequality can be considered as a consistency relation of the pre-EMD early-equilibrium regime. The lhs is the DM mass, which can in principle be measured at the LHC (or future colliders) through the standard missing energy signal for the range of $m_\chi$ shown in Figures 4.2-4.5. One may also impose an upper bound on the rhs, which is a direct measure of the duration of the EMD era, in the context of inflationary cosmology.

In the nonstandard history we have considered here, the number of e-folds of inflation between the time when cosmologically relevant perturbations, corresponding to the pivot scale $k_* = 0.05\,{\rm Mpc}^{-1}$, left the horizon and the end of inflation can be written as [48, 49]:

$$N_{k_*} \approx 57.6 + \frac{1}{4}\ln r - \Delta N_{\rm reh} - \Delta N_{\rm EMD}\,, \tag{4.10}$$

where:

$$\Delta N_{\rm reh} \equiv \frac{1-3w_{\rm reh}}{6(1+w_{\rm reh})}\,\ln\left(\frac{H_{\rm inf}}{H_{\rm reh}}\right) \quad , \quad \Delta N_{\rm EMD} \equiv \frac{1}{6}\ln\left(\frac{H_0}{H_{\rm R}}\right). \tag{4.11}$$

Here, $H_{\rm inf}$ is the Hubble rate during inflation, $r$ is the tensor-to-scalar ratio, and $w_{\rm reh}$ represents the equation of state during inflationary reheating. Using the relation between $H$ and $T$ at the onset and the end of the EMD epoch, we can write:

$$\Delta N_{\rm EMD} \simeq \frac{1}{3}\ln\left(\frac{T_0}{T_{\rm R}}\right) + \frac{1}{12}\ln\left(\frac{g_{*0}}{g_{*\rm R}}\right). \tag{4.12}$$

Theoretical arguments and numerical simulations suggest that generally $0 \leq w_{\rm reh} \leq 1/3$ [50, 51], which implies that $\Delta N_{\rm reh} \geq 0$. Combined with the experimental bound $r < 1$ [52], and the typical range of values for $g_{*0}$ and $g_{*\rm R}$, we find:

$$\ln\left(\frac{T_0}{T_{\rm R}}\right) \lesssim 173 - 3N_{k_*}\,. \tag{4.13}$$

In general, $N_{k_*}$ is related to the scalar spectral index $n_{\rm s}$ that is constrained by the cosmic microwave background (CMB) experiments. In particular, there are simple relations between $N_{k_*}$ and $n_{\rm s}$ [53] in two important universality classes of single-field models of inflation that include a large number of models compatible with the latest Planck results [52]. One can therefore use the experimental bounds on $n_{\rm s}$ to impose a lower limit on $N_{k_*}$ and, through Eq. (4.13), an upper limit on $T_0/T_{\rm R}$ [54].

In addition, one may use the spectrum of primordial gravitational waves to further constrain the rhs of Eq. (4.9). The initial spectrum of gravitational waves produced during inflation depends on $r$ and the tensor spectral index $n_{\rm T}$. However, their subsequent evolution depends on the postinflationary thermal history and is in particular affected by an epoch of EMD [55, 56] (also, see [57, 58, 59]). Tensor modes that enter the horizon during EMD, and the modes that are already at subhorizon scales, experience a suppression, compared to a standard thermal history, due to entropy generation in this epoch. As a result, the shape of the tensor spectrum is sensitive to the beginning and end of the EMD phase, equivalently $T_0$ and $T_{\rm R}$. This is complementary to the information from the scalar spectral index, mentioned above, which only depends on the duration of the EMD period encoded in $T_0/T_{\rm R}$. Therefore, if $r$ is not much smaller than the current experimental bound $r_{\rm max} \simeq 0.064$ [52], a future detection by (or limits from) the gravitational wave detectors could further constrain the allowed regions in the $T_0 - T_{\rm R}$ plane.

We note that because of the very small value of $\langle \sigma_{\rm ann} v \rangle_{\rm f}$ in the early-equilibrium regime, see Figures 4.2-4.5, there is no realistic prospect for a detectable signal from indirect detection searches. For the same reason, one can expect that this regime will also escape direct detection. However, with the help of Eq. (4.9), a combination of collider experiments and cosmological observations could be used as an indirect test of this otherwise elusive scenario.

### 4.4.2 An example

We now discuss a specific particle physics scenario of EMD to see how the inequality in Eq. (4.9) is translated into constraints on the underlying model parameters. As mentioned before, moduli that arise in string theory are natural candidates for driving a period of EMD [18]. Consider a modulus field $\phi$ with mass $m_\phi$. It has gravitationally suppressed coupling to other fields resulting in a decay width:

$$\Gamma_\phi = \frac{c}{2\pi}\frac{m_\phi^3}{M_{\rm P}^2}, \tag{4.14}$$

where typically $c \sim \mathcal{O}(0.1)$.

The modulus $\phi$ gets displaced from the minimum of its potential during inflation, and starts oscillating about it when $H \simeq m_\phi$, with initial amplitude $\phi_{\rm i} \gtrsim \mathcal{O}(0.1 M_{\rm P})$ (see Appendix A). This implies that $\phi$ oscillations, which behave like matter, dominate the Universe shortly after their start, hence $H_0 \lesssim m_\phi$. Oscillations eventually decay when $H \simeq \Gamma_\phi$ and establish a RD Universe with temperature $T_{\rm R}$ [7]. Since the Universe is approximately RD at the onset and the end of the EMD phase, and after using Eq. (4.14) with $c \sim 0.1$, the inequality in Eq. (4.9) can now be written as:

$$m_\chi \lesssim 120\, g_{*\rm dec} \left(\frac{g_{*\rm R}}{g_{*0}}\right)^{1/4} \left(\frac{M_{\rm P}}{10^{10} m_\phi}\right) (1\,{\rm GeV}), \tag{4.15}$$

where the rhs is basically controlled by $m_\phi$.

In Figure 4.7, we show the allowed region of the $m_\chi - m_\phi$ plane accordingly. The curve depicts the upper bound of Eq. (4.15), obtained from full numerical calculations. We have taken $g_{*0} = 106.75$ corresponding to the high values of $T_0$. Including new degrees of freedom beyond the SM (for example $g_{*0} = 228.75$, as in its minimal supersymmetric extension) will shift the curve slightly. Note that the slope of the curve does change, as expected, due to the implicit dependence of $g_{*\rm R}$ on $m_\phi$ when $T_{\rm R}$ drops below the electroweak scale.

[7] Explicit examples in the context of flux compactifications where $\phi$ is the volume modulus are discussed in [60, 61]

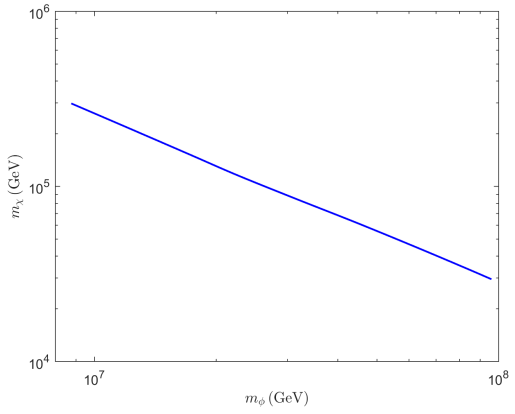


Figure 4.7: Upper bound on the DM mass $m_\chi$ for a given modulus mass $m_\phi$ in the case of modulus-driven EMD. The curve is obtained numerically from the early-equilibrium regime.

## 4.5 Discussion and conclusion

We now turn to discussing how our results may be extended to more general situations that involve a nonstandard thermal history.

Throughout this chapter, we have considered a nonstandard thermal history where the EMD epoch is preceded by a RD phase established at the end of inflationary reheating. However, for a very slowly decaying inflaton, the field(s) driving EMD may have comparable energy density to the inflaton before reheating completes. An example is a modulus-driven EMD scenario with $H_{\rm reh} \ll m_\phi$ [8]. In this case, the Universe does not enter a truly RD phase at the end of inflationary reheating but rather a phase where the energy density of the radiation and matter components are roughly equal. One may approximate this case by taking $T_{\rm reh} = T_0$ in the nonstandard thermal history considered here. We have checked that full numerical calculations are in very good agreement with this approximation. Such a scenario is also of the two-field type, discussed in Chapter 3, where the two matter-components have equal initial energy densities. We note that the freeze-in and freeze-out sides of the curves

[8]For an explicit model, see [62].

in Figures 4.2-4.5 are thus expected to merge at very high DM masses, $m_\chi > T_0$, mimicking the shape of the baseline curve, though offset to smaller $\langle\sigma_{\rm ann}v\rangle_{\rm f}$.

A general postinflationary thermal history may include multiple epochs of EMD with respective parameters $T_{0,i}$ and $T_{{\rm R},i}$, $1 \leq i \leq n$, separated by intermediate RD phases. Because of the temperature dependence discussed in Appendix C, the late-EMD component of the DM relic abundance is mainly due to production in the last (i.e., $n$-th) bout of EMD. This implies that $T_{\rm R}$ must be replaced by $T_{{\rm R},n}$ in Eq. (4.2). The pre-EMD component, in the decoupling regime, is dominated by production at temperature $T_{\rm reh}$, while in the early-equilibrium regime, it is set at temperature $T_{\rm dec}$ when chemical decoupling of DM particles occurs. Hence, the main modification to the expressions in Eq. (4.7) is replacing $T_{\rm R}/T_0$ with the product of $T_{{\rm R},i}/T_{0,i}$ to take all relevant EMD periods into account.

As mentioned at the beginning of Section 4.2, we have assumed $\langle\sigma_{\rm ann}v\rangle_{\rm f}$ to be constant within the temperature range of interest. In general, however, $\langle\sigma_{\rm ann}v\rangle_{\rm f}$ can have a temperature dependence. Then, any allowed $\langle\sigma_{\rm ann}v\rangle_{\rm f}$ in Figures 4.2-4.5 must be considered as the value of $\langle\sigma_{\rm ann}v\rangle(T)$ at the relevant temperature: i.e., $T \sim m_\chi/4$ for region 1, $T \simeq T_{\rm dec}$ for region 2, and $T \simeq T_{\rm reh}$ for region 3 in those figures. In cases where $\langle\sigma_{\rm ann}v\rangle(T) \propto T^n$ with $n > 0$ (such as the model studied in [63]), the pre-EMD production of DM particles will be enhanced compared to our calculations. The pre-EMD component of the relic abundance can be larger in this case thereby affecting the allowed parameter space even more prominently than shown in Figures 4.2-4.5.

In conclusion, early stages in nonstandard thermal histories that include a period of EMD can significantly affect nonthermal production of DM via freeze-in for weak scale DM masses. We have demonstrated this in a postinflationary history involving an early RD phase followed by an EMD epoch that reheats the Universe to a temperature $T_{\rm R}$ before BBN. In the case where $\langle\sigma_{\rm ann}v\rangle_{\rm f}$ is constant over the temperature range of interest, the pre-EMD component of the DM relic abundance depends on

the temperature at the onset of the EMD phase $T_0$ and the reheating temperature after inflation $T_{\rm reh}$, in addition to $T_{\rm R}$. This opens up vast regions of the $m_\chi - \langle\sigma_{\rm ann}v\rangle_{\rm f}$ plane where pre-EMD production can totally dominate the relic abundance as shown in Figures 4.2-4.5.

Moreover, DM particles reach chemical equilibrium in the pre-EMD era for a very broad range of $\langle\sigma_{\rm ann}v\rangle_{\rm f}$ spanning over many decades. The relic abundance in this case is virtually independent of $\langle\sigma_{\rm ann}v\rangle_{\rm f}$, and avoiding DM overproduction yields an inequality between $m_\chi$ and $T_0/T_{\rm R}$. This brings an interesting possibility of combining collider searches (to measure $m_\chi$) with CMB and gravitational wave detector experiments (to constrain $T_0/T_{\rm R}$) to test an elusive scenario that escapes indirect and direct detection.

# Chapter 5

# Nonthermal Dark Matter from Primordial Black Holes

## 5.1 Introduction

Up until this point, we have considered the details of EMD and their effect on freeze-out and freeze-in production of DM. The results of those considerations are important to generic nonthermal DM production scenarios because they define regions in parameter space corresponding to the over/underproduction of DM. Any other source of DM, such as the direct decay of some additional component, must not push the resultant relic abundance over the observed value, and can therefore only be viable in cases where DM is otherwise underproduced. For this reason, the details of freeze-out/in production are relevant for direct production scenarios as they constrain the allowed values of parameters such as the DM annihilation rate. In this chapter, we will present such a direct production scenario involving the evaporation of primordial black holes.[1]

[1]The contents of this chapter are published in a modified form as R. Allahverdi, J. Dent, and J. Osinski, Phys. Rev. D 97, 055013 (2018), and are used with permission [64].

As WIMP detection remains elusive, alternative models in which DM is not a WIMP-like particle have attracted significant attention in recent years (for example, see [65]). One alternative is that DM, instead of being an elementary particle, is (at least partially) composed of primordial black holes (PBHs) [66, 67] formed in the early Universe.[2] PBHs with a mass $\gtrsim 10^{15}\,\mathrm{g}$ would not have evaporated by the present time, and may, in principle, constitute a fraction, if not all, of the DM in the Universe. While this possibility has been a subject of study for a long time, the recent discovery of gravitational waves (GW) by the Advanced LIGO group has led to intensified efforts to constrain a possible PBH population.[3] A great deal of work has also been devoted to mechanisms for amplifying density perturbations toward the end of inflation to allow production of PBHs [123, 124, 125, 126, 127, 128, 129, 130, 131].

In this chapter, we study a scenario where PBHs are responsible for nonthermal production of DM, including the possibility of producing the entirety of the relic abundance. This scenario involves a period of EMD that leads to formation of PBHs within an extended mass range. The subsequent evaporation of PBHs in the ensuing RD phase creates DM particles after thermal freeze-out or freeze-in but prior to BBN. Evading tight observational constraints for evaporation after BBN sets an upper bound of $\simeq 2 \times 10^8\,\mathrm{g}$ on the maximum mass $M_{\mathrm{max}}$ of PBHs thus formed. We

[2]For other early works as well as some reviews, see [68, 69, 70, 71, 72, 73].

[3]This includes examination of the LIGO measurement and constraints on the PBH mass distribution (including the possibility of an extended mass range) and merger rate [3, 74, 75, 76, 77, 78, 79, 80, 81], general signatures of exotic compact objects [82], possible PBH progenitors [83, 84], future GW searches and expectations [85, 86, 87, 88, 89, 90] including those for a GW background [91, 92, 93, 94, 95, 96, 97]. Many other constraints on the existence and effects of PBHs have been recently re-examined, with new constraints proposed including those from dynamical effects in dwarf galaxies [98, 99], radio and X-ray sources [100, 101], CMB measurements [102, 103, 104, 105, 106, 107], ionization history [108], quasar microlensing [109], neutron star capture [110], lensing of radio bursts [111], near infrared and cosmic infrared background [112], 21 cm measurements [113], current and future pulsar timing arrays [114, 115, 116], lensing for intermediate mass PBHs [117], future strong lensing tests [118], orbital eccentricity determination [119], spin distribution evaluation [120], spatial clustering [121] along with effects of astrophysical uncertainties on PBH constraints [122].

show that the correct DM relic abundance can be obtained within the DM mass range $m_\chi = 100\,\mathrm{GeV} - 10\,\mathrm{TeV}$, provided that the scalar power spectrum at small scales (relevant for PBH formation) is enhanced by a factor $\mathcal{O}(10^5)$ relative to its value at scales probed by the cosmic microwave background (CMB) experiments. The upper limit on $M_{\max}$ implies that the transition from EMD to RD should occur when the Hubble expansion rate is $H_{\mathrm{R}} \gtrsim \mathcal{O}(100)\,\mathrm{GeV}$. The entire observed DM abundance can then be accommodated in cases when thermal freeze-out or freeze-in lead to underproduction of DM.

We show that the required enhancement of the power spectrum is compatible with the Planck 2015 limits on the scalar spectral index and its running within $2\sigma$ (for previous work on PBHs in the context of a running spectral index, see [132, 133]). Such amplification is also attainable, for example, in models where the inflaton undergoes a brief period of ultra slow-roll motion toward the end of inflation. However, we do not present an inflationary model that achieves this, as our goal in this chapter is to discuss the main ingredients for nonthermal DM production via evaporation of PBHs and identify the allowed parameter space.

The rest of this chapter is organized as follows. In Section 5.2, we briefly review PBH production in the early Universe in both a RD and EMD phase, focusing on the latter. In Section 5.3, we discuss nonthermal DM production via evaporation of PBHs. We present the main results in Section 5.4, and we close with a brief discussion and conclusion in Section 5.5. Appendix D includes some calculational details of our results.

## 5.2 PBH formation in early matter domination

PBHs are postulated to form from density fluctuations in the postinflationary early Universe. In the standard cosmology, the Universe existed in a RD stage after the

reheating process that followed inflation, and remained so until matter-radiation equality was reached in the post-BBN and pre-CMB era. However, as mentioned in previous chapters, it is possible that there existed a period of EMD that ended before the onset of BBN.

It is well known that density fluctuations exhibit remarkably different growth behavior depending on the form of the dominant background energy component, be it radiation or matter. Here we will briefly review the formation of PBHs in these two different background scenarios, and will then explore some of the consequences of PBH formation in the context of an EMD scenario (for some other works on EMD and PBH see, for example, [68, 69, 105, 134]).

In the case of a RD Universe, a density fluctuation of $\mathcal{O}(1)$ would need to overcome the radiative pressure and thus would have a characteristic size on the order of the scale of the horizon. Assuming a Gaussian perturbation profile with root-mean-square amplitude $\delta(M)$, the fractional energy density of the Universe that goes into PBHs with mass $M$ is given by [72]

$$\beta(M) \approx K\delta(M)^{2\gamma}\mathrm{erfc}\left(\frac{\delta_{\mathrm{c}}}{\sqrt{2}\delta(M)}\right), \tag{5.1}$$

where $\gamma \simeq 0.36$ [135, 136, 137, 138, 139], $K \simeq 3.3$ [140], and $\delta_{\mathrm{c}} \simeq 0.45$ [136, 137, 138] (see [141] for a smaller value of $\delta_c$) We note that after PBH formation $\beta$ increases $\propto a(t)$ during RD, where $a(t)$ is the scale factor.

However, the situation is altered if PBH formation takes place during a period of EMD. In this case one arrives at [68, 69]

$$\beta(M) \approx 2 \times 10^{-2}\delta^{13/2}(M)\,, \tag{5.2}$$

where $\delta(M)$ denotes the amplitude of perturbations for a mode that eventually collapses to form PBH with mass $M$ when it enters the horizon. Such a perturbation enters the horizon when $H \approx 4\pi M_{\mathrm{P}}^2/M$. The amplitude then grows according to

$\delta \propto a \propto H^{-2/3}$ and black hole formation occurs once $\delta \sim \mathcal{O}(1)$ at

$$H_{\rm form} \approx \frac{4\pi M_{\rm P}^2}{M}\delta(M)^{3/2}\,. \tag{5.3}$$

It is important to note that subhorizon fluctuations can form black holes due to the absence of pressure in this case. We also note that $\beta$ remains constant during the EMD era.

The minimum mass of PBHs formed during the EMD era, $M_{\rm min}$, depends on the details of the thermal history between the end of inflation (characterized by $H_{\rm inf}$) and the start of the EMD era (characterized by $H_0$), namely the window $H_0 \lesssim H \lesssim H_{\rm inf}$. An absolute lower bound on $M$ can be found by noticing that the minimal inflationary fluctuation wavelength is $\sim H_{\rm inf}^{-1}$, which implies that

$$M_{\rm min} \gtrsim \frac{4\pi M_{\rm P}^2}{H_{\rm inf}}\,. \tag{5.4}$$

The maximum mass $M_{\rm max}$ corresponds to the mode whose amplitude reaches $\mathcal{O}(1)$ at the end of the EMD epoch, which results in

$$M_{\rm max} \approx \frac{4\pi M_{\rm P}^2}{H_{\rm R}}\delta(M_{\rm max})^{3/2}\,, \tag{5.5}$$

where $H_{\rm R}$ denotes the Hubble rate when the EMD epoch ends and the Universe enters the RD phase. In order to avoid very tight post-BBN constraints on the evaporation of PBHs (for example, see [71]), we require that all PBHs formed during the EMD era evaporate before BBN. As we will see, from Eq. (5.6) in the next section, this results in an upper bound of $M_{\rm max} \lesssim 2 \times 10^8\,{\rm g}$.

One comment is in order before moving to the next section. Since the transition from EMD to RD is not instantaneous, one should not take the above expression for $M_{\rm max}$ as exact. The spectrum of PBHs formed during EMD is not suddenly cut off at $M_{\rm max}$. Instead, there is a quick drop in $\beta(M)$ around $M_{\rm max}$ signifying the transition from EMD to RD. In fact, PBHs with a mass (much) larger than $M_{\rm max}$ may form in the following RD phase from the collapse of fluctuation modes that enter the

horizon then. However, the abundance of such PBHs is extremely suppressed due to its exponential dependence on $\delta(M)$ as seen in Eq. (5.1). Therefore, $M_{\rm max}$ provides a good approximation of the mass above which PBH formation during EMD ceases to be important.

## 5.3 Nonthermal dark matter production from PBH evaporation

Here we study a scenario in which the entire DM relic abundance is due to the evaporation of PBHs, formed during an epoch of EMD, via Hawking radiation. In passing, we note that PBHs formed in a RD phase can also produce DM particles, however, the exponential dependence of $\beta(M)$ on $\delta(M)$ in this case implies that a parametrically larger $\delta(M)$ and a higher level of tuning are needed in order to obtain the correct DM relic abundance. For this reason, we focus on DM production from PBHs formed in an EMD phase.

PBHs with mass $M$ evaporate via Hawking radiation [142] and have a lifetime

$$t_{\rm eva} = \frac{80 M^3}{\pi M_{\rm P}^4}\,, \tag{5.6}$$

giving rise to particles with a thermal spectrum at the Hawking temperature,

$$T_{\rm H} = \frac{M_{\rm P}^2}{M}\,. \tag{5.7}$$

Evaporation of PBHs produces all particles that have a mass below their corresponding Hawking temperature. This implies that DM particles will also be produced as long as $m_{\rm DM} \ll T_{\rm H}$ [143]. For $M_{\rm max} \lesssim 2\times 10^8\,{\rm g}$, we have $T_{\rm H} \gtrsim 50\,{\rm TeV}$, therefore implying production of particles lighter than $\sim 50\,{\rm TeV}$. [4]

[4]This includes possible unwanted relics whose late decay may ruin the success of BBN, which leads to constraints on $\beta(M)$ [144, 145].

PBHs with mass $M_{\rm max} \approx 2 \times 10^8\,{\rm g}$ evaporate in the RD phase of the Universe at a temperature $T_{\rm BBN} \approx 1\,{\rm MeV}$. This late process can be responsible for the entire observed DM relic abundance in cases where thermal freeze-out or freeze-in lead to underproduction of DM. Thermal underproduction in a RD Universe via freeze-out occurs for WIMPs with a large annihilation rate $\langle\sigma_{\rm ann} v\rangle_{\rm f} > 3 \times 10^{-26}\,{\rm cm}^3 s^{-1}$,[5] while for freeze-in, underproduction can happen if DM has extremely weak coupling to SM particles, perhaps even gravitationally suppressed interactions resulting in a very small annihilation cross-section $\sigma_{\rm ann} \sim M_{\rm P}^{-2}$.

From the conservation of energy, and assuming that there is no other entropy generating process after the transition from EMD to RD, evaporation of PBHs with mass $M$ results in a DM abundance,

$$\left(\frac{n_\chi}{s}\right)_M \approx {\rm Br}_\chi \left(\frac{n_{\rm PBH}(M)}{s}\right)\left(\frac{M}{T_{\rm H}}\right) = {\rm Br}_\chi \left(\frac{n_{\rm PBH}(M)}{s}\right)\left(\frac{M}{M_{\rm P}}\right)^2 , \tag{5.8}$$

where $n_{\rm PBH}(M)$ and $s$ are the number density of PBHs and the entropy density in the RD phase respectively. ${\rm Br}_\chi$ denotes the fraction of energy density in PBHs that goes into DM particles. For supersymmetric (SUSY) DM, we have ${\rm Br}_\chi \sim 1$ in the case that all SUSY particles have a mass below $T_{\rm H}$ because all SM particles and their SUSY partners are produced from PBH evaporation, with the latter eventually decaying to DM. However, ${\rm Br}_\chi < 1$ if some of the SUSY particles have a mass above $T_{\rm H}$. In the case that DM interacts extremely weakly with the SM and SUSY particles, ${\rm Br}_\chi$ can be as small as $\mathcal{O}(10^{-2})$ based on direct production of DM along with all SM and SUSY degrees of freedom from PBH evaporation.

The parameter $\beta(M)$ is related to the DM abundance through

$$\beta(M) = \left(\frac{\rho_{\rm PBH}(M)}{\rho_{\rm tot}}\right)_{\rm R} = \frac{4M}{3T_{\rm R}}\left(\frac{n_{\rm PBH}(M)}{s}\right) , \tag{5.9}$$

[5]DM particles produced from PBH evaporation will not undergo further annihilation if $\langle\sigma_{\rm ann} v\rangle_{\rm f} < 3 \times 10^{-26}\,{\rm cm}^3 s^{-1} (T_{\rm f}/T_{\rm BBN})$, where $T_{\rm f} \sim m_{\rm DM}/20$. This is the case for DM masses up to 10 TeV as indicated by the latest Fermi-LAT constraints [13, 14].

and hence

$$\left(\frac{n_\chi}{s}\right)_M \approx \mathrm{Br}_\chi \beta(M) \left(\frac{3T_\mathrm{R}M}{4M_\mathrm{P}^2}\right) . \tag{5.10}$$

The observed DM relic abundance is

$$\left(\frac{n_\chi}{s}\right)_\mathrm{obs} \simeq 4 \times 10^{-12} \left(\frac{100\,\mathrm{GeV}}{m_\chi}\right) . \tag{5.11}$$

Requiring that the contribution from PBHs with mass $M$ does not exceed this value, and after using the previous equations, we arrive at the following relation,

$$\beta(M) \simeq 2.3 \times 10^{-26}\, \mathrm{Br}_\chi^{-1} \left(\frac{g_{*\mathrm{R}}}{106.75}\right)^{1/4} \left(\frac{10^{11}\,\mathrm{g}}{M}\right) \left(\frac{100\,\mathrm{GeV}}{m_\chi}\right) \left(\frac{M_\mathrm{P}}{H_\mathrm{R}}\right)^{1/2} . \tag{5.12}$$

We note that the similar expression in [71], which applies to the case of PBH formation in the RD phase, includes the formation temperature $T_\mathrm{i}$ instead of the reheat temperature $T_\mathrm{R}$.

In reality, all of the PBHs formed within an extended mass range during the EMD epoch will contribute to the DM relic density. However, the constraint on $\beta(M)$ becomes weaker for lighter black holes (see Eq. (5.12)). To be precise, one has to integrate over the whole relevant mass range to find the total contribution to the DM abundance. As shown in Appendix D, this integral is typically dominated by the heaviest PBHs in the mass range. We thus have

$$\beta(M_\mathrm{max}) \simeq 10^{-23}\, \mathrm{Br}_\chi^{-1} \left(\frac{g_{*\mathrm{R}}}{106.75}\right)^{1/4} \left(\frac{2 \times 10^{8}\,\mathrm{g}}{M_\mathrm{max}}\right) \left(\frac{100\,\mathrm{GeV}}{m_\chi}\right) \left(\frac{M_\mathrm{P}}{H_\mathrm{R}}\right)^{1/2} , \tag{5.13}$$

where $M_\mathrm{max}$ is normalized to the largest value for evaporation before the onset of BBN. By using Eq. (5.5), we can recast this expression in terms of $M_\mathrm{max}$ and $\delta(M_\mathrm{max})$ as

$$\beta(M_\mathrm{max}) \simeq 9 \times 10^{-24}\, \mathrm{Br}_\chi^{-1} \left(\frac{g_{*\mathrm{R}}}{106.75}\right)^{1/4} \left(\frac{2 \times 10^{8}\,\mathrm{g}}{M_\mathrm{max}}\right)^{1/2} \left(\frac{100\,\mathrm{GeV}}{m_\chi}\right) \delta(M_\mathrm{max})^{-3/4} . \tag{5.14}$$

## 5.4 Results

Equating the theoretical prediction for $\beta(M_{\rm max})$ in Eq. (5.2) with that satisfying the observational constraint in Eq. (5.14) singles out the value of $\delta(M_{\rm max})$ that is required to obtain the correct DM relic abundance for a given value of $m_\chi$:

$$\delta(M_{\rm max})^{29/4} \simeq 5\times 10^{-22}\,{\rm Br}_\chi^{-1}\left(\frac{g_{*\rm R}}{106.75}\right)^{1/4}\left(\frac{2\times 10^8\,{\rm g}}{M_{\rm max}}\right)^{1/2}\left(\frac{100\,{\rm GeV}}{m_\chi}\right). \quad (5.15)$$

We can trade out $\delta$ for the amplitude of the scalar power spectrum $A_{\rm s}\equiv 25\delta^2/4$ [146]. Planck 2015 has measured a value $A_{\rm s}=2.196\times 10^{-9}$ at the pivot scale of $k_*=0.05$ Mpc$^{-1}$ [147]. We translate the value of $\delta(M_{\rm max})$ from Eq. (5.15) to the enhancement factor in $A_{\rm s}$, denoted by $f_{\rm enh}=(\delta(M_{\rm max})/\delta_*)^2$, from $k_*$ to the scale relevant for forming PBHs with mass $M_{\rm max}$.

Figure 5.1 depicts the $\beta(M_{\rm max})$ curve from theory along with bands representing the observational constraint as a function of $f_{\rm enh}$ for $M_{\rm max}=2\times 10^8\,{\rm GeV}$. In the left panel, ${\rm Br}_\chi=1$ and the band corresponds to the mass range $m_\chi=100\,{\rm GeV}-10\,{\rm TeV}$. In the right panel, $m_\chi=1\,{\rm TeV}$ and the band corresponds to the range ${\rm Br}_\chi=10^{-2}-1$. The intersection region lies between $f_{\rm enh}\approx 6\times 10^4-2\times 10^5$ on the left, and $f_{\rm enh}\approx(1-4)\times 10^5$ on the right.

After using Eqs. (5.2), (5.5), and (5.13), we find the following expression for $H_{\rm R}$

$$H_{\rm R}\approx(200\,{\rm GeV})\,{\rm Br}_\chi^{-6/29}\left(\frac{g_{*\rm R}}{106.75}\right)^{3/58}\left(\frac{100\,{\rm GeV}}{m_\chi}\right)^{6/29}\left(\frac{2\times 10^8\,{\rm g}}{M_{\rm max}}\right)^{32/29}. \quad (5.16)$$

This results in $H_{\rm R}\approx(200-500)\,{\rm GeV}$ within the DM mass range $m_\chi=100\,{\rm GeV}-10\,{\rm TeV}$, for $M_{\rm max}=2\times 10^8\,{\rm g}$, with a very mild dependence on ${\rm Br}_\chi$. This corresponds to a very high reheat temperature of $T_{\rm R}\sim 10^{10}\,{\rm GeV}$, assuming that the Universe instantaneously thermalizes. Considering that fluctuations grow as $\delta\propto a\propto H^{-2/3}$ in the EMD epoch, formation of PBHs with mass $M_{\rm max}=2\times 10^8\,{\rm g}$ from perturbations whose initial amplitude is enhanced according to Figure 5.1 requires EMD to start no later than $H_0\approx 10^6\,{\rm GeV}$. This sets an absolute lower bound of $H_{\rm inf}\gtrsim 10^6\,{\rm GeV}$, which essentially excludes models of low scale inflation for this scenario.

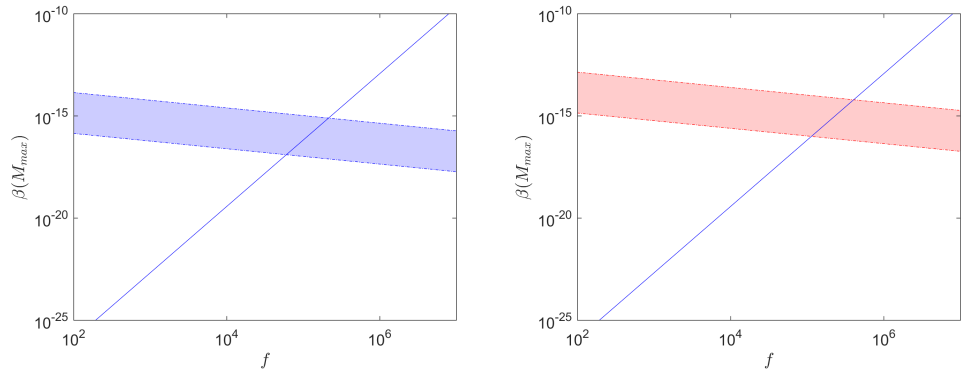


Figure 5.1: The solid line corresponds to the theoretical expression for $\beta(M_{\rm max})$ from Eq. (5.2) as a function of the enhancement factor $f_{\rm enh}$ in the scalar power spectrum at scales relevant for PBH formation. The shaded band shows the observational constraint on $\beta(M_{\rm max})$ from Eq. (5.14) for $\mathrm{Br}_\chi = 1$ in the mass range $m_\chi = 100\,\mathrm{GeV} - 1\,\mathrm{TeV}$ (left), and $m_\chi = 1\,\mathrm{TeV}$ with branching fraction between $\mathrm{Br}_\chi = 10^{-2} - 1$ (right). Larger values of $m_\chi$ or $\mathrm{Br}_\chi$ extend the band toward smaller values of $\beta$.

We see from Eq. (5.15) that a larger value of $\delta(M_{\rm max})$, and hence $f_{\rm enh}$, is needed when $M_{\rm max} < 2 \times 10^8\,\mathrm{g}$. Also, Eq. (5.16) implies a larger $H_{\rm R}$ in this case. Therefore, the scenario will be least constrained for $M_{\rm max} \simeq 2 \times 10^8\,\mathrm{g}$.

One question that arises is whether the large enhancement of the power spectrum that is needed at small scales $f_{\rm enh} \sim \mathcal{O}(10^5)$ is compatible with Planck limits on $n_{\rm s}$ and its running at the pivot scale $k_*$. Following [111], we can write

$$\ln A_{\rm s}(k) = \ln A_{\rm s}(k_*) + (n_{\rm s} - 1) \ln\left(\frac{k}{k_*}\right) + \frac{1}{2}\alpha_{\rm s} \ln^2\left(\frac{k}{k_*}\right) + \frac{1}{6}\beta_{\rm s} \ln^3\left(\frac{k}{k_*}\right) , \quad (5.17)$$

where $n_{\rm s} = 0.9655$ at $k_*$. Choosing $k = k_{\rm max}$, where $k_{\rm max}$ denotes the mode that eventually collapses to PBHs with mass $M_{\rm max}$, we have

$$\ln f_{\rm enh} = (n_{\rm s} - 1) \ln\left(\frac{k_{\rm max}}{k_*}\right) + \frac{1}{2}\alpha_{\rm s} \ln^2\left(\frac{k_{\rm max}}{k_*}\right) + \frac{1}{6}\beta_{\rm s} \ln^3\left(\frac{k_{\rm max}}{k_*}\right) . \quad (5.18)$$

The question is now whether the values of $f_{\rm enh}$ from Figure 5.1 are compatible with constraints from Planck data on the running parameters $\alpha_{\rm s}$ and $\beta_{\rm s}$ at the pivot scale. As shown in Appendix D,

$$\ln\left(\frac{k_{\rm max}}{k_*}\right) \approx 47.7 + \frac{1}{4} \ln \delta(M_{\rm max}) . \quad (5.19)$$

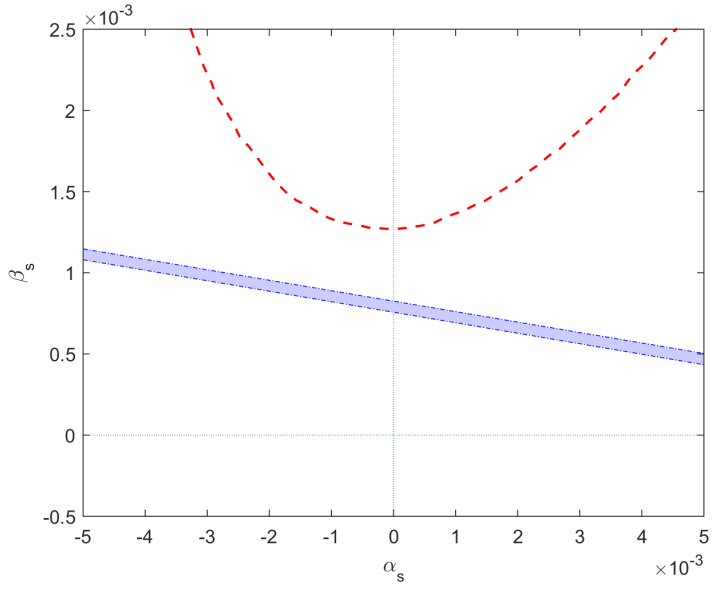


Figure 5.2: The shaded band in the $\alpha_{\rm s} - \beta_{\rm s}$ plane corresponds to the intersection region in the left panel of Figure 5.1. The 68% confidence ellipse from Planck 2015 [146] on the running of the scalar spectral index is outlined by the red dashed line.

Using this expression, and the relation $f_{\rm enh} = (\delta(M_{\rm max})/\delta_*)^2$, we can now check the consistency of Eq. (5.18) with Planck data. In Figure 5.2, we show a band in the $\alpha_{\rm s} - \beta_{\rm s}$ plane that corresponds to the intersection region in the left panel of Figure 5.1 through Eq. (5.19). This band is in agreement with Planck 2015 constraints on $\alpha_{\rm s}$ and $\beta_{\rm s}$ at the $2\sigma$ level.[6]

Another question that naturally arises concerns the mechanism behind a large enhancement of the power spectrum for modes around $k_{\rm max}$. In models of hybrid inflation, large density perturbations, which could lead to formation of PBHs, can be obtained toward the end of inflation [148]. This can also be achieved via multiple phases of inflation in single-field models [131], or by a brief period of ultra slow-roll motion toward the end of inflation [124, 130, 149, 150, 151, 152]. It has been shown in [150] that an amplification of the power spectrum up to a factor of $10^7$ within 10

[6]The band is also in agreement with the Planck 2018 68% limits of $\alpha_{\rm s} = 0.0011 \pm 0.0099$ and $\beta_{\rm s} = 0.009 \pm 0.012$ [9].

e-folds or so can be obtained from ultra slow-roll inflation near an inflection point. This fits well with the requirement in our scenario, namely an enhancement factor $f_{\rm enh} \sim \mathcal{O}(10^5)$ within a few e-folds that include the mode $k_{\rm max}$. While an explicit model to achieve this is beyond the scope of this dissertation, it is encouraging that the desirable enhancement in the power spectrum is both compatible with Planck limits and achievable in models of single-field inflation.

## 5.5 Discussion and conclusion

We now turn to a discussion of the possible origin and consequences of an EMD phase, formation of PBHs in the subsequent RD phase, and possible issues related to very light PBHs. Any implementation of our scenario within a specific model must be aware of these issues along with possible ways of addressing them.

**Origin and consequences of EMD** – An era of EMD can arise from oscillations of a very heavy modulus field that dominates the energy density of the Universe soon after the end of inflation. It may also start right at the end of inflation when the Universe is dominated by inflaton oscillations that eventually decay slowly via perturbative channels (for example, when the inflaton has gravitationally suppressed couplings to the visible sector fields). It may also be possible that the initial stages of inflaton decay occur via nonperturbative effects [153, 154, 155] (for reviews, see [16, 40]), and the zero-mode quanta of the inflaton (or other scalar fields produced during this process) come to dominate the Universe at some point.

One may also worry about dangerous consequences of the high reheat temperatures $T_{\rm R} \sim 10^{10}\,{\rm GeV}$ at the end of the EMD epoch. Notably, a concern arises regarding thermal overproduction of gravitinos that decay after BBN [156, 157, 158]. This can be avoided if the gravitino mass is $m_{3/2} \gtrsim 50\,{\rm TeV}$ so that gravitinos decay before the onset of BBN. Thermal gravitino production will be totally irrelevant if

$m_{3/2} \gg 10^{10}$GeV, which can happen in some string theory constructions (for example, see [159]). Gravitino production can also be suppressed if the Universe has the same equation of state as radiation but thermalization is delayed and full thermal equilibrium is not established when the EMD era ends [160].

**PBH formation in the RD phase** – The relation for $H_{\rm R}$ in Eq. (5.16) ensures that PBHs whose mass is larger than $M_{\rm max}$ are essentially not produced in the EMD epoch. However, an enhancement of the power spectrum for modes around $k_{\rm max}$ may result in the formation of heavier PBHs in the ensuing RD phase. This can happen from the collapse of the modes that enter the horizon when $H \lesssim H_{\rm R}$ (recall that in a RD Universe pressure dominates over gravity for subhorizon modes thus preventing their collapse). We do not expect formation of PBHs with exceedingly large masses in the RD phase as they would correspond to modes with $k \ll k_{\rm max}$, for which have $\delta(M) \ll \delta(M_{\rm max})$ due to the rapid fall off in the power spectrum far away from $k_{\rm max}$. In fact, because of the exponential dependence of $\beta(M)$ on $\delta(M)$ in the RD phase, even moderate suppression of the power spectrum at $k < k_{\rm max}$ can yield a substantial decrease in $\beta(M)$ in accordance with the most stringent observational limits. The abundance of PBHs that may form during RD follows from Eq. (5.1), with $\delta = \delta(M_{\rm max})$. For the values of $\delta(M_{\rm max})$ corresponding to the intersection regions in Figure 5.1, we find that $\beta(M) \ll 10^{-30}$ for $M \gtrsim 2 \times 10^8\,{\rm g}$. This easily satisfies even the tightest observational constraints on the abundance of PBHs over the entire mass range that evaporate after BBN [71].

**Effects of light PBHs** – Very light PBHs with mass $M \ll M_{\rm max}$ may form in the EMD phase. As mentioned above, and shown in Appendix D, the contribution of such black holes to the DM relic abundance is typically negligible. However, they can act as a site for bubble nucleation in a first order phase transition and seed vacuum decay. This effect can be relevant for the electroweak vacuum that becomes unstable for a certain range of the top quark mass [161]. It has been shown that PBHs with a mass in the range $(10^5 - 10^9)M_{\rm P}$ can seed decay of the Higgs vacuum as the decay

rate dominates over Hawking evaporation [162, 163].

The simplest possibility to avoid this effect, is to have an inflationary scale that corresponds to $H_{\rm inf} \lesssim 10^{-9} M_{\rm P}$. Since inflation generates density perturbations with physical wavenumbers $k < H_{\rm inf}$, the condition $H_{\rm inf} \lesssim 10^{-9} M_{\rm P}$ ensures the absence of fluctuation modes that could collapse to form dangerous PBHs with mass $M \lesssim 10^9 M_{\rm p}$. Another possibility is to have a situation where $\delta(M) \ll \delta(M_{\rm max})$ for $M \lesssim 10^9 M_{\rm P}$ as a result of the rapid fall off in the power spectrum far from the mode $k_{\rm max}$. Formation of dangerously light PBHs can then be prevented if the corresponding fluctuations do not grow to become $\mathcal{O}(1)$ by the time $H \simeq H_{\rm R}$, without any restrictions on $H_{\rm inf}$.

Any specific cosmological model producing light primordial black holes must be aware of the issues, along with possible ways of addressing them, that we have outlined above. Though specific models are left to future work, this sets the stage for exploring the intriguing prospect of light primordial black holes as a viable alternative to both the spectrum of primordial black hole masses that have traditionally been explored, and the WIMP paradigm in providing the DM abundance.

In conclusion, we have demonstrated that the evaporation of PBHs can produce the entire DM relic abundance within a DM mass range of $100\,\text{GeV} - 10\,\text{TeV}$, in cases with thermal underproduction. In order for this nonthermal scenario to be viable, a sufficient abundance of PBHs must be produced with masses below about $2 \times 10^8\,\text{g}$, so that they evaporate before BBN. We have found that an epoch of EMD can accommodate this if the scalar power spectrum is enhanced by a factor of $\mathcal{O}(10^5)$ at small scales relative to its value for the CMB modes. Such a scenario demonstrates the versatility of an EMD era as a phenomenological ingredient in the early Universe, particularly relating to DM production.

# Chapter 6

# Topological Dark Matter Involving Early Matter Domination

## 6.1 Introduction

In this penultimate chapter, we will explore the application of EMD eras to an exotic class of DM candidates known as topological DM.[1] Here we will assume DM to be composed of hidden sector magnetic monopoles, whereas in previous chapters, we have intentionally left the particle-physics identity of DM ambiguous (aside from it being a WIMP-like particle) in order to study model-independent effects of EMD eras. As the standard picture of thermal WIMP production is becoming increasingly strained, nonthermal production mechanisms, which depart from the assumptions of thermal equilibrium of DM with SM particles in the early Universe and/or radiation domination in this period, have become more widespread [5]. Spontaneous symmetry breaking in the early Universe prior to BBN provides a natural out-of-equilibrium process for the production of interesting objects. Specifically, symmetry breaking via

[1]The contents of this chapter are based on M. L. Graesser and J. K. Osiński, 2020, in preparation [164].

a second order phase transition can produce a large amount of topological defects through the Kibble-Zurek mechanism (KZM) [165, 166, 167], which can provide stable DM candidates.

Though in general the KZM can produce more complicated objects such as skyrmions, strings, and domain walls, for simplicity, we will be interested in the case where the defects are point-like magnetic monopoles, charged under an unbroken U(1) left over after the phase transition. The abundance of magnetic monopoles charged under the U(1) of electromagnetism is constrained by observations, such as the Parker limit, to be less than that required to account for the full DM abundance [168, 169]. We will therefore avoid such constraints in this chapter by considering the simplest scenario in which the monopoles are charged under a hidden U(1) that does not kinetically mix with electromagnetism, so that monopoles of the hidden sector do not couple to (visible sector) electromagnetic fields.

Topological DM is studied by [170] in the context of the standard thermal history, in which the phase transition that produces topological defects occurs during a RD era, and where the temperature of the symmetry breaking and visible sectors are assumed to be equal. We generalize the topological DM scenario to allow for an intervening phase of EMD in the thermal history of the early Universe, as well as the possibility that the hidden sector (HS) has a different temperature than the visible sector (VS) of SM particles. [2] As we assume that the two sectors interact only very weakly, if at all, there is no reason to expect them to have the same temperature. We will consider the era of EMD to be caused by either a modulus or a decoupled particle, and allow the phase transition to occur anywhere before, during, or after the EMD period.

[2]One can interpret such a cosmological scenario as actually consisting of two hidden sectors: a sector driving the EMD phase; and a second sector in which the symmetry breaking occurs. Couplings between these two sectors would be interesting to explore, and would lead to a more complicated cosmological history, but we will not do so here, simply to avoid over complicating the discussion.

Our scenario begins in a RD phase after inflation, where we allow for the dominant energy density component to be either HS or VS radiation. As the Universe expands, each sector cools independently of the other, and we enter an EMD phase caused by a modulus or by a heavy particle which has decoupled from either sector. As the EMD phase proceeds, the dominant component continually decays to radiation until this decay completes (reheating) and we transition back to a RD phase. We require the dominant component to decay primarily to the VS in order to preserve the standard cosmology at the onset of BBN. We consider a second-order phase transition in the HS as the HS temperature drops below some critical temperature $T_{\rm C}^{(\rm hid)}$, resulting in a significant production of magnetic monopoles in the HS due to the KZM. We allow the phase transition to occur at any time in the pre-BBN thermal history of our scenario. We also neglect any subsequent annihilations of monopoles, because of their high mass (PeV and above) and consequently low number density. As mentioned above, we do not consider any nongravitational interactions between the sectors, other than that which provides the decay that reheats the Universe.

We begin with a brief overview of monopole production in Section 6.2, followed by an overview of a nonthermal history involving EMD and a HS in Section 6.3. In Section 6.4, we present analytical forms for the monopole abundance in the presence of an EMD phase, including monopole production before, during, and after EMD. We then present numerical results for the cases of EMD by a modulus or a heavy decoupled particle in Sections 6.5 and 6.6 respectively. We conclude with a brief discussion in Section 6.7, and include some calculational details in Appendix E.

## 6.2 Monopole production involving early matter domination - part 1

We now briefly describe the KZM and refer the reader to the original references [165, 166, 167] for details. In the KZM theory, a system is assumed to be driven through a second-order phase transition by a quench that importantly, is assumed

to be of a finite timescale; it is neither instantaneous, nor extremely long. In a cosmological context, the quench is driven by the cosmological expansion of the Universe itself.

The KZM results in a monopole number density of approximately one per correlation volume, $\xi^{-3}$. As the temperature of the HS cools and passes through the critical temperature, $T_{\rm C}^{(\rm hid)}$, the behavior of the correlation length and the correlation time is characterized by the critical exponents $\nu$ and $\mu$ via $\xi = \xi_0|\epsilon|^{-\nu}$ and $\tau = \tau_0|\epsilon|^{-\mu}$ respectively, where the temperature parameter is $\epsilon \equiv (T_{\rm C}^{(\rm hid)} - T^{(\rm hid)})/T_{\rm C}^{(\rm hid)}$. Because we enforce the requirement of reheating predominantly to the VS before BBN, the HS temperature only redshifts with time, and therefore, to linear order, we have $\epsilon \approx (t - t_{\rm C})/2t_{\rm C}$ if the phase transition occurs in a RD period, and $\epsilon \approx 2(t - t_{\rm C})/3t_{\rm C}$ in EMD. This results in a quenching time of $\tau_{\rm Q} = 2t_{\rm C}$ in RD and $\tau_{\rm Q} = 3t_{\rm C}/2$ in EMD, which in both cases can be re-expressed in terms of the Hubble rate at the critical time as $H_{\rm C}^{-1}$.

For a finite speed quench, the time which marks the freezing of fluctuations is $\tau(t_*) = |t_* - t_{\rm C}|$ [165, 170], which results in a frozen correlation length of

$$\xi(t_*) \approx \xi_0 \left(\frac{\tau_{\rm Q}}{\tau_0}\right)^{\frac{\nu}{1+\mu}} \tag{6.1}$$

For a Landau-Ginsberg potential, $V(\phi) = (T^{(\rm hid)} - T_{\rm C}^{(\rm hid)})m\phi^2 + (1/2)\lambda\phi^4$, the critical exponents are both 1/2, and we take $\xi_0 \approx \tau_0 \sim (T_{\rm C}^{(\rm hid)}\sqrt{\lambda})^{-1}$ for the initial correlation length [167, 170]. However, we will keep the critical exponents general to allow for quantum corrections, but will restrict them to the range $0 \leq \nu \leq \mu \leq 1$. In terms of cosmological quantities, the frozen correlation length is then

$$\xi(t_*) \approx \frac{1}{T_{\rm C}^{(\rm hid)}\sqrt{\lambda}} \left(\frac{T_{\rm C}^{(\rm hid)}\sqrt{\lambda}}{H_{\rm C}}\right)^{\frac{\nu}{1+\mu}} \tag{6.2}$$

regardless of the type of dominant energy density, with the understanding that the temperature dependence of $H_{\rm C}$ does depend on the form of the dominant energy density component. We further note that $g_*^{(\rm hid)}$, the number of relativistic degrees of

freedom in the HS, is taken to be constant for times near the critical time. After the phase transition is complete, the monopole number density is $n_{\rm M} \approx \xi(t_*)^{-3}$ and the comoving number density is fixed as their abundance simply redshifts through the remaining history of the Universe. We will neglect any subsequent annihilations of monopoles because the masses needed to account for the entire current DM abundance will turn out to be quite high, with correspondingly low number densities, and we additionally do not wish to specify any details of the HS. [3]

## 6.3 A thermal history interlude

In order to proceed, we must address the relationship between the Hubble expansion rate and the temperature of the Universe. In this section, we therefore introduce the general expansion history we will be considering. First, we begin with RD by either the hidden or visible sector (or any combination) some time after inflation, with other energy densities comparatively negligible. In this era, the Hubble expansion rate is given by

$$H = \sqrt{\frac{\left(\rho_{\rm r}^{(\rm vis)} + \rho_{\rm r}^{(\rm hid)}\right)}{3M_{\rm P}^2}} = \sqrt{\frac{\pi^2}{90} g_*^{(\rm hid)} (1+f)} \frac{{T^{(\rm hid)}}^2}{M_{\rm P}} \tag{6.3}$$

where the factor $f \equiv \rho_{\rm r}^{(\rm vis)}/\rho_{\rm r}^{(\rm hid)}$ defines the ratio of the radiation energy densities of the visible and hidden sectors, $T^{(\rm hid)}$ is the temperature of the HS, $g_*^{(\rm hid)}$ is the number of relativistic degrees of freedom in the HS at temperature $T^{(\rm hid)}$, and $M_{\rm P} \approx 2.4 \times 10^{18}\,\text{GeV}$ is the reduced Planck mass. In this period, the factor $(1+f)$ is well approximated by its initial value $(1+f_{\rm i})$ regardless of the distribution of initial radiation among the two sectors, and we will make this substitution when using Eq. (6.3) below. We consider the visible and hidden sectors to have independent temperatures, each with their own $g_*$ factors depending on the specific particle content

[3] The interactions of magnetic monopoles with fermions have not been fully worked out because this is a strongly coupled system, and therefore the rate of dissipation of monopole energy in a HS plasma is unknown [171, 172, 173, 174].

(standard model for the VS), and we could have equivalently expressed Eq. (6.3) in terms of VS quantities. The $g_*$ factors of course depend on the temperature of their respective sector, but we will treat $g_*^{(\mathrm{hid})}$ as roughly constant at high temperatures in order to avoid specifying the details of the HS.

We achieve EMD through the presence of a scalar modulus, or by the decoupling of a heavy scalar field from either the HS or VS during this initial RD phase. We call this scalar $\Phi$ in both cases. If $\Phi$ has gravitational coupling, it decays with a rate

$$\Gamma_\Phi \sim \frac{\alpha^2}{2\pi}\frac{m_\Phi^3}{M_\mathrm{P}^2} \tag{6.4}$$

where $m_\Phi$ is the $\Phi$ mass, and we have included a possible loop factor $\alpha^2$ in the case that $\Phi$ decay occurs predominantly through a loop (we will set $\alpha = 1$ when not considering this). The decay is complete when $H \approx H_\mathrm{RH} \equiv \Gamma_\Phi$, which marks the approximate time of reheating, and we avoid having significant amounts of left over hidden radiation by requiring $\Phi$ to decay predominantly to the VS:

$$H_\mathrm{R} = \sqrt{\frac{\pi^2}{90} g_{*\mathrm{R}}^{(\mathrm{vis})} \left(1 + \frac{1}{f_\mathrm{R}}\right)} \frac{{T_\mathrm{R}^{(\mathrm{vis})}}^2}{M_\mathrm{P}} \tag{6.5}$$

where $T_\mathrm{R}^{(\mathrm{vis})}$ is the VS temperature at reheating, and $g_{*\mathrm{R}}^{(\mathrm{vis})}$ is the number of relativistic degrees of freedom in the VS at this temperature. In order to preserve standard BBN, the VS reheat temperature must be larger than a few MeV. The ratio of the VS radiation energy density to that of the HS at reheating, denoted by $f_\mathrm{R}$, depends on the duration of the EMD phase as well as the initial factor $f_\mathrm{i}$, but is typically large due to our VS reheating requirement, and thus always satisfies $f_\mathrm{R} > 1$ and $f_\mathrm{R} > f_\mathrm{i}$ (see Appendix E). This ensures that the temperature of the HS at reheating, $T_\mathrm{R}^{(\mathrm{hid})}$, is correspondingly always smaller than that of the VS. We also point out that this ratio remains fixed after reheating due to the absence of any further decays. From Eqs. (6.4) and (6.5), we additionally see that a given choice of the VS reheat temperature specifies a corresponding $\Phi$ mass in the absence of loop decay, while including the loop factor allows for different combinations.

In order to have a well defined EMD phase, the energy density of $\Phi$ must be large enough to dominate well before reheating. During EMD, the scaling of the Hubble rate with the VS temperature is altered from a typical MD redshift relation because the VS is fed by the decay of $\Phi$; however, the scaling with the HS temperature remains unaffected: $H^{2/3} \propto T^{(\mathrm{hid})} {g_*^{(\mathrm{hid})}}^{1/4}$. Based on the initial energy density of VS radiation, there can be a phase of ordinary redshift for the VS temperature even during EMD (see Chapter 4), but once the effect of the decay wins over this dilution (see, for example, Eq. (6.19)), the relation becomes:

$$H = \left( \frac{5\pi g_*^{(\mathrm{vis})}}{6\sqrt{10} {g_{*\mathrm{R}}^{(\mathrm{vis})}}^{1/2}} \right) \frac{{T^{(\mathrm{vis})}}^4}{{T_{\mathrm{R}}^{(\mathrm{vis})}}^2 M_{\mathrm{P}}} \tag{6.6}$$

This relation is always true just before reheating, but may not start until deep within the EMD phase if the initial VS radiation energy density is large.

At the end of the EMD phase, once reheating completes, we enter RD with the Hubble rate given by

$$H = \sqrt{\frac{\pi^2}{90} g_*^{(\mathrm{vis})} \left( 1 + \frac{1}{f_{\mathrm{RH}}} \right)} \frac{{T^{(\mathrm{vis})}}^2}{M_{\mathrm{P}}} \tag{6.7}$$

where the factor $f_{\mathrm{R}}$ is large such that the VS is dominant, thus recovering the standard thermal history leading up to BBN.

## 6.4 Monopole production involving early matter domination - part 2

We can now address monopole production in the context of the thermal history presented in the previous section. The effects of EMD on the monopole abundance can be understood regardless of the mechanism for establishing MD in this early period, and we obtain analytical expressions below that do not depend on the identity of the field $\Phi$. In addition to the start time of EMD, what matters is that the

dominant energy density component decays to VS radiation at a rate $\Gamma_\Phi$, thus setting the end time of EMD. The overall effect is to slow the redshift of VS radiation relative to the HS such that only the VS is dominant after EMD even if it was not initially. Because we only consider HS magnetic monopoles, this offset in the VS and HS temperatures generally results in a lower number density of monopoles of a given mass, where the magnitude of the offset is determined by the duration of EMD and the initial abundances of visible and hidden radiation. We label the start of EMD by $H = H_{\rm MD}$, with VS and HS temperatures $T_{\rm MD}^{\rm (vis)}$ and $T_{\rm MD}^{\rm (hid)}$ respectively, and the end of the EMD phase occurs when $H \approx \Gamma_\Phi$. Recall that the VS reheat temperature, which we restrict to be larger than a few MeV such that reheating occurs before BBN, is the primary parameter that determines the end of EMD.

**Production before EMD** – We will start with the case where the HS phase transition occurs in the RD period before EMD, resulting in a frozen monopole number density that is redshifted through the remainder of the RD phase as well as the full EMD period. This results in considerable dilution and a need for higher monopole masses in order to maintain a fixed contribution to the energy density of the Universe. Using Eq. (6.2) and recalling that the number density of monopoles produced in the phase transition is approximately one per correlation volume, we have

$$\left(\frac{n_{\rm M}}{s_{\rm (vis)}}\right)_{\rm R}^{\rm (before)} \approx \frac{45(T_{\rm C}^{\rm (hid)}\sqrt{\lambda})^{3-\frac{3\nu}{1+\mu}} H_{\rm C}^{\frac{3\nu}{1+\mu}}}{2\pi^2 h_{*\rm R}^{\rm (vis)} {T_{\rm R}^{\rm (vis)}}^3} \left(\frac{\Gamma_\Phi^2}{H_{\rm C}^{3/2} H_{\rm MD}^{1/2}}\right) \tag{6.8}$$

where the factor in parentheses on the rhs accounts for redshift from the critical time to the start of EMD, and then from the start of EMD to reheating. We do not need to redshift any further and can obtain a fixed abundance by normalizing by the VS entropy density at reheating, as both number density and entropy density dilute as the cube of the scale factor once the significant entropy production from reheating stops. The factor $h_*^{\rm (vis)}$ tracks the VS relativistic degrees of freedom for entropy and is nearly equal to $g_*^{\rm (vis)}$ for the high temperatures in our scenario as well as the low temperature today [11, 43] (it is evaluated at reheating in the expression above, as

indicated by the subscript). Note that the Hubble rate at the critical time is given by Eq. (6.3).

**Production during EMD** – If the phase transition occurs during the EMD phase, the frozen monopole number density only redshifts through the remaining duration of EMD, and we have

$$\left(\frac{n_{\rm M}}{s_{\rm (vis)}}\right)_{\rm R}^{\rm (during)} = \frac{45(T_{\rm C}^{\rm (hid)}\sqrt{\lambda})^{3-\frac{3\nu}{1+\mu}} H_{\rm C}^{\frac{3\nu}{1+\mu}}}{2\pi^2 h_{*\rm R}^{\rm (vis)} {T_{\rm R}^{\rm (vis)}}^3} \left(\frac{\Gamma_\Phi}{H_{\rm C}}\right)^2 \tag{6.9}$$

As before, we normalize by the VS entropy density at reheating to obtain the frozen monopole abundance. The dependence of $H_{\rm C}$ on the HS temperature is that of ordinary MD redshift, while the relation to the VS temperature depends on how much VS radiation was present at the onset of EMD. If the VS energy density is greater than the contribution from the decay of $\Phi$ at $H = H_{\rm MD}$, then there will be a period of ordinary MD redshift for the VS temperature as well. Once the decay contribution takes over well within the EMD phase, we have the relation of Eq. (6.6). We note that this modified scaling can begin much earlier, even before EMD, if the initial VS radiation energy density is small.

**Production after EMD** – Finally, if the phase transition occurs in the RD period after reheating but still before BBN, so as to leave the later evolution of the Universe unchanged, the abundance can be evaluated directly at the critical time, without need of redshifting:

$$\left(\frac{n_{\rm M}}{s_{\rm (vis)}}\right)_{\rm C}^{\rm (after)} = \frac{45(T_{\rm C}^{\rm (hid)}\sqrt{\lambda})^{3-\frac{3\nu}{1+\mu}} H_{\rm C}^{\frac{3\nu}{1+\mu}}}{2\pi^2 h_{*\rm C}^{\rm (vis)} {T_{\rm C}^{\rm (vis)}}^3} \tag{6.10}$$

This expression is also valid for a thermal history that does not involve EMD at all, where the HS radiation energy density is lower than or equal to that of the VS by a constant factor, as both energy densities simply redshift with time. The Hubble rate at the critical time is given by Eq. (6.7) in terms of VS quantities, but is easily related to the corresponding HS quantities by multiplying by the square root of the constant factor.

In these three cases of monopole production before, during, or after EMD, the parameters $\mu$, $\nu$, and $\lambda$, are determined by the details of the phase transition, as is the ratio $x_{\rm M} \equiv m_{\rm M}/T_{\rm C}^{\rm (hid)}$. This ratio typically has a value of $\mathcal{O}(10)$ [170], and we will assume $x_{\rm M} = 50$ in our results below. The current abundance of monopoles, expressed as a fractional energy density $\Omega_{\rm M}h^2$, is related to the frozen abundance by

$$\Omega_{\rm M}h^2 = \Omega_\gamma h^2 \frac{2h_{*0}^{\rm (vis)} m_{\rm M}}{3T_0^{\rm (vis)}} \left(\frac{n_{\rm M}}{s_{\rm (vis)}}\right)_0 \approx \Omega_\gamma h^2 \frac{2h_{*0}^{\rm (vis)} m_{\rm M}}{3T_0^{\rm (vis)}} \left(\frac{n_{\rm M}}{s_{\rm (vis)}}\right)_{\rm R,C}^{\rm (EMD)} \tag{6.11}$$

where $\Omega_\gamma h^2 = 2.473 \times 10^{-5}$ is the current photon abundance, and we have made use of the relation $\rho_\gamma = (2/g_*^{\rm (vis)})\rho_{\rm r}^{\rm (vis)}$ between the photon and VS radiation energy densities [175]. The subscript '0' labels the current time, and the final term labeled by the superscript '(EMD)' refers to any one of the three above cases. In order for monopoles to constitute all of DM, the value of $\Omega_{\rm M}h^2$ must reach the observed value of 0.12 [9].

We can obtain a few more analytical expressions to understand the effect of EMD in more detail. The three cases of monopole production above are separated by production at the start and end of EMD, and we can easily obtain expressions for the monopole abundance corresponding to these boundaries.

**Production at the start of EMD** – For production at the start of EMD, the HS temperature at the critical point is $T_{\rm C}^{\rm (hid)} = T_{\rm MD}^{\rm (hid)}$ with corresponding $H_{\rm C} = H_{\rm MD}$. From Eqs. (6.3) and (6.9), we obtain the frozen abundance of monopoles at reheating:

$$\left(\frac{n_{\rm M}}{s_{\rm (vis)}}\right)_{\rm R}^{\rm (start)} = \frac{45\lambda^{\frac{3}{2}-\frac{3\nu}{2(1+\mu)}} \left(\frac{\pi^2}{90} g_{*\rm MD}^{\rm (hid)}(1+f_{\rm i})\right)^{\frac{3\nu}{2(1+\mu)}-1} {T_{\rm C}^{\rm (hid)}}^{\frac{3\nu}{1+\mu}-1} \Gamma_\Phi^2}{2\pi^2 h_{*\rm R}^{\rm (vis)} {T_{\rm R}^{\rm (vis)}}^3 M_{\rm P}^{\frac{3\nu}{1+\mu}-2}} \tag{6.12}$$

Aside from the parameters of the phase transition, the abundance is determined by the VS reheat temperature, the initial ratio of VS-to-HS radiation, and the monopole mass.

**Production at the end of EMD** – Monopole production at the end of EMD corresponds to a HS critical temperature of $T_{\rm C}^{\rm (hid)} = T_{\rm R}^{\rm (hid)}$ with $H_{\rm C} = H_{\rm R} = \Gamma_\Phi$.

This results in a frozen monopole abundance of:

$$\left(\frac{n_{\rm M}}{s_{\rm (vis)}}\right)_{\rm R}^{\rm (end)} = \frac{45\left(T_{\rm C}^{\rm (hid)}\sqrt{\lambda}\right)^{3-\frac{3\nu}{1+\mu}}\Gamma_{\Phi}^{\frac{3\nu}{1+\mu}}}{2\pi^2 h_{*\rm R}^{\rm (vis)} {T_{\rm R}^{\rm (vis)}}^3} \tag{6.13}$$

Note that this expression does not depend on the initial ratio of radiation energy densities as it only involves the time of reheating.

Requiring EMD to start before reheating, these two expressions for production at the boundaries of EMD significantly constrain the allowed parameter space. For a realistic scenario, even the shortest EMD period will have a finite duration such that EMD is well defined, ensuring that we never quite access the limiting case where the start and end of EMD are coincident. This case, rather, corresponds to the absence of EMD altogether.

It is also useful to obtain the functional dependence of the monopole abundance produced during any of the three periods of Eqs. (6.8)-(6.10) on the monopole mass. To do this, we need to extract the dependence of the Hubble rate $H_{\rm C}$ on the HS critical temperature. In the period before EMD, we have the RD relation of Eq. (6.3), while in the period after EMD we have this same functional form, but with a different constant factor offsetting the VS and HS radiation energy densities. During EMD, because the HS is not being fed by the decay of $\Phi$, we have the standard MD relation: ${g_*^{\rm (hid)}}^{1/4} T^{\rm (hid)} \propto H^{2/3}$. Additionally, for production after EMD, the VS critical temperature is related to the HS critical temperature by a constant factor. With these relations, and Eq. (6.11), we have

$$\Omega_{\rm M} h^2 \propto \begin{cases} m_{\rm M}^{1+\frac{3\nu}{1+\mu}} & \text{(RD)} \\ m_{\rm M}^{1+\frac{3\nu}{2(1+\mu)}} & \text{(EMD)} \end{cases} \tag{6.14}$$

where the RD case applies to monopole production both before and after EMD, and we have again assumed a constant factor, $x_{\rm M}$, between the monopole mass and HS critical temperature. We will provide the detailed expressions for the frozen monopole abundance in the following sections, which address the nature of $\Phi$.

Before moving on to consider specific scenarios for establishing EMD, we can see that the presence of an intervening MD phase in the period before BBN pushes the preferred monopole mass for DM higher than in a purely RD equivalent. Fixing the phase transition parameters ($\mu$, $\nu$, $\lambda$, and $x_{\rm M}$) as well as the monopole mass, $m_{\rm M}$, we must first identify the equivalent RD scenario, which comes down to specifying the factor $f^{(\rm RD)}$ between the VS and HS radiation energy densities. We obtain this by decreasing the duration of EMD until we arrive at the limiting RD scenario to use for comparison. If EMD is preceded by a period of RD by the VS, the limiting scenario is one which preserves the initial ratio of VS-to-HS radiation: $f^{(\rm RD)} = f_{\rm i}$. However, if HS radiation is dominant before EMD, the limiting case is one of $f^{(\rm RD)} = 1$ because we wish to avoid RD by the HS at the onset of BBN. With this, we can easily see that $f_{\rm R}$ is always larger than $f^{(\rm RD)}$ by a factor $e_{\rm f} = \left(\rho_{\rm r}^{(\rm hid)}\right)_{\rm R}^{(\rm RD)} / \left(\rho_{\rm r}^{(\rm hid)}\right)_{\rm R}^{(\rm EMD)}$, so long as $\Phi$ preferentially decays to the VS. The factor $e_{\rm f}$ is fixed for a given EMD phase, regardless of the value of $f_{\rm i}$ or the timing of the phase transition (see Appendix E). Using Eqs. (6.8)-(6.10), we arrive at the ratio of the current monopole abundance between an EMD and a pure RD scenario:

$$\frac{\Omega_{\rm M}^{(\rm EMD)}}{\Omega_{\rm M}^{(\rm RD)}} = \frac{1}{e_{\rm f}^{3/4}} \begin{cases} \left(\frac{1+f_{\rm MD}}{1+f^{(\rm RD)}}\right)^{\frac{3\nu}{2(1+\mu)}} & \text{(before)} \\ \left(\frac{1+f_{\rm C}}{1+f^{(\rm RD)}}\right)^{\frac{3\nu}{2(1+\mu)}} & \text{(during)} \\ \left(\frac{1+f_{\rm C}}{1+f^{(\rm RD)}}\right)^{\frac{3\nu}{2(1+\mu)}} \frac{\left(h_{*\rm C}^{(\rm vis)}\right)^{(\rm RD)}}{\left(h_{*\rm C}^{(\rm vis)}\right)^{(\rm EMD)}} \left(\frac{\left(g_{*\rm C}^{(\rm vis)}\right)^{(\rm EMD)}}{\left(g_{*\rm C}^{(\rm vis)}\right)^{(\rm RD)}}\right)^{3/4} & \text{(after)} \end{cases} \tag{6.15}$$

where the cases refer to monopole production before, during, or after the EMD phase. In all three cases, the terms involving $f$'s and the critical exponents are the ratios of the monopole number densities produced at the critical time between the EMD and RD scenarios. In the first two cases, we normalize the monopole number densities by the VS entropy density at the time of reheating (when the VS temperature is equal to the reheat temperature), accounting for the redshift factors, while in the third case, because monopole production occurs in RD after EMD, there is no need

for redshifting, and we normalize by the VS entropy densities at the critical time. The factor of $1/e_{\rm f}^{3/4}$, in the first two cases, is the ratio of the redshift factors from the time of monopole production to reheating between the EMD and RD scenarios respectively, while in the third case, it, along with the terms involving the relativistic degrees of freedom, comes from the ratio of entropy densities at the critical time between the two scenarios.

In each case, the rhs of Eq. (6.15) is less than one, which can be verified by considering the relative sizes of the numerical factors involved. The exponent of the $f$-dependent terms ranges from 0 to 3/4 for the range $0 \leq \nu \leq \mu \leq 1$. In the first case, of monopole production before EMD, we have $f_{\rm MD} \leq f^{(\rm RD)}$ and the number density of monopoles just after their production is thus smaller than, or at most equal to, the number density in a RD equivalent scenario. Furthermore, the factor $e_{\rm f} > 1$, and the number density experiences more redshift due to the EMD phase than the RD equivalent number density, resulting in a smaller frozen abundance. In the second case, of monopole production during EMD, there is no fixed relation between $f_{\rm C}$ and $f^{(\rm RD)}$, so the produced number density can be smaller than, equal to, or greater than that of the RD equivalent, however, the increased amount of redshifting is always sufficient to bring the frozen abundance below the RD equivalent. In the third case, of monopole production after EMD, the visible and hidden sectors are offset by a larger value than those in the RD scenario, with $f_{\rm C} > f^{(\rm RD)}$, resulting in a larger produced number density for the EMD scenario, however, this greater offset also results in a larger entropy density such that the frozen abundance is again smaller than that of the RD scenario after normalization. The frozen monopole abundance in a scenario involving EMD is therefore always less than or equal to that in a pure RD equivalent, for a fixed monopole mass. This, along with the mass-dependence of Eq. (6.14), results in a larger monopole mass needed to account for a fixed $\Omega_{\rm M}h^2$ when EMD is involved.

## 6.5 Early matter domination by a modulus

We now move to consider specific mechanisms for establishing a period of EMD, beginning with the case where the matter-dominating field $\Phi$ is a scalar modulus with mass $m_\Phi$ and initial amplitude $\Phi_{\rm i} \lesssim M_{\rm P}$ [18]. The modulus begins to oscillate, acquiring a matter equation of state, when $H \approx m_\Phi$, at which time its energy density is given by $\rho_{\Phi,{\rm i}} = (1/2)m_\Phi^2\Phi_{\rm i}^2$. This initial energy density, along with the matter-like redshift relation $\rho_\Phi \sim a^{-3}$, determines how quickly $\Phi$ can dominate over the background radiation energy density, be it of the hidden or visible sectors. The initial ratio of the VS radiation energy density to that of the hidden sector is given by the factor $f_{\rm i}$. The Hubble factor during the period before EMD by $\Phi$ is given by Eq. (6.3).

EMD begins shortly after the energy densities of $\Phi$ and radiation become comparable, and approximately corresponds to

$$H_{\rm MD} \approx \frac{m_\Phi \Phi_{\rm i}^4}{36 M_{\rm P}^4}\,. \tag{6.16}$$

In calculating this, we have assumed the energy density of $\Phi$ is dominant over, as opposed to equal to, that of radiation, which results in a better agreement between our analytical calculations and numerical results shown below. For a modulus with maximal amplitude, we note that the modulus essentially dominates the energy density of the Universe as it begins to oscillate, while a smaller amplitude results in a delay. In order to successfully establish EMD, $\Phi$ must also be sufficiently long lived such that its decay completes well after the start of EMD. The minimum value of the initial amplitude, corresponding to decay at the onset of EMD, can be estimated from Eqs. (6.4) and (6.16) to be

$$\Phi_{\rm i} \gtrsim \left(\frac{36\Gamma_\Phi M_{\rm P}^4}{m_\Phi}\right)^{1/4} \approx \sqrt{\alpha m_\Phi M_{\rm P}} \tag{6.17}$$

For tree-level decays, a given VS reheat temperature determines not only the end of EMD, but also the mass of $\Phi$ and thus the minimum amplitude to have EMD at

all. A choice of $\Phi_{\rm i}$, within the allowed limits, then determines how early the EMD phase starts. The inclusion of a loop factor in $\Gamma_\Phi$ shifts the values of $m_\Phi$ and $\Phi_{\rm i}$ which correspond to a particular EMD duration for a given VS reheat temperature. A change in initial amplitude of $10^{-1}$ can be compensated by a change in mass of $10^4$ with a loop factor of $10^{-12}$, resulting in the same EMD phase.

The evolution of the three background energy density components (that of $\Phi$ and the radiation from the hidden and visible sectors) is governed by the following set of Boltzmann equations:

$$\frac{d\rho_\Phi}{dt} + 3H\rho_\Phi = -\Gamma_\Phi \rho_\Phi \tag{6.18}$$

$$\frac{d\rho_{\rm r}^{\rm (vis)}}{dt} + 4H\rho_{\rm r}^{\rm (vis)} = \Gamma_\Phi \rho_\Phi \tag{6.19}$$

$$\frac{d\rho_{\rm r}^{\rm (hid)}}{dt} + 4H\rho_{\rm r}^{\rm (hid)} = 0 \tag{6.20}$$

where $3H^2M_{\rm P}^2 = \rho_\Phi + \rho_{\rm r}^{\rm (vis)} + \rho_{\rm r}^{\rm (hid)}$, and the equation for $\Phi$ is only valid after $H = m_\Phi$. We emphasize that, for simplicity, we have taken $\Phi$ to decay only to the VS in the Boltzmann equations above, though it is straightforward to include branching fractions for decay to both sectors. We numerically solve this set of equations beginning in a period of RD by any combination of VS and HS radiation, and track the evolution sufficiently beyond reheating such that RD by the VS is well established. Additionally, we use a smooth function (shown in Appendix A) to capture the temperature dependence of the relativistic degrees of freedom in the VS, $g_*^{\rm (vis)}$, while for the HS we assume a constant $g_*^{\rm (hid)} = 100$. Figure 6.1 shows the energy density evolution in the two cases of initial RD by the HS ($f_{\rm i} << 1$) and VS ($f_{\rm i} >> 1$) respectively, for an example set of parameters.

We allow the phase transition of the HS to occur at any time in the background evolution, and obtain the resultant current monopole abundance from the numerical solution. Analytical expressions can be obtained in the three periods of our scenario by noting that

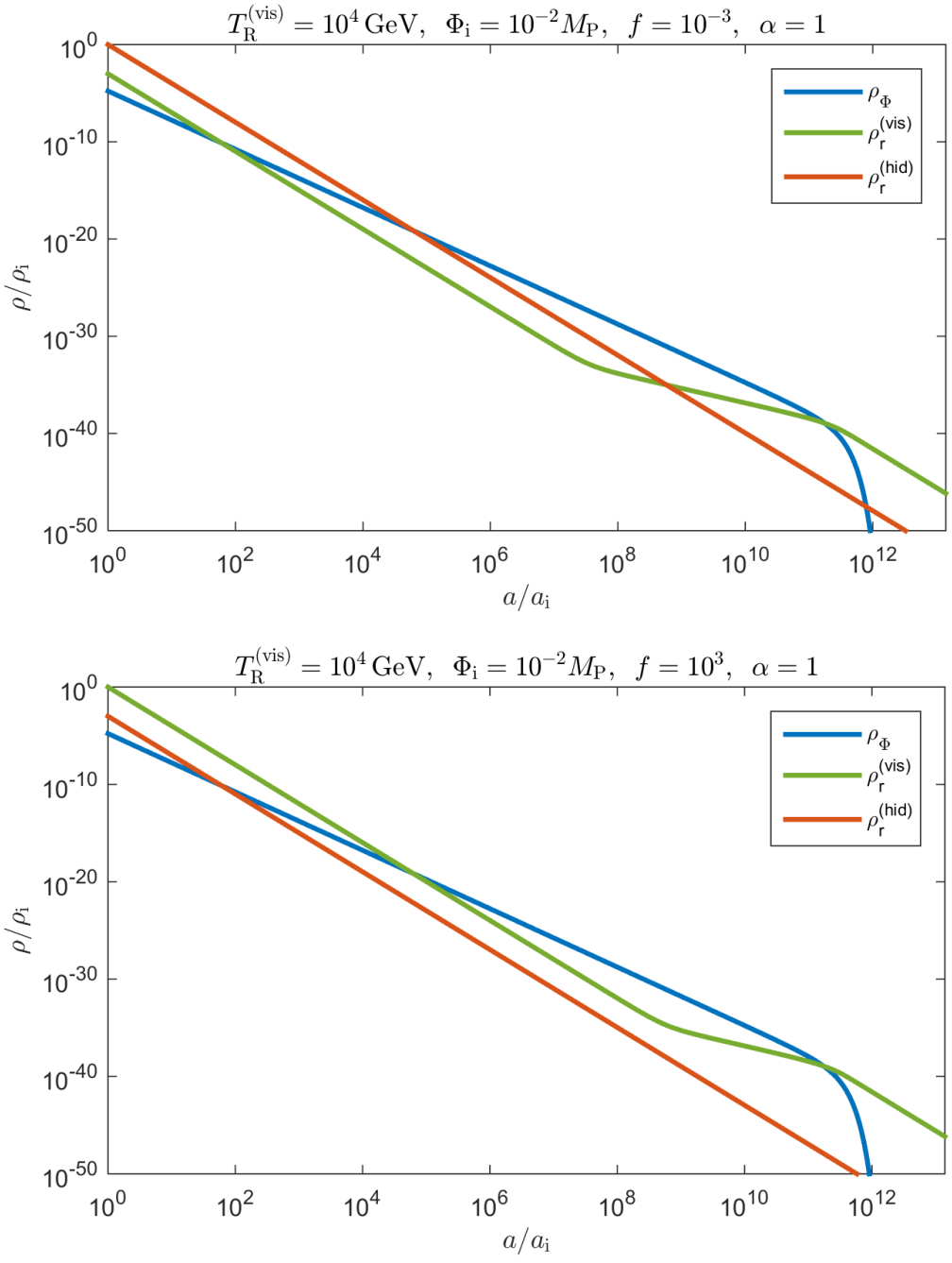


Figure 6.1: Numerical evolution of the background energy density components with scale factor. EMD begins once $\rho_\Phi$ dominates over both radiation components, and lasts until $\Phi$ decays. Top panel: initial RD by the HS. Bottom panel: initial RD by the VS.

$$H_{\rm C} \approx \begin{cases} \sqrt{\frac{\pi^2}{90} g_*^{(\rm hid)} (1+f_{\rm i})} \frac{{T_{\rm C}^{(\rm hid)}}^2}{M_{\rm P}} & \text{(before)} \\ \left( \frac{\pi^2}{90} g_*^{(\rm hid)} (1+f_{\rm i}) \right)^{3/8} \frac{H_{\rm MD}^{1/4} {T_{\rm C}^{(\rm hid)}}^{3/2}}{M_{\rm P}^{3/4}} & \text{(during)} \\ \sqrt{\frac{\pi^2}{90} g_*^{(\rm hid)} (1+f_{\rm R})} \frac{{T_{\rm C}^{(\rm hid)}}^2}{M_{\rm P}} & \text{(after)} \end{cases} \tag{6.21}$$

Using Eqs. (6.8), (6.9), (6.10), and (6.11), the analytical estimates for the monopole abundance produced during modulus-driven EMD are

$$\frac{(\Omega_{\rm M} h^2)^{(\rm before)}}{\Omega_\gamma h^2} \approx \left( \frac{15 \lambda^{3/4} h_{*0}^{(\rm vis)} \Gamma_\Phi^2 m_{\rm M}^{5/2}}{\pi^2 x_{\rm M}^{3/2} h_{*\rm R}^{(\rm vis)} {T_{\rm R}^{(\rm vis)}}^3 T_0^{(\rm vis)} H_{\rm MD}^{1/2}} \right) \left( \frac{\pi^2 g_*^{(\rm hid)} (1+f_{\rm i}) m_{\rm M}^2}{90 \lambda x_{\rm M}^2 M_{\rm P}^2} \right)^{\frac{3\nu}{2(1+\mu)} - \frac{3}{4}} \tag{6.22}$$

$$\frac{(\Omega_{\rm M} h^2)^{(\rm during)}}{\Omega_\gamma h^2} \approx \left( \frac{15 \lambda^{1/2} h_{*0}^{(\rm vis)} \Gamma_\Phi^2 m_{\rm M}^2}{\pi^2 x_{\rm M} h_{*\rm R}^{(\rm vis)} {T_{\rm R}^{(\rm vis)}}^3 T_0^{(\rm vis)}} \right) \left( \frac{\pi^2 g_*^{(\rm hid)} (1+f_{\rm i}) H_{\rm MD}^{2/3} m_{\rm M}^{4/3}}{90 \lambda^{4/3} x_{\rm M}^{4/3} M_{\rm P}^2} \right)^{\frac{9\nu}{8(1+\mu)} - \frac{3}{4}} \tag{6.23}$$

$$\frac{(\Omega_{\rm M} h^2)^{(\rm after)}}{\Omega_\gamma h^2} \approx \left( \frac{15 \lambda^{3/4} h_{*0}^{(\rm vis)} \Gamma_\Phi^{3/2} m_{\rm M}^{5/2}}{\pi^2 x_{\rm M}^{3/2} h_{*\rm R}^{(\rm vis)} {T_{\rm R}^{(\rm vis)}}^3 T_0^{(\rm vis)}} \right) \left( \frac{\pi^2 g_*^{(\rm hid)} (1+f_{\rm R}) m_{\rm M}^2}{90 \lambda x_{\rm M}^2 M_{\rm P}^2} \right)^{\frac{3\nu}{2(1+\mu)} - \frac{3}{4}} \tag{6.24}$$

In Figure 6.2 we plot the current monopole abundance, $\Omega_{\rm M} h^2$, as a function of monopole mass, $m_{\rm M}$, for a variety of parameter values, where we have taken $x_{\rm M} \equiv m_{\rm M}/T_{\rm C}^{(\rm hid)} = 50$. The figure shows both the numerical curves and the three analytical approximations above. Each of the numerical curves has three distinct segments corresponding to the three regimes of production time: in the top right, monopoles are produced in the RD period before EMD - the slope of the curve in this region is the same as that of a pure RD monopole production scenario; the central segment of the curve corresponds to production during EMD, with a slope given by Eq. (6.23); and in the bottom left section, production after EMD recovers the RD slope. The two analytical expressions for production at the beginning (Eq. (6.12)) and end (Eq. (6.13)) of EMD separate these three regimes regardless of the specific parameter values, as expected. We note that the entire curves sit at higher monopole masses when compared to a pure RD production scenario because of the offset of the hidden and visible energy densities, as shown in Eq. (6.15).

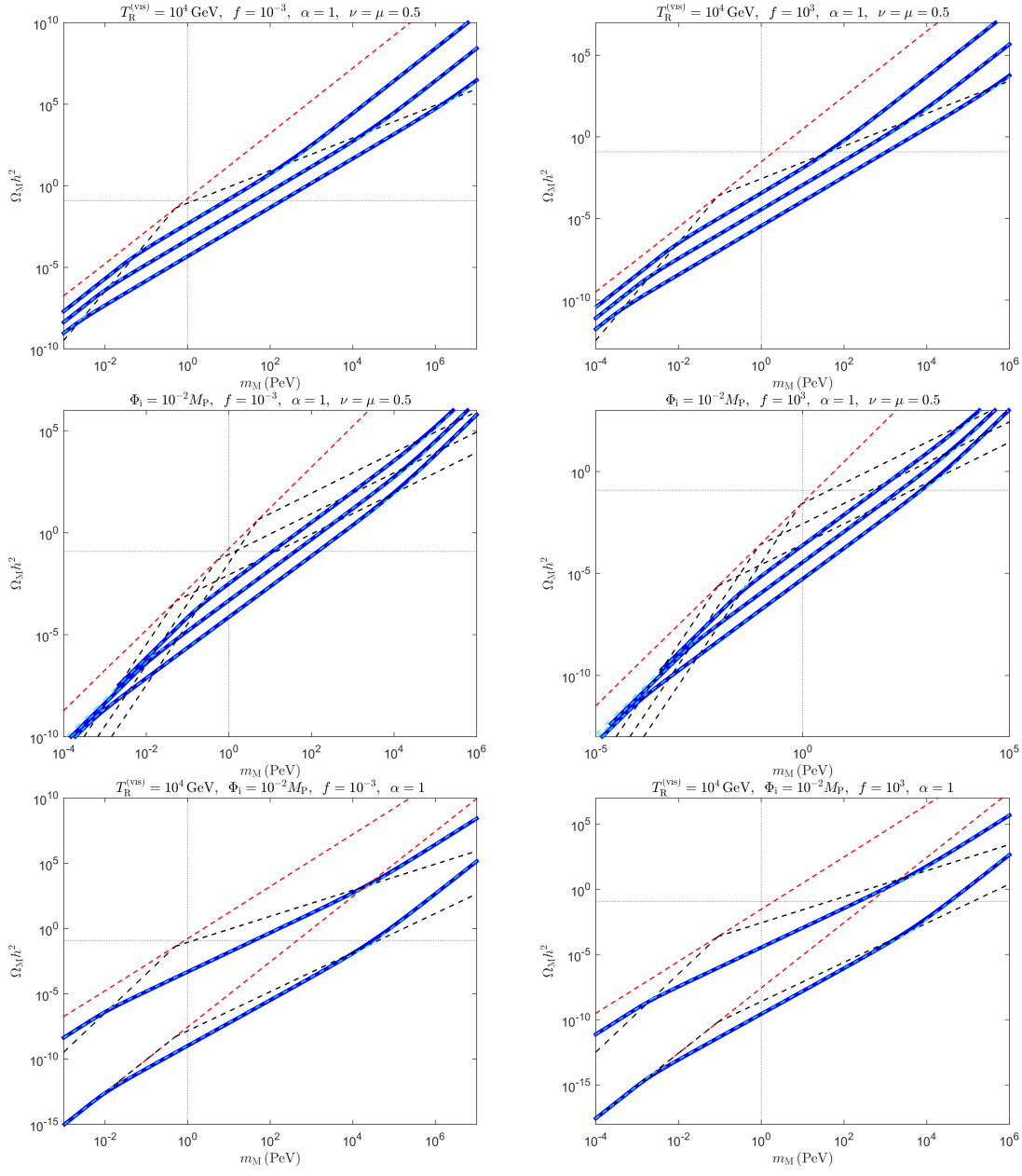


Figure 6.2: Solid curves are obtained from numerical evolution of the background while dashed lines are analytical. The red dashed line in all panels marks the purely RD equivalent scenario. Black dashed lines indicate production at the start and end of EMD. Solid blue curves correspond to (from top to bottom in each panel): $\Phi_{\rm i} = 10^{-3} M_{\rm P}$, $10^{-2} M_{\rm P}$, and $10^{-1} M_{\rm P}$ (top panels); $T_{\rm R}^{\rm (vis)} = 10^5\,{\rm GeV}$, $10^4\,{\rm GeV}$, and $10^3\,{\rm GeV}$ (middle panels); $\nu = \mu = 0.5$ and 1 (bottom panels). Left panels: initial RD by the HS. Right panels: initial RD by the VS.

## 6.6 Early matter domination by a heavy decoupled particle

Rather than being a modulus, the scalar $\Phi$ that drives the EMD phase can instead be a heavy particle which decouples from either the HS or VS at a very early time and subsequently dominates the energy density of the Universe as a nonrelativistic matter component before eventually decaying (see Figure 6.3). We will parameterize the interaction rate of $\Phi$ with the sector from which it is decoupling (the "host" sector) by the thermally averaged annihilation cross-section times relative velocity, $\langle \sigma_\Phi v \rangle$, similar to our treatment of DM decoupling in previous chapters. The Boltzmann equation for the number density of $\Phi$ is then

$$\frac{dn_\Phi}{dt} + 3Hn_\Phi = \langle \sigma_\Phi v \rangle \left(n_{\Phi,\mathrm{eq}}^2 - n_\Phi^2\right) - \Gamma_\Phi n_\Phi \,, \tag{6.25}$$

where $n_{\Phi,\mathrm{eq}}$ is the thermal equilibrium number density, and $\Gamma_\Phi$ is the decay rate. The energy density of $\Phi$ is given by $\rho_\Phi = \langle E_\Phi \rangle \, n_\Phi$, where we approximate the average energy per particle as $\langle E_\Phi \rangle \approx \sqrt{m_\Phi^2 + 9T^2}$. The temperature $T$ is that of the host sector.

If $\Phi$ decouples from the HS, the remaining two Boltzmann equations for the radiation components are

$$\frac{d\rho_\mathrm{r}^{(\mathrm{vis})}}{dt} + 4H\rho_\mathrm{r}^{(\mathrm{vis})} = \Gamma_\Phi \rho_\Phi \tag{6.26}$$

$$\frac{d\rho_\mathrm{r}^{(\mathrm{hid})}}{dt} + 4H\rho_\mathrm{r}^{(\mathrm{hid})} = \langle E_\Phi \rangle \, \langle \sigma_\Phi v \rangle \left(n_\Phi^2 - n_{\Phi,\mathrm{eq}}^2\right), \tag{6.27}$$

while if it decouples from the VS, we have

$$\frac{d\rho_\mathrm{r}^{(\mathrm{vis})}}{dt} + 4H\rho_\mathrm{r}^{(\mathrm{vis})} = \Gamma_\Phi \rho_\Phi + \langle E_\Phi \rangle \, \langle \sigma_\Phi v \rangle \left(n_\Phi^2 - n_{\Phi,\mathrm{eq}}^2\right) \tag{6.28}$$

$$\frac{d\rho_\mathrm{r}^{(\mathrm{hid})}}{dt} + 4H\rho_\mathrm{r}^{(\mathrm{hid})} = 0 \,. \tag{6.29}$$

Note that we retain the decay of $\Phi$ predominantly to the VS in order to preserve the standard history from BBN onward.[4] We numerically solve the Boltzmann equations, in both decoupling cases, for the visible and hidden radiation energy densities, as well as the number density of $\Phi$, as shown in Figure 6.4.

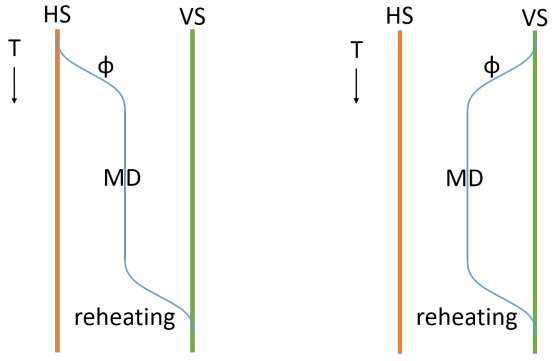


Figure 6.3: Diagram of particle $\Phi$ decoupling from either sector while always reheating to the VS.

Following the energy density evolution, we start in RD at some initial early time, with the HS and VS radiation related by the factor $f_{\rm i}$, and with negligible $\Phi$ energy density.[5] As the Universe cools, $\Phi$ decouples from the sector it was in contact with via freeze-out or freeze-in, leaving a frozen energy density that redshifts like matter once $\Phi$ becomes nonrelativistic. This matter energy density can then dominate over radiation, provided that the frozen energy density is high enough for domination to occur before the eventual decay of $\Phi$. The decay completes near $H \approx \Gamma_\Phi$, and we are subsequently left with the standard phase of domination by VS radiation.

The evolution of the thermal equilibrium number density for $\Phi$ transitions from relativistic to nonrelativistic when the temperature of the host sector drops below $m_\Phi$. Because of this transition, there is a maximum frozen number density for a given $m_\Phi$, which is achieved through the decoupling of $\Phi$ while it is relativistic and

[4] In the Boltzmann equations we do not include the possibility of $\Phi$ decay to the HS, though one can easily include it by introducing branching fractions for both sectors.

[5] One can consider a non-negligible initial energy density for $\Phi$, but that will depend on the details of specific models, so we do not consider it here.

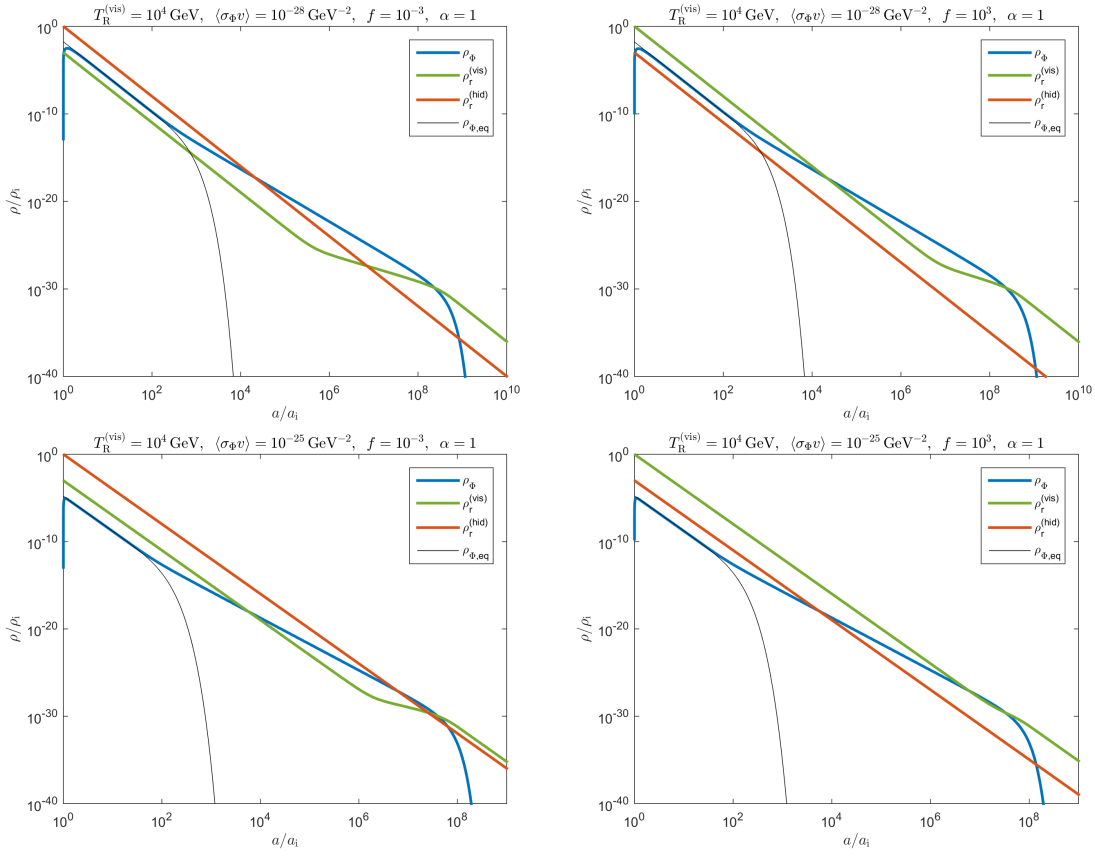


Figure 6.4: Background energy densities vs scale factor in the case of EMD by a decoupled particle. Values of $\langle\sigma_\Phi v\rangle$ are chosen to correspond to relativistic freeze-out, thus yielding the longest possible EMD phase in each panel. Left panels: initial RD by the HS. Right panels: initial RD by the VS. Top panels: $\Phi$ decoupling from the dominant sector. Bottom panels: $\Phi$ decoupling from the subdominant sector.

in equilibrium with its host sector. We call this relativistic freeze-out. If $\Phi$ were to start with a number density larger than equilibrium, annihilations would drive it down to the equilibrium density, unless the annihilation rate was too small, which is not a scenario we will consider here because we assume RD at the initial time in order to justify an origin for the intervening EMD phase. Decoupling through relativistic freeze-out results in the earliest possible start time for the EMD phase caused by $\Phi$ of a given mass, and requires the annihilation rate to be large enough such that $\Phi$ reaches equilibrium while still relativistic, but not too large such that it remains in equilibrium after becoming nonrelativistic. The value of $\langle\sigma_\Phi v\rangle$ at the transition between relativistic and nonrelativistic freeze-out can be approximated by (see Appendix A for an analogous expression concerning DM decoupling)

$$\langle\sigma_\Phi v\rangle \approx \begin{cases} \dfrac{2\pi^{5/2}\,\mathrm{e}\,{g_*^{(\mathrm{hid})}}^{1/2}(1+f_\mathrm{i})^{1/2}}{\sqrt{45}g_\Phi M_\mathrm{P} m_\Phi} & \text{HS decoupling} \\ \dfrac{2\pi^{5/2}\,\mathrm{e}\,{g_{*\mathrm{f}}^{(\mathrm{vis})}}^{1/2}(1+\frac{1}{f_\mathrm{i}})^{1/2}}{\sqrt{45}g_\Phi M_\mathrm{P} m_\Phi} & \text{VS decoupling}\,. \end{cases} \tag{6.30}$$

If the annihilation rate of $\Phi$ is large enough to maintain equilibrium with its host sector below $T \approx m_\Phi$, then decoupling will occur via nonrelativistic freeze-out, resulting in a smaller frozen number density and thus a later start time for EMD. As the annihilation rate increases further, the frozen $\Phi$ energy density decreases and the start of EMD approaches the time of reheating, resulting in a shorter duration for the EMD phase. This gives an upper limit, corresponding to $H_\mathrm{MD} \gtrsim \Gamma_\Phi$, on the value of $\langle\sigma_\Phi v\rangle$, for a given mass and decay rate (or equivalently VS reheat temperature), for EMD to happen at all:

$$\langle\sigma_\Phi v\rangle \lesssim \frac{m_\Phi}{3\Gamma_\Phi^{1/2} M_\mathrm{P}^2 H_\mathrm{f}^{1/2}}\,, \tag{6.31}$$

where $H_\mathrm{f}$ is given in Appendix E.

Now, if the annihilation rate is smaller than that needed for relativistic freeze-out, $\Phi$ will never reach thermal equilibrium and will decouple via freeze-in. Low-

ering $\langle\sigma_\Phi v\rangle$ further reduces the frozen number density, and thus the duration of EMD, down to a minimum value corresponding to the absence of EMD altogether. The value of $\langle\sigma_\Phi v\rangle$ corresponding to the transition between freeze-in and relativistic freeze-out is approximately

$$\langle\sigma_\Phi v\rangle \approx \begin{cases} \dfrac{\pi^3 {g_*^{(\mathrm{hid})}}^{1/2}(1+f_\mathrm{i})^{1/2}}{\sqrt{90}\zeta(3) g_\Phi M_\mathrm{P} T_\mathrm{i}^{(\mathrm{hid})}} & \text{HS decoupling} \\ \dfrac{\pi^3 {g_{*\mathrm{i}}^{(\mathrm{vis})}}^{1/2}(1+\frac{1}{f_\mathrm{i}})^{1/2}}{\sqrt{90}\zeta(3) g_\Phi M_\mathrm{P} T_\mathrm{i}^{(\mathrm{vis})}} & \text{VS decoupling} \end{cases} \tag{6.32}$$

and the minimum value corresponding to $H_\mathrm{MD} \gtrsim \Gamma_\Phi$ is (see Appendix E)

$$\langle\sigma_\Phi v\rangle \gtrsim \begin{cases} \dfrac{3\pi^7 {g_*^{(\mathrm{hid})}}^{3/2}(1+f_\mathrm{i})^{3/2}\Gamma_\Phi^{1/2}}{90^{3/2}\zeta(3)^2 g_\Phi^2 M_\mathrm{P} m_\Phi H_\mathrm{i}^{1/2}} & \text{HS decoupling} \\ \dfrac{3\pi^7 {g_{*\mathrm{i}}^{(\mathrm{vis})}}^{3/2}\left(1+\frac{1}{f_\mathrm{i}}\right)^{3/2}\Gamma_\Phi^{1/2}}{90^{3/2}\zeta(3)^2 g_\Phi^2 M_\mathrm{P} m_\Phi H_\mathrm{i}^{1/2}} & \text{VS decoupling} \end{cases} \tag{6.33}$$

Other than defining the range of annihilation rates that can yield an EMD phase[6], the significance of these regimes of $\langle\sigma_\Phi v\rangle$ is that a particular EMD phase, with a set start time and end time, can be established by two different values of $\langle\sigma_\Phi v\rangle$, one corresponding to freeze-out and the other to freeze-in.

The abundance of monopoles produced by the HS phase transition is determined by using Eqs. (6.8)-(6.11) and (6.21), and is given by, Eqs. (6.22), (6.23), and (6.24), in the previous section. Though these expressions were obtained in the context of $\Phi$ being a modulus, they are independent of its identity and are still valid in the cases presented in this section, provided that we use the appropriate expressions for quantities such as $H_\mathrm{MD}$.

The current monopole abundance is shown in Figure 6.5 as a function of monopole mass for some example parameter values, and we have again taken $x_\mathrm{M} \equiv m_\mathrm{M}/T_\mathrm{C}^{(\mathrm{hid})} =$

[6]We include an additional constraint in Appendix E on the parameter values that must hold for an EMD phase to have nonzero duration.

50. As in the modulus case, there are three regions corresponding to monopole production before, during, and after EMD, and the curves have the same behavior as before. The main feature that sets the decoupled-particle case apart from the modulus case is that any particular curve can be obtained by either nonrelativistic freeze-out or freeze-in, meaning the value of the annihilation rate of $\Phi$ can be quite different while still reproducing the same curve. Otherwise, the same regions are generally accessible to a modulus or decoupled-particle scenario, where the maximum extent toward larger monopole masses is set by either the maximum initial modulus amplitude or by relativistic freeze-out in the two cases respectively.

We finally note that the case of freeze-in depends on the initial host-sector temperature because freeze-in of $\Phi$ occurs in RD, such that the time of peak $\Phi$ production from the background is the initial time (see Chapter 4 for details of freeze-in during RD before EMD). In our numerical calculations, we chose the initial time arbitrarily, with an initial energy density configuration consisting of dominant radiation and negligible $\Phi$. For a given initial time, there is a unique annihilation rate that results in a particular freeze-in $\Phi$ energy density, provided that we remain within the freeze-in regime of the annihilation rate. The important thing to note is that the accessible region in $\Omega_{\rm M}h^2$ vs $m_{\rm M}$ is generally independent of the initial time because it is determined by the start and end of EMD, which can be obtained by multiple values of the initial time and annihilation rate.

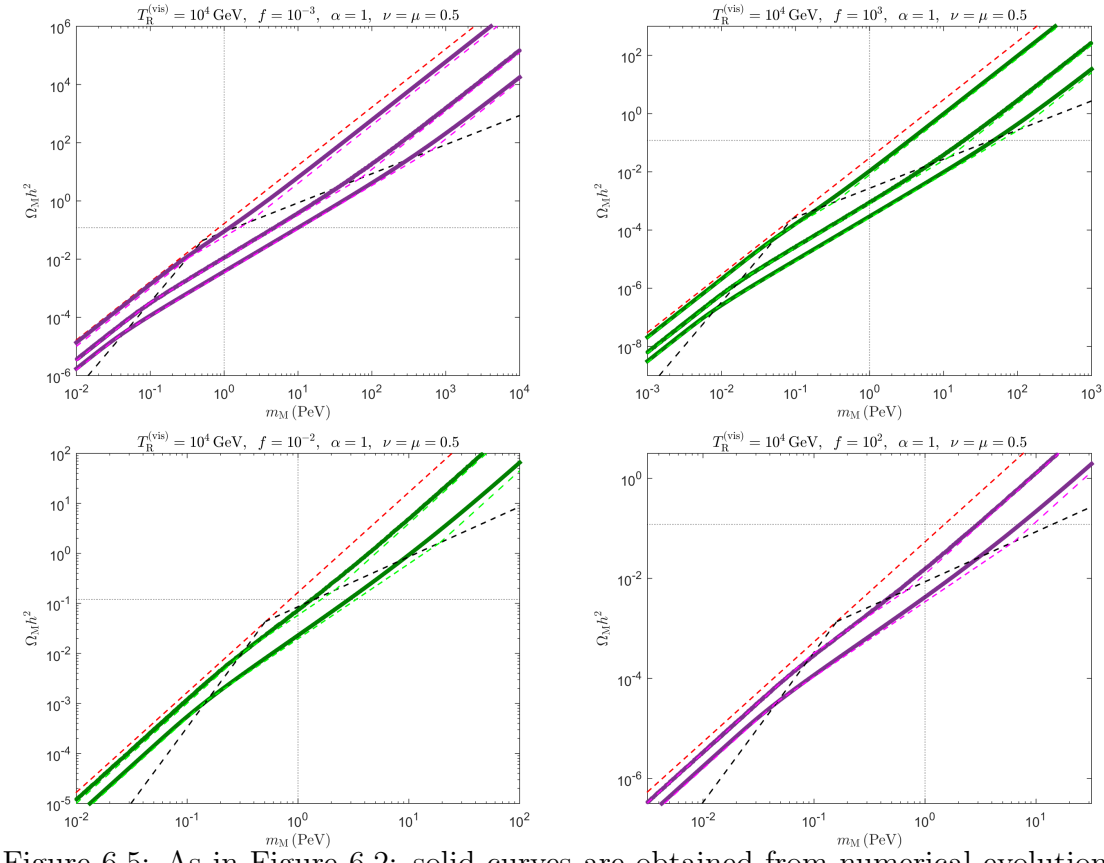


Figure 6.5: As in Figure 6.2: solid curves are obtained from numerical evolution of the background, while dashed lines are analytical. The red dashed line in all panels marks the purely RD equivalent scenario. Black dashed lines indicate production at the start and end of EMD. Solid curves correspond to (from top to bottom in each panel): $\langle\sigma_\Phi v\rangle = 10^{-31}\,\mathrm{GeV}^{-2}$, $10^{-25}\,\mathrm{GeV}^{-2}$, and $10^{-28}\,\mathrm{GeV}^{-2}$ (top panels); $\langle\sigma_\Phi v\rangle = 10^{-24}\,\mathrm{GeV}^{-2}$ and $10^{-26.5}\,\mathrm{GeV}^{-2}$ (bottom panels). Left panels: initial RD by the HS. Right panels: initial RD by the VS. Top panels: $\Phi$ decoupling from the dominant sector. Bottom panels: $\Phi$ decoupling from the subdominant sector. The curves with the largest monopole mass correspond to relativistic freeze-out of $\Phi$ in each panel. The dependence on $T_R^{(vis)}$ and the critical exponents $\nu$ and $\mu$ is the same as in Figure 6.2.

## 6.7 Discussion and conclusion

In this chapter, we have presented a scenario in which DM is composed of HS magnetic monopoles whose abundance is set by a second order phase transition in the early Universe via the KZM. Our focus has been on generalizing the thermal history of the early Universe to include an epoch of EMD, and to allow the hidden and visible sectors to have different temperatures. In doing so, we have shown that the monopole masses which are needed to reproduce the entire DM abundance are $\mathcal{O}(\text{PeV})$ and higher, and are always greater than the masses needed in an equivalent scenario that does not involve EMD. This can be understood as an effect of the significant dilution caused by the decay of the matter component as well as the offset between the visible and hidden radiation energy densities. An important assumption we have made is to restrict the decay of the matter component to only (or at least predominantly) reheat the VS, resulting in RD by the VS after EMD.

An interesting direction for further generalization of our scenario is to allow for decay of $\Phi$ to both sectors, resulting in a more complicated reheating configuration. The HS temperature, in this case, would not simply redshift through the entire EMD phase, but would adopt the late-EMD scaling which is characteristic of the end of EMD. This would add additional features to the curves in the $\Omega_{\text{M}}h^2 - m_{\text{M}}$ plane, though we do not expect this to result in monopole masses smaller than a purely RD scenario.

Because the presence of an EMD phase results in heavier monopole masses, one can imagine that an intervening phase of domination by a component with a more general equation of state can in some cases result in lighter masses. Particularly, a period of kination, in which the energy density of the Universe is dominated by the kinetic energy of a scalar field such as the inflaton, results in a redshift relation $H \propto a^{-3}$ which decreases faster than RD (for example, see [176, 177, 178]). If the HS phase transition were to occur during such a phase, the monopole mass may be

pushed to lighter masses than in the RD case.

Finally, in embedding our scenario in a specific model, one must make sure that the model-derived parameters are consistent with our cosmologically-derived parameter constraints, particularly in the case of decoupled particle $\Phi$. Additionally, it would be interesting to see the effects of any stronger coupling between the various sectors on the final monopole abundance in a realistic model.

# Chapter 7

# Conclusion

## 7.1 Summary

This dissertation has been focused on studying the effects of EMD eras on the production of DM in the early Universe. Our main motivation has been to explore the possibilities of DM production beyond the thermal WIMP paradigm as this scenario becomes increasingly constrained. We have made use of some of the rich theoretical possibilities for the pre-BBN era to investigate the parameter space for DM production with the hope that the properties of this period may be probed by future observations/experiments through DM production mechanisms.

In the first two non-introductory chapters (Chapters 3 and 4), we were concerned with the details of a generic EMD period beyond the standard picture of EMD presented in Chapter 2. Firstly, a particular EMD period can easily occur in the presence of additional fields other than the one driving the phase of altered expansion, in a generic postinflationary history. Usually, only a single field is considered at a time in the context of the entropy-generating period of EMD. However, we have shown in Chapter 3 that the presence of a subdominant second field that decays well before

the final reheating, can significantly alter the thermal history of the early Universe by injecting radiation. The parameter space that results in the correct DM abundance is then substantially changed, with regions corresponding to underproduction in a single-field scenario, now yielding too much DM. This example demonstrates the importance of the field content of the early Universe in determining the relic abundance of DM produced in that era.

Secondly, any generic EMD period must have began somehow, and the details of this beginning, as well as the prior history, can have substantial effects on DM production. A feature which appeared in the two-field scenario of Chapter 3, but which has greater significance (explored in Chapter 4), is the period of EMD where radiation simply redshifts. If the radiation energy density during, or before, a period of EMD is ever greater than the contribution from the decay of the driving component, it will not feel this contribution until it has redshifted down to an acceptable level. The significance of this is that EMD actually has two generic behaviors: the standard entropy-producing phase just before reheating, and the memory phase during which the memory of the substantial radiation gets erased. Furthermore, because DM decoupling during the memory phase, or a RD phase preceding EMD, depends on the largest relevant temperature, the DM relic abundance can be dominated by contributions that are set before the standard phase of EMD even begins. We have therefore shown that a determination of the relic DM abundance in a scenario involving EMD, requires knowledge of the prior history, as well as the presence of other fields, in large parts of the relevant parameter space.

Having discussed the significance of generic EMD periods on DM production via decoupling, the later two chapters of this dissertation (Chapters 5 and 6) focused on applications of an EMD period in scenarios with other sources of DM production. With the advent of gravitational wave astronomy, interest in PBHs has greatly increased. In relation to DM, PBHs are typically studied as possible DM candidates produced in the early Universe and surviving to the present day. We, however, were

interested in another possibility, namely that PBH evaporation can be a source of DM particles. To this end, Chapter 5 presented a scenario in which the DM relic abundance is produced by Hawking radiation from PBHs which completely evaporate before BBN. We made use of an era of EMD to allow for the formation of PBHs in an extended mass range so as to avoid requiring highly tuned values of the amplitude of the scalar power spectrum at small scales relevant for PBH formation. We have shown that PBH evaporation can yield the correct DM abundance if the scalar power spectrum is enhanced at small scales by an amount that is consistent with Planck 2015 and 2018 data. This scenario demonstrates how observations can be connected to DM production mechanisms which depend on the properties of the early Universe.

Lastly, in Chapter 6, we explored the effects of EMD in the context of a more exotic DM production scenario involving topological defects produced via the Kibble-Zurek mechanism. Due to observational constraints, we considered a second-order phase transition to occur in a HS and resulting in the production of a substantial amount of magnetic monopoles charged under a hidden U(1). We generalised such a topological DM scenario by allowing the HS and VS temperatures to be different, in addition to studying the effects of an EMD phase. We found that a period of EMD, independent of its timing before, during, or after the phase transition, results in heavier DM masses needed to obtain the current abundance than in a purely RD scenario. Because hidden sectors and phase transitions are common ingredients in early Universe models, a scenario such as this one demonstrates the flexibility of EMD eras as an additional ingredient for model building.

## 7.2 Future work

The majority of our discussion of DM production mechanisms has been focused on cosmological effects as opposed to specific particle physics details of DM and its

interactions (as well as those of the other fields). This model-independent approach has been useful for us in identifying important features without being obscured by the particular properties of a given model. However, an implementation of any of our scenarios in a realistic model is a natural next step toward the goal of probing the pre-BBN era. Though we hope to do this in the future, for now, we will touch on possible ways in which to extend our scenarios along cosmologically motivated directions.

**Continuous distributions of matter components** – Because early Universe models often involve many additional fields, and as we have seen, the presence of subdominant components can have substantial effects on DM production during EMD, it would be interesting to explore the case where there is a continuous distribution of components contributing to an overall EMD phase. Specifically, we are interested in a distribution of moduli, each decaying at their own time determined by $\Gamma_i \approx m_i^3/M_{\rm P}^2$, as well as a distribution of PBHs which can drive EMD and then evaoporate before BBN according to $t_i \approx M_i^3/M_{\rm P}^4$. We have started preliminary investigations of such scenarios, and find that one can obtain relations for $T$ and $H$ that lie between RD and MD, as one might expect due to the continuous decay of the matter components and thus continuous pumping of the radiation component. Additionally, the different expressions governing the lifetime of moduli and PBHs result in different slopes for $H(T)$. We will continue to analyze such scenarios, and examine the resultant effects on DM production.

**Generalized equations of state** – In our discussions of nonstandard thermal histories we have restricted ourselves to considering matter-like equations of state for the dominating components. However, situations may exist in which a component with a different equation of state comes to dominate the energy density of the Universe. It would therefore be useful to see how our results change when the dominating components have a more generalized equation of state resulting in $\rho \propto a^{-3(1+w)}$, where $w = 1/3$ yields radiation and $w = 0$ is matter. A particular example of this is ki-

nation: a period of domination by the kinetic energy of a scalar field. In this case, $w = 1$ and $\rho \propto a^{-6}$, which is a stronger relation than that of radiation, and could thus result in substantially different features for DM production.

**Hidden sectors** – Finally, as we saw in the case of topological DM, the inclusion of a HS can have important effects on DM production, especially when the HS has a temperature different from that of the VS. If DM particles decouple from a HS, one can imagine many new possibilities involving nonstandard thermal histories. For example, if the dominant component of the HS behaves like matter and decays to HS radiation, but the energy density of the Universe is dominated by VS radiation, one can alter the HS temperature evolution while leaving the VS unchanged. Or, as in Chapter 6, if the Universe is initially dominated by HS radiation and then undergoes a period of EMD which reheats the two sectors differently, the values of DM parameters such as its mass and annihilation rate needed to obtain the correct relic abundance may shift considerably. Such scenarios, however, introduce additional parameters which may have substantial dependence on specific particle physics implementations of the HS, and one should be careful to identify the cosmologically important parameters and their specific regimes in order to facilitate an embedding in a specific model.

# Appendix A

# Additional Introductory Material

This appendix is associated with the first two chapters, and covers some important introductory material.

## A.1 Freeze-in during RD and standard EMD

This appendix section details freeze-in production of DM during both RD and the late phase of EMD. If $\langle\sigma_{\rm ann}v\rangle$ is small enough such that DM never reaches equilibrium, we may drop $n_\chi$ in comparison to $n_{\chi,\rm eq}$ in Equation (1.5):

$$\frac{d(a^3 n_\chi)}{dt} = a^3 \langle\sigma_{\rm ann}v\rangle\, n_{\chi,\rm eq}^2\,. \tag{A.1}$$

In RD, we have $t = 1/2H$, $a \propto H^{-1/2}$, and Eq. (1.4) for $H(T)$, while in the entropy-generating phase of EMD, we have $t = 2/3H$, $a \propto H^{-2/3}$, and Eq. (2.4).

**Relativistic freeze-in during RD** – Using the relativistic expression for the equilibrium number density in Eq. (1.7) and the RD expressions above, we have

$$\frac{d(a^3 n_\chi)}{dH} = -\frac{90^{3/2}\zeta(3)^2 g_\chi^2 M_{\rm P}^3 a_{\rm i}^3 H_{\rm i}^{3/2}}{2\pi^7}\left(\frac{\langle\sigma_{\rm ann}v\rangle}{g_*^{3/2}H^{1/2}}\right) \tag{A.2}$$

where subscript 'i' indicates an arbitrary initial time. Assuming negligible initial DM abundance, we have

$$a_{\rm f}^3 n_{\chi,{\rm f}} = \frac{90^{3/2}\zeta(3)^2 g_\chi^2 M_{\rm P}^3 a_{\rm i}^3 H_{\rm i}^{3/2}}{2\pi^7} \int_{H_{\rm f}}^{H_{\rm i}} \left(\frac{\langle\sigma_{\rm ann} v\rangle}{g_*^{3/2} H^{1/2}}\right) dH\,. \tag{A.3}$$

where subscript 'f' indicates an arbitrary final time. Taking the annihilation rate to be temperature-independent and assuming that $g_*$ only changes slightly at the high temperatures of the early Universe, we are left with a simple integral that is dominated by its upper limit. The resultant number density is set by the value of $H$ at the initial time and only changes due to redshift. Dividing by the entropy density at the final time yields

$$\left(\frac{n_\chi}{s}\right)_{\rm f} \approx \left(\frac{45^{7/4}\zeta(3)^2 g_\chi^2}{2^{1/4}\pi^{15/2} g_{*{\rm f}}^{1/4} g_{*{\rm i}}^{3/2}}\right) \langle\sigma_{\rm ann} v\rangle_{\rm i} M_{\rm P}^{3/2} H_{\rm i}^{1/2}\,, \tag{A.4}$$

which is constant apart from slight changes due to $g_*(T)$. The initial time is bounded by inflation and in the standard thermal history, the RD era extends all the way back to the end of inflationary reheating without interruption. Therefore, the scale of inflationary reheating, or the maximum temperature of the RD era, determines how much DM would be produced right after. Because current observations cannot probe the pre-BBN Universe, this scale is unknown, however models based on various considerations, such as over-production of gravitinos, often place it within the range $T_{\rm reh} \sim 10^9 - 10^{15}\,{\rm GeV}$ [16, 49, 52, 158]. The relic abundance for freeze-in during RD is

$$\left(\Omega_\chi h^2\right)_{\text{freeze-in}}^{\rm (RD)} \approx \frac{117\, g_\chi^2}{g_{*{\rm f}}^{1/4} g_{*{\rm reh}}^{5/4}} \left(\frac{T_{\rm reh}}{10^{10}\,{\rm GeV}}\right) \left(\frac{m_\chi}{100\,{\rm GeV}}\right) \left(\frac{\langle\sigma_{\rm ann} v\rangle_{\rm reh}}{2\times 10^{-53}\,{\rm cm}^3\,{\rm s}^{-1}}\right) \tag{A.5}$$

where $g_{*{\rm f}}$ indicates its value once the DM number density is frozen shortly after the initial time, and we have taken the initial time to correspond to the end of inflationary reheating.

**Nonrelativistic freeze-in during RD** – We will calculate the nonrelativistic contribution to show that production while $\chi$ is relativistic dominates. Using the non-

relativistic form of $n_{\chi,\mathrm{eq}}$, we have

$$a_{\mathrm{f}}^3 n_{\chi,\mathrm{f}} = \frac{90^{3/4} g_\chi^2 m_\chi^3 M_{\mathrm{P}}^{3/2} a_{\mathrm{i}}^3 H_{\mathrm{i}}^{3/2}}{16\pi^{9/2}} \int_{H_{\mathrm{f}}}^{H_{\mathrm{i}}} \left( \frac{\langle \sigma_{\mathrm{ann}} v \rangle}{g_*^{3/4} H^2} \, \mathrm{e}^{-\frac{2m_\chi}{\sqrt{H M_{\mathrm{P}}}} \left( \frac{\pi^2 g_*}{90} \right)^{1/4}} \right) dH \,. \tag{A.6}$$

Once again pulling $\langle \sigma_{\mathrm{ann}} v \rangle$ and $g_*$ out of the integral, the integral can be written in the form $\int_{u_{\mathrm{i}}}^{u_{\mathrm{f}}} u \, \mathrm{e}^{-u} du$ which is controlled by the lower limit for $u_{\mathrm{f}} \gg u_{\mathrm{i}}$. Upon integrating, we have

$$\left( \frac{n_\chi}{s} \right)_{\mathrm{f}} \approx \left( \frac{45^{3/2} g_\chi^2}{32\sqrt{2}\pi^6 g_{*\mathrm{f}}^{1/4} g_{*\mathrm{i}}^{5/4}} \right) \mathrm{e}^{-\frac{2m_\chi}{T_{\mathrm{i}}}} \left( \frac{2m_\chi}{T_{\mathrm{i}}} + 1 \right) \langle \sigma_{\mathrm{ann}} v \rangle_{\mathrm{i}} \, m_\chi M_{\mathrm{P}} \,. \tag{A.7}$$

To compare this to Eq. (A.4), we take the initial time in both expressions to correspond to $T \approx 2m_\chi$, the approximate boundary between the two regimes, and the peak production time in the nonrelativistic case. We get that the relativistic contribution at $T \approx 2m_\chi$ is roughly 40 times larger than the nonrelativistic. Noting that this time corresponds to the largest nonrelativistic contribution and the smallest relativistic contribution, we see that freeze-in while $\chi$ is relativistic dominates.

**Nonrelativistic freeze-in during standard EMD** – Using the expressions for EMD at the beginning of this appendix section as well as the nonrelativistic form of the equilibrium number density, we have

$$\frac{d(a^3 n_\chi)}{dH} = -\frac{g_\chi^2 g_{*\mathrm{R}}^{3/8} a_{\mathrm{i}}^3 H_{\mathrm{i}}^2 M_{\mathrm{P}}^{3/4} T_{\mathrm{R}}^{3/2} m_\chi^3}{2^{7/8} 3^{1/4} 5^{3/8} \pi^{15/4}} \left( \frac{\langle \sigma_{\mathrm{ann}} v \rangle}{g_*^{3/4} H^{13/4}} \, \mathrm{e}^{-\frac{2m_\chi}{A H^{1/4}}} \right) \tag{A.8}$$

where we have defined $A \equiv T/H^{1/4}$ in Eq. (2.4). The integral over $H$ can be written as $\int_{u_{\mathrm{i}}}^{u_{\mathrm{f}}} u^8 \, \mathrm{e}^{-u} du$ from some initial to final time. The solution in terms of lower incomplete gamma functions is $\gamma(9, u_{\mathrm{f}}) - \gamma(9, u_{\mathrm{i}})$. Taking the initial time to correspond to the time when $\chi$ becomes nonrelativistic and the final time to be the end of EMD, we have $u_{\mathrm{i}} \approx 1$ and $u_{\mathrm{f}} \gg 1$. Because the integrand is strongly peaked at $T = m_\chi/4$, we can approximate the integration limits as zero and infinity such that the integral becomes $\Gamma(9) = 8!$.

Unlike the RD case, we must first redshift the frozen number density to the end of EMD before normalizing by the entropy density because the decay of the matter

component continuously generates entropy. Noting that, once frozen, $n \propto H^2$ in EMD, and normalizing by the entropy density at reheating, we have

$$\left(\frac{n_\chi}{s}\right)_{\rm R} \approx \left(\frac{1134 g_\chi^2 g_{*\rm R}^{3/2}}{\sqrt{10}\pi^6 g_{*\rm f}^3}\right) \frac{M_{\rm P} T_{\rm R}^7 \langle\sigma_{\rm ann} v\rangle_{\rm f}}{m_\chi^6} \tag{A.9}$$

where $g_{*\rm f}$ corresponds to the time of peak production, and we have used Eq. (2.1) for $H_{\rm R}$. The relic abundance for freeze-in during the late phase of EMD is then

$$\left(\Omega_\chi h^2\right)^{\rm (EMD)}_{\text{freeze-in}} \approx \frac{213\, g_\chi^2 g_{*\rm R}^{3/2}}{g_{*\rm f}^3} \left(\frac{T_{\rm reh}}{1\,{\rm GeV}}\right)^7 \left(\frac{100\,{\rm GeV}}{m_\chi}\right)^5 \left(\frac{\langle\sigma_{\rm ann} v\rangle_{\rm reh}}{10^{-31}\,{\rm cm}^3\,{\rm s}^{-1}}\right) . \tag{A.10}$$

**Relativistic freeze-in during standard EMD** – The relativistic contribution will turn out to be comparable to the nonrelativistic one above, if not slightly subdominant. Using the relativistic form of $n_{\chi,\rm eq}$, we have

$$a_{\rm f}^3 n_{\chi,\rm f} = \frac{2^{13/4}\sqrt{3}\zeta(3)^2 g_\chi^2 g_{*\rm R}^{3/4} a_{\rm i}^3 H_{\rm i}^2 T_{\rm R}^3 M_{\rm P}^{3/2}}{5^{3/4}\pi^{11/2}} \int_{H_{\rm f}}^{H_{\rm i}} \left(\frac{\langle\sigma_{\rm ann} v\rangle}{g_*^{3/2} H^{5/2}}\right) dH\,. \tag{A.11}$$

Keeping only the $H$ term in the integral, we have a simple integral dominated by its lower limit. The relativistic contribution is thus set by the final time, which we will take to be $T \approx m_\chi$, which approximately marks the transition between the two regimes. Redshifting the relativistic contribution to reheating and dividing by the entropy density there yields

$$\left(\frac{n_{\chi,\rm f}}{s}\right)_{\rm R} = \left(\frac{48\sqrt{2}\zeta(3)^2 g_\chi^2 g_{*\rm R}^{3/2}}{5^{3/2}\pi^7 g_{*\rm f}^3}\right) \frac{M_{\rm P} T_{\rm R}^7 \langle\sigma_{\rm ann} v\rangle_{\rm f}}{T_{\rm f}^6}\,. \tag{A.12}$$

Comparing this to Eq. (A.9), we see that the nonrelativistic contribution is approximately 130 times larger than the relativistic contribution. Note that the difference between the two contributions is not as large here as in the RD case because both the relativistic and nonrelativistic contributions peak near $T \approx m_\chi$ (there is some sensitivity to the exact value chosen here, however, the two contributions remain roughly comparable for a reasonable range of values). Therefore, either one of the contributions can be used to approximate the freeze-in abundance produced during the late phase of EMD, and we will typically use the nonrelativistic expression given in Eq. (A.10).

## A.2 Regimes of $\langle\sigma_{\rm ann}v\rangle_{\rm f}$ for freeze-out/in during RD and standard EMD

Here we will list the regimes of $\langle\sigma_{\rm ann}v\rangle_{\rm f}$ where freeze-out and freeze-in are valid in the cases of RD and the entropy-producing phase of EMD. Starting with a large annihilation rate such that $\chi$ is in thermal equilibrium and freeze-out occurs when $\chi$ is nonrelativistic, the freeze-out relic abundance increases as we decrease $\langle\sigma_{\rm ann}v\rangle_{\rm f}$. When $T_{\rm f} \gtrsim m_\chi$, freeze-out occurs as $\chi$ transitions to being relativistic, which corresponds to the maximum possible relic abundance for freeze-out. As we decrease $\langle\sigma_{\rm ann}v\rangle_{\rm f}$ further, the relic abundance remains roughly constant until the annihilation rate is too small to bring $\chi$ into thermal equilibrium. This marks the transition to the freeze-in regime, which extends through very small values of $\langle\sigma_{\rm ann}v\rangle_{\rm f}$. The relic abundance decreases as we decrease $\langle\sigma_{\rm ann}v\rangle_{\rm f}$ in this regime.

To estimate the values of $\langle\sigma_{\rm ann}v\rangle_{\rm f}$ that correspond to nonrelativistic freeze-out, we consider $n_{\chi,\rm eq}\langle\sigma_{\rm ann}v\rangle_{\rm f} = H_{\rm f}$, using the nonrelativistic expression for $n_{\chi,\rm eq}$ and setting $T_{\rm f} = m_\chi$. For freeze-out in RD, we use Eq. (1.4) for $H(T)$ and get

$$\langle\sigma_{\rm ann}v\rangle^{\rm (RD)}_{\rm f,\,freeze\text{-}out} \gtrsim \frac{2\pi^{5/2}\,{\rm e}\,g_{*\rm f}^{1/2}}{\sqrt{45}g_\chi M_{\rm P} m_\chi}\,, \tag{A.13}$$

while for freeze-out in the late phase of EMD, using Eq. (2.4), we have

$$\langle\sigma_{\rm ann}v\rangle^{\rm (EMD)}_{\rm f,\,freeze\text{-}out} \gtrsim \frac{\sqrt{5}\pi^{5/2}\,{\rm e}\,g_{*\rm f} m_\chi}{3g_\chi g_{*\rm R}^{1/2} M_{\rm P} T_{\rm R}^2}\,, \tag{A.14}$$

For freeze-in, the production rate of $\chi$ from the annihilation of SM particles, $n_{\chi,\rm eq}\langle\sigma_{\rm ann}v\rangle_{\rm f}$, is much less than the Hubble rate $H$. We can estimate the maximum value of $\langle\sigma_{\rm ann}v\rangle_{\rm f}$ as the one that is able to equate these two rates at the peak production time. For RD, this corresponds to the earliest time, while for standard EMD it corresponds to $T \approx m_\chi$. Using the relativistic expression for $n_{\chi,\rm eq}$ and the expressions for $H(T)$ in both RD (Eq. (1.4)) and EMD (Eq. (2.4)), we find the condition

for freeze-in in RD to be

$$\langle\sigma_{\rm ann}v\rangle^{\rm (RD)}_{\rm f,\,freeze\text{-}in} \lesssim \frac{\pi^3 g_{*\rm reh}^{1/2}}{\sqrt{90}\zeta(3)g_\chi M_{\rm P}T_{\rm reh}}\,, \tag{A.15}$$

and in the entropy-generating phase of EMD it is

$$\langle\sigma_{\rm ann}v\rangle^{\rm (EMD)}_{\rm f,\,freeze\text{-}in} \lesssim \frac{\sqrt{5}\pi^3 g_{*\rm f}m_\chi}{6\sqrt{2}\zeta(3)g_\chi g_{*\rm R}^{1/2}M_{\rm P}T_{\rm R}^2}\,, \tag{A.16}$$

where the subscript 'f' labels the peak production time in each case.

These limits are used in Figures 1.1 and 2.1 to constrain the extent of the analytical freeze-out/in lines to the values of $\langle\sigma_{\rm ann}v\rangle_{\rm f}$ where the respective assumptions hold.

## A.3 EMD from an oscillating scalar

Here we briefly discuss how an oscillating scalar field, such as a modulus, leads to a period of EMD. Though we will specifically treat moduli, the general features apply to any oscillating scalar field, such as the inflaton during inflationary reheating.

Moduli are gravitationally coupled massive scalars that arise in string theory constructions of early Universe models (see [18]). Because the gravitational interaction is suppressed by the Planck mass, we will begin by considering a free scalar field.

The Lagrangian density for a free scalar field $\phi$ with mass $m_\phi$ is

$$\mathcal{L} = \frac{1}{2}\partial^\mu\phi\partial_\mu\phi - \frac{1}{2}m_\phi^2\phi^2 \tag{A.17}$$

with corresponding energy-momentum tensor

$$T^{\mu\nu} = \partial^\mu\phi\partial^\nu\phi - \mathcal{L}g^{\mu\nu}\,. \tag{A.18}$$

If we assume spatial homogeneity on cosmic scales for the field $\phi$, the energy density and pressure are

$$\rho_\phi = \frac{1}{2}\dot{\phi}^2 + \frac{1}{2}m_\phi^2\phi^2 \quad \text{and} \quad p_\phi = \frac{1}{2}\dot{\phi}^2 - \frac{1}{2}m_\phi^2\phi^2\,. \tag{A.19}$$

where dots denote time derivatives.

Allowing for decays of $\phi$ into lighter particle species, the equation of motion of $\phi$ in the expanding background is [10]

$$\ddot{\phi} + (3H + \Gamma_\phi)\dot{\phi} + m_\phi^2 \phi = 0\,. \tag{A.20}$$

where $H$ is the Hubble expansion rate and $\Gamma_\phi$ is the total decay rate. If we consider a modulus with only gravitational interaction, the decay rate is $\Gamma_\phi \sim m_\phi^3/M_{\rm P}^2$.

When $H \gg m_\phi, \Gamma_\phi$, and taking $\ddot{\phi} \approx 0$ initially, we have $\dot{\phi} \approx -m_\phi^2\phi/3H$ which results in $\phi(H) \approx \phi_{\rm i} e^{-m_\phi^2/12H^2}$ if we assume initial RD such that $H = 1/2t$. Thus $\phi$ is roughly constant as long as $H \gg m_\phi$, and the corresponding energy density is $\rho_\phi \approx \frac{1}{2} m_\phi^2 \phi_{\rm i}^2$. This period of constant energy density lasts until $H \approx m_\phi$, after which we transition to an oscillatory phase. Averaging over the oscillations in the regime $H \ll m_\phi$ results in $\rho_\phi = \langle \dot{\phi} \rangle^2$ and $p_\phi = 0$, since the effective frequency is dominated by $m_\phi$. The equation of motion can then be written as

$$\dot{\rho}_\phi + 3H\rho_\phi = -\Gamma_\phi \rho_\phi \tag{A.21}$$

which is the equation for a decaying matter energy density component.

We have numerically solved the equation of motion together with the equation for the radiation energy density using $H = \sqrt{(\rho_{\rm r} + \rho_\phi)/3M_{\rm P}^2}$ in the case that we begin in RD with $\ddot{\phi} = 0$. The resultant energy density evolution is shown in Figure A.1.

Because the energy density of $\phi$ begins constant and then redshifts as matter, it can quickly dominate over radiation. The onset of EMD can be estimated in the following way. Generic arguments based on effective field theory estimates [31, 32, 33, 34], or explicit calculations [179], suggest that the initial amplitude of oscillations is $\phi_{\rm i} \gtrsim \mathcal{O}(0.1\, M_{\rm P})$. The Hubble rate once $\phi$ is dominant is $H \approx \sqrt{\rho_\phi/3M_{\rm P}^2}$ which, using the energy density of $\phi$ in the constant regime, yields $H \approx m_\phi$ for $\phi_{\rm i} \approx M_{\rm P}$. This time marks the beginning of the oscillatory phase where $\phi$ behaves like matter,

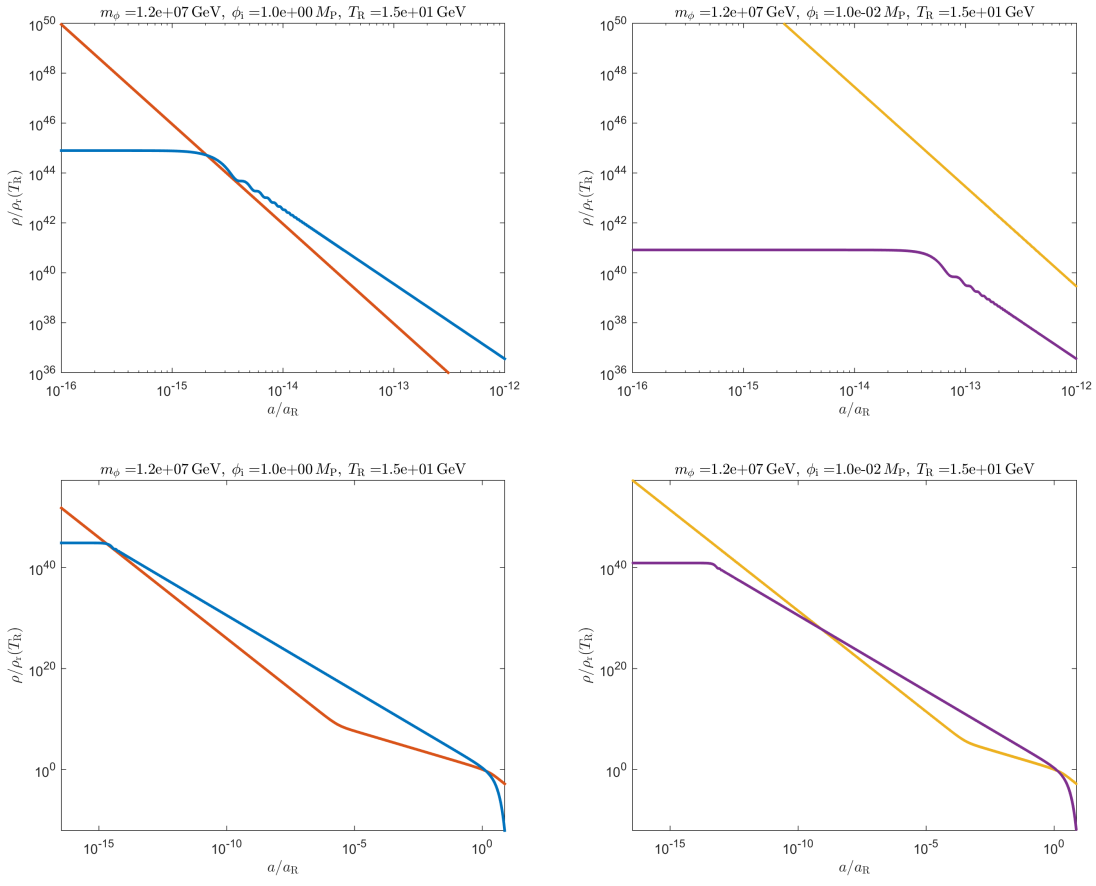


Figure A.1: Numerical evolution of the energy density in a scalar field as it begins to oscillate. The oscillating curve corresponds to the energy density of the scalar field in all panels, while the other curve depicts the radiation energy density. Top Panels show the onset of oscillation and matter-like redshift of the field in detail. Bottom panels show the entire evolution through eventual decay for the same parameters. Left panels correspond to a Planckian initial amplitude, while in the right panels it is smaller.

and therefore for maximal amplitudes, EMD starts near the same time as oscillations, which can be seen in the left panels of Figure A.1. For smaller amplitudes, $\phi$ will nevertheless begin oscillating at $H \approx m_\phi$, after which it will redshift slower than radiation leading to eventual domination as long as the lifetime of $\phi$ is long enough, as seen in the right panels of Figure A.1. EMD ends once the decay of $\phi$ completes near $H \approx \Gamma_\phi$.

## A.4 Relativistic degrees of freedom

Throughout this dissertation, we use a continuous function to capture the temperature dependence of the number of relativistic degrees of freedom $g_*(T)$, particularly in our numerical calculations. Figure A.2 shows $g_*$ as a function of temperature in the range that shows all of the major changes. When all SM species are relativistic, for $T > 100\,\mathrm{GeV}$, we have $g_* = 106.75$. This drops slightly as the W and Z bosons become nonrelativistic, and decreases abruptly after the QCD phase transition, which we take to be at $T \approx 170\,\mathrm{MeV}$. As the temperature drops below $100\,\mathrm{MeV}$, only electrons, positrons, neutrinos and photons are relativistic and we have $g_* = 10.75$ (where we have assumed 3 neutrino species). Finally, once $T \approx 1\,\mathrm{MeV}$ around the time of neutrino decoupling, $g_*$ drops to 3.36. Note that Neutrinos are still relativistic after they decouple, but their temperature differs from the photon temperature due to electron-positron annihilation, which increases the comoving number density of photons but not the decoupled neutrinos [10]. Because of these different temperatures, the relativistic degrees of freedom for entropy, $h_*$, differs from $g_*$ at this time. Accounting for the different temperatures with $T_\nu = (4/11)^{1/3} T_\gamma$ gives $h_* = 3.9$ after neutrino decoupling and electron-positron annihilation.

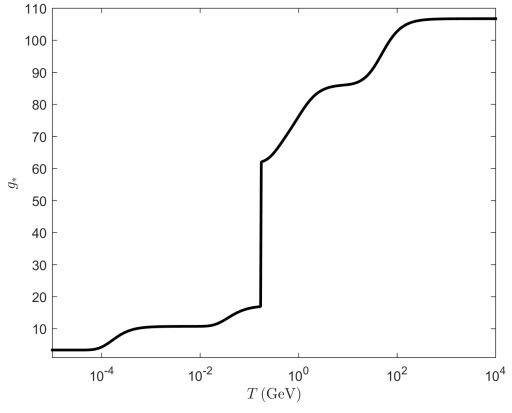


Figure A.2: Relativistic degrees of freedom in the SM, $g_*(T)$ as a function of temperature.

# Appendix B

# Additional Details for Chapter 3

In this appendix, we derive the temperature dependence of the two-field transition regime, as well as the freeze-in abundance of DM produced during this period.

## B.1 Temperature during the transition regime

Here, we first derive an expression for the instantaneous temperature of the Universe in the transition regime of the two-field scenario discussed in Section 3.2. The last equation in (3.2), assuming that $H \gg \Gamma_\phi$, results in:

$$\frac{d(a^4\rho_{\rm r})}{dt} \approx \left(1 + \alpha f e^{-\Gamma_\varphi t}\right) \Gamma_\phi \rho_\phi a^4 \,. \tag{B.1}$$

Noting that $\rho_\phi a^3 \approx$ const in this case, and that $a \propto t^{2/3}$ during EMD, we find:

$$\frac{d(a^4\rho_{\rm r})}{dt} \approx \left(1 + \alpha f e^{-\Gamma_\varphi t}\right) \Gamma_\phi \rho_{\phi,{\rm i}} a_{\rm i}^4 \left(\frac{t}{t_{\rm i}}\right)^{2/3} , \tag{B.2}$$

where $t_{\rm i}$ is an initial time that we take to be the onset of the late stage of EMD. Then $\rho_{\rm r,i} = 0$, and integrating both sides of (B.2) gives:

$$a^4\rho_{\rm r} \approx \Gamma_\phi \rho_{\phi,{\rm i}} a_{\rm i}^4 t_{\rm i}^{-2/3} \left(I_1 + \alpha f I_2\right) , \tag{B.3}$$

where

$$I_1 \equiv \frac{3}{5}(t^{5/3} - t_i^{5/3}) \quad , \quad I_2 \equiv \Gamma_\varphi^{-5/3}\left[\gamma(5/3, \Gamma_\varphi t) - \gamma(5/3, \Gamma_\varphi t_{\rm i})\right] . \tag{B.4}$$

Here, $\gamma$ denotes the lower incomplete gamma function. We can now solve for $\rho_{\rm r}$ and in turn get the corresponding temperature from $\rho_{\rm r} = (\pi^2/30) g_* T^4$, making use of $\rho_{\phi,{\rm i}} \approx 3H_{\rm i}^2 M_{\rm P}^2$ and $t_{\rm i} = 2/3H_{\rm i}$:

$$T \approx \left(\frac{40\Gamma_\phi M_{\rm P}^2}{\pi^2 g_*}\right)^{1/4} \left(\frac{I_1 + \alpha f I_2}{t^{8/3}}\right)^{1/4} \tag{B.5}$$

Since $t \gg \Gamma_\varphi^{-1}$ in the transition regime, and noting that $t_{\rm i} \ll \Gamma_\varphi^{-1}$, the incomplete gamma functions in $I_2$ approach $\Gamma_\varphi^{-5/3}\Gamma(5/3)$ and $(3/5)t_{\rm i}^{5/3}$ respectively, leading to:

$$I_1 + \alpha f I_2 \approx \frac{3}{5} t^{5/3} + \alpha f \Gamma_\varphi^{-5/3}\Gamma(5/3)\,. \tag{B.6}$$

During the transition regime, the second term on the right-hand side of this expression dominates. After using $\Gamma_\varphi = \alpha\Gamma_\phi$ and Eq. (2.1), we find:

$$T \approx \left(\frac{22.5}{g_{*\rm R}^{1/3} g_*}\right)^{1/4} \left(\frac{H^2 M_{\rm P}^2}{T_{\rm R}}\right)^{1/3} \alpha^{-1/6} f^{1/4}\,. \tag{B.7}$$

The first term on the right-hand side of Eq. (B.6) will eventually take over as it increases in time. At that point, the expression in Eq. (B.5) is precisely reduced to that in the single-field scenario given in Eq. (2.4). Therefore, we can approximately find the time after which the effect of the second field completely disappears by equating the two terms on the rhs of (B.6). This yields:

$$H_{\rm tran} \simeq 0.5 \left(\frac{\pi^2 g_{*\rm R}}{90}\right)^{1/2} \frac{T_{\rm R}^2}{M_{\rm P}} \alpha^{2/5} f^{-3/5}\,, \tag{B.8}$$

where $\Gamma_\phi < H \lesssim H_{\rm tran}$ corresponds to the single-field regime.

## B.2 Freeze-in during the transition regime

Here, we derive the abundance of DM produced via freeze-in during the transition regime. From Eq. (3.6), noting that $n_\chi \ll n_{\chi,\rm eq}$ in the case of freeze-in, we find:

$$\frac{d(a^3 n_\chi)}{dt} \approx a^3 \left\langle \sigma_{\rm ann} v \right\rangle_{\rm f} n_{\chi,\rm eq}^2 \,. \tag{B.9}$$

After converting $dt$ to $dH$, this equation becomes:

$$\frac{d(a^3 n_\chi)}{dH} \approx \frac{-2\Gamma_\varphi^2}{3H^4} a_\varphi^3 \left\langle \sigma_{\rm ann} v \right\rangle_{\rm f} n_{\chi,\rm eq}^2 \,. \tag{B.10}$$

Here, we have used $t = 2/3H$ and $a^3 = a_\varphi^3 (\Gamma_\varphi/H)^2$ during EMD, where $a_\varphi$ is the value of the scale factor at the onset of the transition regime $H \simeq \Gamma_\varphi$. Starting at temperatures $T \gg m_\chi$, and assuming that $\chi$ represents one degree of freedom, the equilibrium number density is $n_{\chi,\rm eq} = (\zeta(3)/\pi^2) g_\chi T^3$. We thus have:

$$\frac{d(a^3 n_\chi)}{dH} \approx \frac{-2\zeta(3)^2}{3\pi^4} \frac{T^6}{H^4} \left\langle \sigma_{\rm ann} v \right\rangle_{\rm f} \Gamma_\varphi^2 a_\varphi^3 \,. \tag{B.11}$$

After using Eq. (B.7), this becomes:

$$\frac{d(a^3 n_\chi)}{dH} \approx -\left( \frac{22.5}{g_{*\rm R}^{1/3} g_*} \right)^{3/2} \frac{2\zeta(3)^2}{3\pi^4} \alpha^{-1} f^{3/2} \frac{M_{\rm P}^4}{T_{\rm R}^2} \left\langle \sigma_{\rm ann} v \right\rangle_{\rm f} \Gamma_\varphi^2 a_\varphi^3 . \tag{B.12}$$

The integral of the rhs over $H$ is controlled by the largest value of $H$ during the transition regime, namely $\Gamma_\varphi$. After using $a^3 = a_\varphi^3 (\Gamma_\varphi/H)^2$ once again, and $\Gamma_\varphi = \alpha \Gamma_\phi$, we find:

$$n_\chi \approx \left( \frac{22.5}{g_{*\rm R}^{1/3} g_{*\varphi}} \right)^{3/2} \frac{2\zeta(3)^2}{3\pi^4} f^{3/2} \frac{\Gamma_\phi M_{\rm P}^4 H^2}{T_{\rm R}^2} \left\langle \sigma_{\rm ann} v \right\rangle_{\rm f} \,, \tag{B.13}$$

where $g_{*\varphi}$ is the number of relativistic degrees of freedom at $H = \Gamma_\varphi$. After normalizing this frozen number density by the entropy density at the end of EMD, and using the expression in Eq. (2.1), we arrive at:

$$\frac{n_\chi}{s} \approx (4 g_{*\varphi})^{-3/2} \frac{15\zeta(3)^2}{\pi^3} f^{3/2} (T_{\rm R} M_{\rm P}) \left\langle \sigma_{\rm ann} v \right\rangle_{\rm f} \,. \tag{B.14}$$

This can be directly used to find $\Omega_\chi h^2$ (where we have dropped an overall proportionality factor):

$$\left(\Omega_\chi h^2\right)_{\text{f.i.}}^{\text{tran}} \propto f^{3/2}(T_{\text{R}} M_{\text{P}}) \left(\frac{m_\chi}{1\text{GeV}}\right) \langle\sigma_{\text{ann}} v\rangle_{\text{f}} \ . \tag{B.15}$$

We note that Eq. (B.13) is obtained by integrating the expression in (B.12) for a constant $\langle\sigma_{\text{ann}} v\rangle_{\text{f}}$, which we have considered throughout Chapter 3. In cases where $\langle\sigma_{\text{ann}} v\rangle_{\text{f}} \propto T^n$, with $n > 0$, freeze-in during the transition regime yields a higher DM abundance. The enhancement is more significant for a strong temperature dependence of $\langle\sigma_{\text{ann}} v\rangle_{\text{f}}$, like models studied in [63, 180].

# Appendix C

# Additional Details for Chapter 4

In this appendix, we obtain the pre-EMD freeze-in contribution to the DM relic abundance.

## C.1 Regimes of pre-EMD freeze-in production

Here, we present the details of calculating the DM freeze-in abundance produced prior to EMD as well as in the memory phase of EMD.

We will begin with the late phase of EMD, i.e. $H \ll H_{\rm tran}$ (see Eq. (4.4)). In the freeze-in scenario, the rate for production of DM particles from the annihilation of SM particles, $\Gamma_\chi = \langle \sigma_{\rm ann} v \rangle_{\rm f}\, n_{\chi,{\rm eq}}$, is, by definition, small compared to the Hubble rate $H$. At sufficiently high temperatures, $T \gg m_\chi$, we have $n_{\chi,{\rm eq}} \propto T^3$. Assuming that $\langle \sigma_{\rm ann} v \rangle_{\rm f}$ is constant, as mentioned before, and using the expression in Eq. (4.1), we see that $\Gamma_\chi \propto H^{3/4}$. This implies that the freeze-in condition is satisfied more strongly at earlier times (equivalently higher temperatures). Then, since $n_{\chi,{\rm eq}}$ and $\Gamma_\chi$ are Boltzmann suppressed at $T \ll m_\chi$, DM particles will not reach chemical equilibrium during EMD provided that $\Gamma_\chi \ll H$ when $T \sim m_\chi$.

The situation, however, is different prior to the entropy generating phase of EMD (i.e. $H \gtrsim H_{\rm tran}$). In the RD phase after inflationary reheating, see Eq. (4.3), $T \propto H^{1/2}$ implying that $\Gamma_\chi \propto H^{3/2}$, while, during the memory phase of EMD, see Eq. (4.5), $T \propto H^{2/3}$ and hence $\Gamma_\chi \propto H^2$. As a result, DM production becomes more efficient at earlier times (higher temperatures) for $H \gtrsim H_{\rm tran}$. Then, in order for DM to not be in chemical equilibrium with the thermal bath prior to the entropy generating EMD epoch, we need $\Gamma_\chi \ll H$ at $H \simeq H_{\rm reh}$. Based on this, DM production at $H_{\rm tran} \lesssim H \lesssim H_{\rm reh}$ has two regimes, which we discuss separately below.

**Decoupling regime** – Production of DM from SM particles in the thermal bath will be inefficient, and DM will never reach chemical equilibrium in the postinflationary Universe, if $\Gamma_\chi \ll H$ when $H \simeq H_{\rm reh}$. This is the case if:

$$\langle \sigma_{\rm ann} v \rangle_{\rm f} \ll \frac{\pi^3 g_{*\rm reh}^{1/2}}{\sqrt{90}\zeta(3) M_{\rm P} T_{\rm reh}} \,. \tag{C.1}$$

In this regime, $n_\chi \ll n_{\chi,\rm eq}$ and the third equation of Eq. (4.8) results in:

$$\frac{d(a^3 n_\chi)}{dt} \approx a^3 \langle \sigma_{\rm ann} v \rangle_{\rm f} \, n_{\chi,\rm eq}^2 \,. \tag{C.2}$$

Integrating both sides between $H_{\rm tran}$ and $H_{\rm reh}$, and after converting $dt$ to $dH$, the comoving number density of DM is found to be:

$$(a^3 n_\chi)_{\rm dec} \simeq \frac{\zeta(3)^2}{\pi^4} \langle \sigma_{\rm ann} v \rangle_{\rm f} \left( \int_{H_{\rm tran}}^{H_0} \frac{2T^6 a^3}{3H^2} dH + \int_{H_0}^{H_{\rm reh}} \frac{T^6 a^3}{2H^2} dH \right) . \tag{C.3}$$

Here, we have used $t = 2/3H$ for $H_{\rm R} \lesssim H \lesssim H_0$, $t = 1/2H$ for $H_0 \lesssim H \lesssim H_{\rm reh}$, and $n_{\chi,\rm eq} = \zeta(3) T^3/\pi^2$ as $T \gg m_\chi$ for much of the pre-EMD phases and $n_{\chi,\rm eq}$ is Boltzmann suppressed for lower temperatures. We have taken $\langle \sigma_{\rm ann} v \rangle_{\rm f}$ out of the integrals as it is assumed to be a constant.

Using the relation in Eq. (4.3) and $a \propto H^{-1/2}$ for $H_0 \lesssim H \lesssim H_{\rm reh}$, as well as the relation in Eq. (4.5) and $a \propto H^{-2/3}$ for $H_{\rm R} \lesssim H \lesssim H_0$, we see that both integrals on the rhs of (C.3) are dominated by their upper limit. Thus, for $H_{\rm reh} \gg H_0$, production prior to EMD dominates over the memory phase. We are interested

in $n_\chi$ normalized by the entropy density $s = 2\pi^2 g_* T^3/45$ once significant entropy production has stopped, where $T = T_{\rm R}$, which results in:

$$\left(\frac{n_\chi}{s}\right)_{\rm dec} \simeq \frac{45\sqrt{90}\zeta(3)^2}{2\pi^7 g_{*\rm reh}^{5/4} g_{*0}^{1/4}} \left\langle\sigma_{\rm ann} v\right\rangle_{\rm f} M_{\rm P} \left(\frac{T_{\rm reh} T_{\rm R}}{T_0}\right) . \tag{C.4}$$

**Early-equilibrium regime** – If $\Gamma_\chi \gtrsim H$ when $H \simeq H_{\rm reh}$, then DM particles will initially be in chemical equilibrium with the thermal bath in the postinflationary Universe. This is satisfied if:

$$\left\langle\sigma_{\rm ann} v\right\rangle_{\rm f} \gtrsim \frac{\pi^3 g_{*\rm reh}^{1/2}}{\sqrt{90}\zeta(3) M_{\rm P} T_{\rm reh}} . \tag{C.5}$$

However, as mentioned before, $\Gamma_\chi$ decreases more quickly with time than $H$ in the prior RD and memory periods. This implies that DM can drop out of chemical equilibrium sometime prior to the late EMD phase and stay so during the rest of the EMD epoch. DM chemical decoupling occurs at a temperature $T_{\rm dec}$, where $T_{\rm tran} \lesssim T_{\rm dec} \lesssim T_{\rm reh}$, at which $\Gamma_\chi$ drops below $H$. We note that for very high DM masses, such that $T_{\rm tran} \ll m_\chi$, decoupling would have to happen before $T \sim m_\chi$ in order to avoid transitioning to a freeze-out regime.

The number density of DM particles follows its equilibrium value $n_{\chi,\rm eq} \propto T^3$ down to $T_{\rm dec}$. At lower temperatures, $n_\chi$ is redshifted $\propto a^{-3}$ due to expansion of the Universe and the comoving number density of DM remains essentially constant. Since production of radiation from the decaying component(s) driving EMD is negligible for $H_{\rm tran} \lesssim H \lesssim H_{\rm reh}$, the comoving entropy density is constant implying that $n_\chi \propto g_* T^3$ in this interval. We then find:

$$(a^3 n_\chi)_{\text{e-eq}} \simeq \frac{\zeta(3) g_{*0}}{\pi^2 g_{*\rm dec}} T_0^3 a_0^3 . \tag{C.6}$$

Eventually, after normalizing $n_\chi$ by $s$ at the end of EMD where $T = T_{\rm R}$, we arrive at:

$$\left(\frac{n_\chi}{s}\right)_{\text{e-eq}} \simeq \frac{45\zeta(3)}{2\pi^4 g_{*\rm dec}} \left(\frac{T_{\rm R}}{T_0}\right) . \tag{C.7}$$

An important point to keep in mind is that in both of the decoupling and early-equilibrium regimes, Eqs. (C.4) and (C.7) respectively, the relic abundance is set by DM production in the pre-EMD phase. In the decoupling regime, production at $T \simeq T_{\rm reh}$ makes the most important contribution. While, in the early-equilibrium regime, DM particles reach chemical equilibrium in the pre-EMD era and their comoving number density remains constant upon decoupling.

# Appendix D

# Additional Details for Chapter 5

In this appendix, we consider the difference in the number of $e$-folds between the scale $k_{\max}$ and the pivot scale $k_*$, as well as the contribution to the DM abundance from the evaporation of PBHs of all masses in the extended mass range.

## D.1 Number of relevant $e$-folds

For the standard thermal history, the number of $e$-folds of inflation between the time when the pivot scale $k_* = 0.05\,\mathrm{Mpc}^{-1}$ left the horizon and the end of inflation is given by [48, 49]

$$N_{k_*} \approx 63.5 + \frac{1}{4}\ln\frac{3H_{\rm inf}^2}{(8\pi M_{\rm P})^2} + \frac{1}{6}\ln\frac{H_{\rm reh}}{H_{\rm inf}}\,. \tag{D.1}$$

Here $H_{\rm inf}$ and $H_{\rm reh}$ denote the Hubble rate at the end of inflation and when reheating after inflation completes respectively, assuming that the Universe has the same equation of state as a MD phase for $H_{\rm reh} < H < H_{\rm inf}$. In the presence of an epoch of EMD for $H_{\rm R} < H < H_0$, this relation is modified as follows:

$$N_{k_*} \approx 63.5 + \frac{1}{4}\ln\frac{3H_{\rm inf}^2}{(8\pi M_{\rm P})^2} + \frac{1}{6}\ln\frac{H_{\rm reh}}{H_{\rm inf}} + \frac{1}{6}\ln\frac{H_{\rm R}}{H_0}\,. \tag{D.2}$$

The number of $e$-folds relevant for the mode $k_0$ that enters the horizon at the start of EMD when $H = H_0$ is given by

$$N_0 = \frac{1}{3} \ln \frac{H_{\rm inf}}{H_{\rm reh}} + \frac{1}{2} \ln \frac{H_{\rm reh}}{H_0} \,. \tag{D.3}$$

The terms on the rhs of the equation take evolution in the MD phase between $H_{\rm inf}$ and $H_{\rm reh}$ and the RD phase between $H_{\rm reh}$ and $H_0$, respectively, into account. The number of $e$-folds relevant for the mode $k_{\rm max}$ that eventually collapses to form PBHs with mass $M_{\rm max}$ follows from

$$N_{k_{\rm max}} - N_0 = \frac{1}{3} \ln \frac{H_0}{H_{\rm max}} \,, \tag{D.4}$$

where $H_{\rm max} = 4\pi M_{\rm P}^2 / M_{\rm max}$ is the Hubble rate when the mode $k_{\rm max}$ enters the horizon.

After using Eqs. (D.2), (D.3), (D.4), and (5.5), we find

$$N_{k_*} - N_{k_{\rm max}} \approx 47.7 + \frac{1}{4} \ln \delta(M_{\rm max}). \tag{D.5}$$

It is interesting to note that $H_{\rm inf}$ does not appear in this expression. However, it implicitly enters as we must have $H_0 \leq H_{\rm reh} \leq H_{\rm inf}$. For the shaded bands shown in Figure 5.2, we get $N_{k_*} - N_{k_{\rm max}} \approx 46.4 - 46.5$.

## D.2 Integrating over PBHs in an extended mass range

Here we derive the total contribution from evaporation of PBHs within a mass range $M_{\rm min} \leq M \leq M_{\rm max}$ to the DM relic abundance. For simplicity, we assume that ${\rm Br}_\chi = 1$ in this derivation, but including ${\rm Br}_\chi$ in the calculation is straightforward. In general, the number density of regions with mass $M$ in the early Universe can be written as

$$n(M) = \frac{\rho_{\rm tot}}{M} \,, \tag{D.6}$$

where $\rho_{\rm tot}$ is the total energy density of the Universe. Then the number density of PBHs whose mass is between $M$ and $M + dM$ follows from

$$dn_{\rm PBH}(M) = \beta(M) dn(M)\,. \tag{D.7}$$

Since $\rho_{\rm tot}$ does not depend on $M$, we have $dn(M)M = -n(M)dM$. This results in

$$dn_{\rm PBH}(M) = \frac{\beta(M) n(M)}{M} dM = \rho_{\rm tot} \frac{\beta(M)}{M^2} dM\,, \tag{D.8}$$

and hence

$$\frac{\rho_{\rm PBH}}{\rho_{\rm tot}} = \frac{1}{\rho_{\rm tot}} \int_{M_{\rm min}}^{M_{\rm max}} M dn_{\rm PBH}(M) = \int_{M_{\rm min}}^{M_{\rm max}} \frac{\beta(M)}{M} dM\,. \tag{D.9}$$

Also, after using the relation $\rho_{\rm tot}/s = 3T_{\rm R}/4$ at the end of the EMD epoch, we find

$$\frac{dn_{\rm PBH}(M)}{s} = \frac{3}{4} T_{\rm R} \frac{\beta(M)}{M^2} dM\,. \tag{D.10}$$

The corresponding contribution to the DM relic abundance, see Eq. (5.8), is given by

$$\frac{dn_\chi}{s} \approx \frac{dn_{\rm PBH}(M)}{s} \frac{M^2}{M_{\rm P}^2}\,. \tag{D.11}$$

After integrating over the entire mass range, we derive the analogue of Eq. (5.10),

$$\frac{n_\chi}{s} \approx \int_{M_{\rm min}}^{M_{\rm max}} \frac{3T_{\rm R}}{4M_{\rm P}^2} \beta(M) dM\,, \tag{D.12}$$

which generalizes Eq. (5.12) to:

$$\int_{M_{\rm min}}^{M_{\rm max}} \beta(M) \left(\frac{H_{\rm R}}{M_{\rm P}}\right)^{1/2} \left(\frac{106.75}{g_{*\rm R}}\right)^{1/4} \frac{dM}{2\times 10^8\,{\rm g}} \simeq 10^{-23} \left(\frac{100\,{\rm GeV}}{m_\chi}\right)\,, \tag{D.13}$$

where $\beta(M)$ is the theoretical prediction given in Eq. (5.2).

If $\beta(M)$ varies slowly in the mass range $M_{\rm min} \le M \le M_{\rm max}$, the above integral is $\propto M_{\rm max}$ and Eq. (D.13) reproduces the bound in (5.13). The same conclusion holds as long as the minimum of $\beta(M)$ does not happen around $M_{\rm max}$. We expect this to be the case if the range of modes over which the power spectrum is enhanced includes $k_{\rm max}$.

# Appendix E

# Additional Details for Chapter 6

In this appendix, we provide some useful parameters in comparing topological DM scenarios with or without an EMD phase, as well as some relevant details for an EMD phase caused by a heavy decoupled particle in various cases.

## E.1 The factors $f_{\rm R}$ and $e_{\rm f}$

At the end of EMD, as $\Phi$ completes its decay and reheats the VS, the ratio of the radiation energy densities of the two sectors becomes fixed as

$$f_{\rm R} = \frac{\rho_{\rm r,R}^{\rm (vis)}}{\rho_{\rm r,R}^{\rm (hid)}} \,, \tag{E.1}$$

where the additional subscript 'R' on the energy densities indicates their value at reheating. To facilitate our comparison between scenarios which include a phase of EMD and those which remain purely RD, we define the factor

$$e_{\rm f} \equiv \frac{f_{\rm R}^{\rm (EMD)}}{f^{\rm (RD)}} \,, \tag{E.2}$$

where we have included a superscript on $f_{\rm R}$ for clarity (whenever $f$ appears without a superscript label, it refers to the EMD case). The energy density ratio in a purely RD

scenario corresponding to an EMD scenario with initial domination by VS radiation is given by $f^{(\mathrm{RD})} = f_{\mathrm{i}}$, while in the case of an EMD scenario with initial domination by HS radiation, it is $f^{(\mathrm{RD})} = 1$.

The factor $e_{\mathrm{f}}$ is determined by the duration of the EMD phase, and we can approximate it in the following way. At the onset of EMD, the energy densities of $\Phi$ and radiation are close to equal and we have $\rho_{\Phi,\mathrm{MD}} \approx \rho_{\mathrm{r,MD}} \approx 3H_{\mathrm{MD}}^2 M_{\mathrm{P}}^2$. Similarly, at the end of EMD we have $\rho_{\Phi,\mathrm{R}} \approx \rho_{\mathrm{r,R}} \approx 3\Gamma_\Phi^2 M_{\mathrm{P}}^2$. In the case of initial HS domination, $\rho_{\mathrm{r,MD}}$ is dominated by $\rho_{\mathrm{r,MD}}^{(\mathrm{hid})}$, while for initial VS domination it is dominated by $\rho_{\mathrm{r,MD}}^{(\mathrm{vis})}$. The energy density at reheating in both cases is dominated by the VS because of our decay requirement. Therefore, the ratio of the VS and HS radiation energy densities at reheating is

$$f_{\mathrm{R}} \approx \begin{cases} \dfrac{\Gamma_\Phi^2}{H_{\mathrm{MD}}^2}\left(\dfrac{H_{\mathrm{MD}}}{\Gamma_\Phi}\right)^{8/3} & f_{\mathrm{i}} \ll 1 \\ \dfrac{f_{\mathrm{i}}\Gamma_\Phi^2}{H_{\mathrm{MD}}^2}\left(\dfrac{H_{\mathrm{MD}}}{\Gamma_\Phi}\right)^{8/3} & f_{\mathrm{i}} \gg 1\,, \end{cases} \tag{E.3}$$

where we have included a redshift factor for the HS from reheating to the start of EMD. Therefore we have

$$e_{\mathrm{f}} \approx \left(\frac{H_{\mathrm{MD}}}{\Gamma_\Phi}\right)^{2/3} = \left(\frac{a_{\mathrm{R}}}{a_{\mathrm{MD}}}\right)\,. \tag{E.4}$$

Lastly, we note that $e_{\mathrm{f}}$ can also be approximated as $e_{\mathrm{f}} \approx f_{\mathrm{R}}/(1+f_{\mathrm{i}})$, to smoothly connect the two cases of initial domination.

## E.2 Decoupling of $\Phi$ from either sector via freeze-out

It is useful to obtain an expression for the Hubble rate at the onset of EMD, $H_{\mathrm{MD}}$. we do so by redshifting the frozen number density of $\Phi$ from the freeze-out time to

the start of EMD:

$$n_{\Phi,\mathrm{MD}} = n_{\Phi,\mathrm{f}} \left(\frac{H_{\mathrm{MD}}}{H_{\mathrm{f}}}\right)^{3/2} = \frac{H_{\mathrm{MD}}^{3/2}}{\langle\sigma_\Phi v\rangle\, H_{\mathrm{f}}^{1/2}}\,. \tag{E.5}$$

Noting that we have $m_\Phi n_{\Phi,\mathrm{MD}} \approx 3H_{\mathrm{MD}}^2 M_{\mathrm{P}}^2$ at the onset of EMD, we are left with

$$H_{\mathrm{MD}} \approx \frac{m_\Phi^2}{9\,\langle\sigma_\Phi v\rangle^2\, M_{\mathrm{P}}^4 H_{\mathrm{f}}}\,. \tag{E.6}$$

What remains is to specify $H_{\mathrm{f}}$, which we do below for a number of cases.

**Nonrelativistic freeze-out from HS** – Using the usual freeze-out condition of $n_{\Phi,\mathrm{eq}}\,\langle\sigma_\Phi v\rangle = H_{\mathrm{f}}$, with the nonraltivistic form of the equilibrium number density, we have

$$g_\Phi \left(\frac{m_\Phi^2}{2\pi x_{\mathrm{f}}}\right)^{3/2} \mathrm{e}^{-x_{\mathrm{f}}}\,\langle\sigma_\Phi v\rangle \approx \sqrt{\frac{\pi^2}{90} g_*^{(\mathrm{hid})}(1+f_{\mathrm{i}})}\,\frac{m_\Phi^2}{M_{\mathrm{P}} x_{\mathrm{f}}^2}\,, \tag{E.7}$$

where we have used $H_{\mathrm{f}} \approx \sqrt{\frac{\pi^2}{90} g_*^{(\mathrm{hid})}(1+f_{\mathrm{i}})}\,\frac{m_\Phi^2}{M_{\mathrm{P}} x_{\mathrm{f}}^2}$ with $x_{\mathrm{f}} \equiv m_\Phi/T_{\mathrm{f}}^{(\mathrm{hid})}$. Rearranging yields an expression that can be solved for $x_{\mathrm{f}}$:

$$x_{\mathrm{f}} \approx \ln\left(\frac{3\sqrt{5} g_\Phi\,\langle\sigma_\Phi v\rangle\, m_\Phi M_{\mathrm{P}} x_{\mathrm{f}}^{1/2}}{2\pi^{5/2} {g_*^{(\mathrm{hid})}}^{1/2} (1+f_{\mathrm{i}})^{1/2}}\right)\,. \tag{E.8}$$

The solution to this can then be used in the expression for $H_{\mathrm{f}}$ above to complete its specification in terms of the parameters of our scenario.

**Nonrelativistic freeze-out from VS** – Here we define $x_{\mathrm{f}} \equiv m_\Phi/T_{\mathrm{f}}^{(\mathrm{vis})}$, resulting in

$$g_\Phi \left(\frac{m_\Phi^2}{2\pi x_{\mathrm{f}}}\right)^{3/2} \mathrm{e}^{-x_{\mathrm{f}}}\,\langle\sigma_\Phi v\rangle \approx \sqrt{\frac{\pi^2}{90} g_{*\mathrm{f}}^{(\mathrm{vis})} \left(1+\frac{1}{f_{\mathrm{i}}}\right)}\,\frac{m_\Phi^2}{M_{\mathrm{P}} x_{\mathrm{f}}^2}\,. \tag{E.9}$$

and

$$x_{\mathrm{f}} \approx \ln\left(\frac{3\sqrt{5} g_\Phi\,\langle\sigma_\Phi v\rangle\, m_\Phi M_{\mathrm{P}} x_{\mathrm{f}}^{1/2}}{2\pi^{5/2} {g_{*\mathrm{f}}^{(\mathrm{vis})}}^{1/2} \left(1+\frac{1}{f_{\mathrm{i}}}\right)^{1/2}}\right)\,. \tag{E.10}$$

Otherwise, this case is the same as above.

**Relativistic freeze-out from HS** – In this case, we use the relativistic expression for the equilibrium number density, giving

$$\frac{\zeta(3) g_\Phi m_\Phi^3}{\pi^2 x_{\mathrm{f}}^3}\,\langle\sigma_\Phi v\rangle \approx \sqrt{\frac{\pi^2}{90} g_*^{(\mathrm{hid})}(1+f_{\mathrm{i}})}\,\frac{m_\Phi^2}{M_{\mathrm{P}} x_{\mathrm{f}}^2}\,, \tag{E.11}$$

and

$$x_{\rm f} \approx \frac{\sqrt{90}\zeta(3) g_\Phi \langle\sigma_\Phi v\rangle M_{\rm P} m_\Phi}{\pi^3 {g_*^{\rm (hid)}}^{1/2} (1+f_{\rm i})^{1/2}} \,. \tag{E.12}$$

**Relativistic freeze-out from VS** – In this case, we have

$$\frac{\zeta(3) g_\Phi m_\Phi^3}{\pi^2 x_{\rm f}^3} \langle\sigma_\Phi v\rangle \approx \sqrt{\frac{\pi^2}{90} g_{*\rm f}^{\rm (vis)} \left(1+\frac{1}{f_{\rm i}}\right)} \frac{m_\Phi^2}{M_{\rm P} x_{\rm f}^2} \,, \tag{E.13}$$

and

$$x_{\rm f} \approx \frac{\sqrt{90}\zeta(3) g_\Phi \langle\sigma_\Phi v\rangle M_{\rm P} m_\Phi}{\pi^3 {g_{*\rm f}^{\rm (vis)}}^{1/2} \left(1+\frac{1}{f_{\rm i}}\right)^{1/2}} \,. \tag{E.14}$$

## E.3 Decoupling of $\Phi$ from either sector via freeze-in

Because $\Phi$ is the source of the EMD period, it decouples in the prior RD phase. From Appendix A, we know that freeze-in in a RD period is dominated by the relativistic component and the abundance is set at the initial time. We begin with

$$\frac{d(a^3 n_\Phi)}{dt} = a^3 \langle\sigma_\Phi v\rangle (n_{\Phi,\rm eq}^2 - n_\Phi^2) - a^3 \Gamma_\Phi n_\Phi \,, \tag{E.15}$$

We are interested in the early evolution of the $\Phi$ number density well before it decays in a freeze-in scenario, thus we may drop the decay term relative to the decoupling term above, as well as the actual number density relative to the thermal equilibrium value. Using typical expressions for RD, we have

$$\frac{d(a^3 n_\Phi)}{dH} = -\frac{a_{\rm i}^3 H_{\rm i}^{3/2} \langle\sigma_\Phi v\rangle n_{\Phi,\rm eq}^2}{2H^{7/2}} \,. \tag{E.16}$$

To continue, we must express the temperature dependence of the equilibrium number density in terms of $H$, which is most easily done by specializing to the two decoupling cases.

**Freeze-in from HS** – If $\Phi$ decouples from the HS, we have

$$a_{\rm f}^3 n_{\Phi,{\rm f}} \approx -\frac{90^{3/2}\zeta(3)^2 g_\Phi^2 a_{\rm i}^3 H_{\rm i}^{3/2} \langle\sigma_\Phi v\rangle M_{\rm P}^3}{2\pi^7 {g_*^{(\rm hid)}}^{3/2}(1+f_{\rm i})^{3/2}} \int_{H_{\rm i}}^{H_{\rm f}} \frac{dH}{H^{1/2}}\,, \tag{E.17}$$

which results in a frozen number density of

$$n_{\Phi,{\rm f}} \approx \frac{90^{3/2}\zeta(3)^2 g_\Phi^2 H_{\rm f}^{3/2} \langle\sigma_\Phi v\rangle M_{\rm P}^3 H_{\rm i}^{1/2}}{\pi^7 {g_*^{(\rm hid)}}^{3/2}(1+f_{\rm i})^{3/2}}\,. \tag{E.18}$$

Redshifting this to the beginning of EMD and using $m_\Phi n_{\Phi,{\rm MD}} \approx 3H_{\rm MD}^2 M_{\rm P}^2$, we have

$$H_{\rm MD} \approx \frac{90^3\zeta(3)^4 g_\Phi^4 M_{\rm P}^2 \langle\sigma_\Phi v\rangle^2 m_\Phi^2 H_{\rm i}}{9\pi^{14} {g_*^{(\rm hid)}}^3(1+f_{\rm i})^3}\,. \tag{E.19}$$

**Freeze-in from VS** – If $\Phi$ decouples from the VS, we have

$$n_{\Phi,{\rm f}} \approx \frac{90^{3/2}\zeta(3)^2 g_\Phi^2 H_{\rm f}^{3/2} \langle\sigma_\Phi v\rangle M_{\rm P}^3 H_{\rm i}^{1/2}}{\pi^7 {g_{*{\rm i}}^{(\rm vis)}}^{3/2}\left(1+\frac{1}{f_{\rm i}}\right)^{3/2}}\,, \tag{E.20}$$

and

$$H_{\rm MD} \approx \frac{90^3\zeta(3)^4 g_\Phi^4 M_{\rm P}^2 \langle\sigma_\Phi v\rangle^2 m_\Phi^2 H_{\rm i}}{9\pi^{14} {g_{*{\rm i}}^{(\rm vis)}}^3\left(1+\frac{1}{f_{\rm i}}\right)^3}\,. \tag{E.21}$$

## E.4 Additional parameter constraints for decoupled $\Phi$

We obtain another constrain that must be satisfied in order for the EMD phase caused by the decoupled $\Phi$ to have nonzero duration. If $\Phi$ decouples from the subdominant sector, the value of $f_{\rm i}$ must be such that the decoupled number density is large enough to lead to EMD. Using Eq. (6.30) for an annihilation rate that achieves relativistic freeze-out (which corresponds to the maximum frozen number density and thus longest possible duration for EMD), we require $H_{\rm MD} \gtrsim \Gamma_\Phi$. Using Eq. (E.6) for $H_{\rm MD}$ and Eqs. (E.12) and (E.14) for $x_{\rm f}$ in their respective cases, we have

$$f_{\rm i} \lesssim \left(\frac{30\sqrt{10}\zeta(3)^2 g_\Phi^2 m_\Phi^2}{\pi^7 {g_*^{(\rm hid)}}^{3/2} M_{\rm P}\Gamma_\Phi}\right)^{2/3}\,, \tag{E.22}$$

in the case of decoupling from the HS while the VS is dominant, and

$$f_{\rm i} \gtrsim \left( \frac{\pi^7 {g_{*\rm f}^{(\rm vis)}}^{3/2} M_{\rm P} \Gamma_\Phi}{30\sqrt{10}\zeta(3)^2 g_\Phi^2 m_\Phi^2} \right)^{2/3} , \tag{E.23}$$

in the case of decoupling from the VS while the HS is dominant.

# References


[1] G. Bertone, D. Hooper, and J. Silk.
Phys. Rept. **405**, 279 (2005).

[2] G. Bertone and D. Hooper.
Rev. Mod. Phys. **90**, 045002 (2018).

[3] B. Carr, M. Raidal, T. Tenkanen, V. Vaskonen, and H. Veermäe.
Phys. Rev. D **96**, 023514 (2017).

[4] T. Lin.
PoS 333, 009 (2019). (arXiv:1904.07915 [hep-ph]).

[5] H. Baer, K.-Y. Choi, J. Kim, and L. Roszkowski.
Phys. Rept. **555**, 1 (2015).

[6] D. Hooper.
PoS TASI2018, 010 (2019). (arXiv:1812.02029 [hep-ph]).

[7] M. Tanabashi *et al.* (Particle Data Group).
Phys. Rev. D **98**, 030001 (2018). (28. Cosmic Microwave Background).

[8] M. Tanabashi *et al.* (Particle Data Group).
Phys. Rev. D **98**, 030001 (2018). (23. Big-Bang Nucleosynthesis).

[9] N. Aghanim *et al.* (Planck Collaboration).
arXiv:1807.06209 [astro-ph.CO], (2018). (VI Cosmological Parameters).

[10] E. W. Kolb and M. S. Turner.
*The Early Universe* (Addison-Wesley, Menlo Park, California, 1990).

[11] M. Tanabashi *et al.* (Particle Data Group).
Phys. Rev. D **98**, 030001 (2018). (21. Big-Bang Cosmology).

[12] G. Jungman, M. Kamionkowski, and K. Griest.
Phys. Rept. **267**, 195 (1996).

[13] M. Ackermann *et al.* (Fermi-LAT Collaboration).
Phys. Rev. Lett. **115**, 231301 (2015).

[14] A. Albert *et al.* (Fermi-LAT and DES Collaborations).
Astrophys. J. **834**, 110 (2017).

[15] R. K. Leane, T. R. Slatyer, J. F. Beacom, and K. C. Y. Ng.
Phys. Rev. D **98**, 023016 (2018).

[16] R. Allahverdi, R. Brandenberger, F.-Y. Cyr-Racine, and A. Mazumdar.
Ann. Rev. Nucl. Part. Sci. **60**, 27 (2010).

[17] M. Tanabashi *et al.* (Particle Data Group).
Phys. Rev. D **98**, 030001 (2018). (22. Inflation).

[18] G. Kane, K. Sinha, and S. Watson.
Int. J. Mod. Phys. D **24**, 1530022 (2015).

[19] J. A. Dror, E. Kuflik, and W. H. Ng.
Phys. Rev. Lett. **117**, 211801 (2016).

[20] A. Berlin, D. Hooper, and G. Krnjaic.
Phys. Rev. D **94**, 095019 (2016).

[21] J. A. Dror, E. Kuflik, B. Melcher, and S. Watson.
Phys. Rev. D **97**, 063524 (2018).

[22] M. Cirelli, Y. Gouttenoire, K. Petraki, and F. Sala.
J. Cosmol. Astropart. Phys. **02**, 014 (2019).

[23] G. F. Giudice, E. W. Kolb, and A. Riotto.
Phys. Rev. D **64**, 023508 (2001).

[24] A. L. Erickcek.
Phys. Rev. D **92**, 103505 (2015).

[25] R. Allahverdi and J. K. Osiński.
Phys. Rev. D **99**, 083517 (2019).

[26] S. Kachru, R. Kallosh, A. D. Linde, and S. P. Trivedi.
Phys. Rev. D **68**, 046005 (2003).

[27] V. Balasubramanian, P. Berglund, J. P. Conlon, and F. Quevado.
J. High Energy Phys. **03**, 007 (2005).

[28] K. Choi, A. Falkowski, H. P. Nilles, and M. Olechowski.
Nucl. Phys. B **718**, 113 (2005).

[29] M. Cicoli, C. Mayrhofer, and R. Valandro.
J. High Energy Phys. **02**, 062 (2012).

[30] M. Cicoli, S. Krippendorf, C. Mayrhofer, F. Quevado, and R. Valandro.
J. High Energy Phys. **09**, 019 (2012).

[31] M. Dine, W. Fischler, and D. Nemeschansky.
Phys. Lett. B **136**, 169 (1984).

[32] G. D. Coughlan, R. Holman, P. Ramond, and G. G. Ross.
Phys. Lett. B **140**, 44 (1984).

[33] A. S. Goncharov, A. D. Linde, and M. I. Vysotsky.
Phys. Lett. B **44**, 279 (1984).

[34] M. Dine, L. Randall, and S. D. Thomas.
Nucl. Phys. B **458**, 291 (1996).

[35] B. Carr, T. Tenkanen, and V. Vaskonen.
Phys. Rev. D **96**, 063507 (2017).

[36] R. Allahverdi and J. K. Osiński.
arXiv:1909.01457 [hep-ph], (2019).

[37] K. Redmond and A. L. Erickcek.
Phys. Rev. D **96**, 043511 (2017).

[38] L. Visinelli.
Symmetry **10**, 546 (2018).

[39] C. Maldonado and J. Unwin.
J. Cosmol. Astropart. Phys. **06**, 37 (2019).

[40] M. A. Amin, M. P. Hertzberg, D. I. Kaiser, and J. Karouby.
Int. J. Mod. Phys. D **24**, 1530003 (2015).

[41] N. Bernal, M. Heikinheimo, T. Tenkanen, K. Tuominen, and V Vaskonen.
Int. J. Mod. Phys. A **32**, 1730023 (2017).

[42] K. Harigaya and K. Mukaida.
J. High Energy Phys. **05**, 006 (2014).

[43] M. Drees and F. Hajkarim.
J. Cosmol. Astropart. Phys. **02**, 057 (2018).

[44] M. Kawasaki, T. Moroi, and T. Yanagida.
Phys. Lett. B **370**, 52 (1996).

[45] T. Moroi and L. Randall.
Nucl. Phys. B **570**, 455 (2000).

[46] G. B. Gelmini and P. Gondolo.
Phys. Rev. D **74**, 023510 (2006).

[47] R. Allahverdi, B. Dutta, and K. Sinha.
Phys. Rev. D **83**, 083502 (2011).

[48] A. R. Liddle and S. M. Leach.
Phys. Rev. D **68**, 103503 (2003).

[49] T. Rehagen and G. B. Gelmini.
J. Cosmol. Astropart. Phys. **06**, 039 (2015).

[50] D. I. Podolsky, G. N. Felder, L. Kofman, and M. Peloso.
Phys. Rev. D **73**, 023501 (2006).

[51] K. D. Lozanov and M. A. Amin.
Phys. Rev. Lett. **119**, 061301 (2017).

[52] Y. Akrami *et al.* (Planck Collaboration).
arXiv:1807.06211 [astro-ph.CO], (2018). (X Constraints on Inflation).

[53] D. Roest.
J. Cosmol. Astropart. Phys. **01**, 007 (2014).

[54] R. Allahverdi, K. Dutta, and A. Maharana.
J. Cosmol. Astropart. Phys. **10**, 038 (2018).

[55] R. Durrer and J. Hasenkamp.
Phys. Rev. D **84**, 064027 (2011).

[56] R. Jinno, T. Moroi, and K. Nakayama.
J. Cosmol. Astropart. Phys. **01**, 040 (2014).

[57] F. D'Eramo and K. Schmitz.
Phys. Rev. Research **1**, 013010 (2019).

[58] N. Bernal and F. Hajkarim.
Phys. Rev. D **100**, 063502 (2019).

[59] D. G. Figueroa and E. H. Tanin.
J. Cosmol. Astropart. Phys. **08**, 011 (2019).

[60] R. Allahverdi, B. Dutta, and K. Sinha.
Phys. Rev. D **86**, 095016 (2012).

[61] R. Allahverdi, M. Cicoli, B. Dutta, and K. Sinha.
Phys. Rev. D **88**, 095015 (2013).

[62] R. Allahverdi, M. Cicoli, and F. Muia.
J. High Energy Phys. **06**, 153 (2016).

[63] M. A. G. Garcia, Y. Mambrini, K. A. Olive, and M. Peloso.
Phys. Rev. D **96**, 103510 (2017).

[64] R. Allahverdi, J. Dent, and J. Osinski.
Phys. Rev. D **97**, 055013 (2018).

[65] M. Battaglieri *et al.*
arXiv:1707.04591 [hep-ph], (2017).

[66] B. J. Carr and S. W. Hawking.
Mon. Not. R. Astron. Soc. **168**, 399 (1974).

[67] B. J. Carr.
Astrophys. J. **201**, 1 (1975).

[68] M. Khlopov, B. A. Malomed, and I. B. Zeldovich.
Mon. Not. R. Astron. Soc. **215**, 575 (1985).

[69] A. G. Polnarev and M. Y. Khlopov.
Usp. Fiz. Nauk. **145**, 369 (1985) [Sov. Phys. Usp. **28**, 213 (1985)].

[70] M. Y. Khlopov.
Res. Astron. Astrophys. **10**, 495 (2010).

[71] B. J. Carr K., Kohri, Y. Sendouda, and J. Yokoyama.
Phys. Rev. D **81**, 104019 (2010).

[72] B. Carr, F. Kühnel, and M. Sandstad.
Phys. Rev. D **94**, 083504 (2016).

[73] J. García-Bellido.
J. Phys. Conf. Ser. **840**, 012032 (2017).

[74] S. Bird, I. Cholis, J. B. Muñoz, Y. Ali-Haïmoud, M. Kamionkowski, E. D. Kovetz, A. Raccanelli, and A. G. Riess.
Phys. Rev. Lett. **116**, 201301 (2016).

[75] M. Sasaki, T. Suyama, T. Tanaka, and S. Yokoyama.
Phys. Rev. Lett. **117**, 061101 (2016).

[76] S. Clesse and J. García-Bellido.
Phys. Dark Universe **15**, 142 (2017).

[77] E. D. Kovetz, I. Cholis, P.C. Breysse, and M. Kamionkowski.
Phys. Rev. D **95**, 103010 (2017).

[78] A. M. Green.
Phys. Rev. D **94**, 063530 (2016).

[79] F. Kühnel and K. Freese.
Phys. Rev. D **95**, 083508 (2017).

[80] N. Bellomo, J. L. Bernal, A. Raccanelli, and L. Verde.
J. Cosmol. Astropart. Phys. **01**, 004 (2018).

[81] K. Inomata, M. Kawasaki, K. Mukaida, and T. T. Yanagida.
Phys. Rev. D **97**, 043514 (2018).

[82] G. F. Giudice, M. McCullough, and A. Urbano.
J. Cosmol. Astropart. Phys. **10**, (001 2016).

[83] A. Raccanelli, E. D. Kovetz, S. Bird, I. Cholis, and J. B. Muñoz.
Phys. Rev. D **94**, 023516 (2016).

[84] K. Postnov and A. Kuranov.
IAU Symp. **329**, 118 (2017).

[85] K. Kyutoku and N. Seto.
Mon. Not. R. Astron. Soc. **462**, 2177 (2016).

[86] N. Bartolo *et al.*
J. Cosmol. Astropart. Phys. **12**, 026 (2016).

[87] A. Sesana.
J. Phys. Conf. Ser. **840**, 012018 (2017).

[88] M. Coleman Miller.
Gen. Relativ. Gravit. **48**, 95 (2016).

[89] T. Nakamura *et al.*
Prog. Theor. Exp. Phys. **2016**, 093E01 (2016).

[90] H. Davoudiasl and P. P. Giardino.
Phys. Lett. B **768**, 198 (2017).

[91] I. Cholis.
J. Cosmol. Astropart. Phys. **06**, 037 (2017).

[92] S. Clesse and J. García-Bellido.
Phys. Dark Universe **18**, 105 (2017).

[93] S. Wang, Y.-F. Wang, Q.-G. Huang, and T. G. F. Li.
Phys. Rev. Lett. **120**, 191102 (2018).

[94] T. Nakama, J. Silk, and M. Kamionkowski.
Phys. Rev. D **95**, 043511 (2017).

[95] K. Crocker, T. Prestegard, V. Mandic, T. Regimbau, K. Olive, and E. Vangioni.
Phys. Rev. D **95**, 063015 (2017).

[96] E. D. Kovetz.
Phys. Rev. Lett. **119**, 131301 (2017).

[97] J. García-Bellido, M. Peloso, and C. Unal.
J. Cosmol. Astropart. Phys. **09**, 013 (2017).

[98] T. D. Brandt.
Astrophys. J. **824**, L31 (2016).

[99] S. M. Koushiappas and A. Loeb.
Phys. Rev. Lett. **119**, 041102 (2017).

[100] D. Gaggero, G. Bertone, F. Calore, R. M. T. Connors, M. Lovell, S. Markoff, and E. Storm.
Phys. Rev. Lett. **118**, 241101 (2017).

[101] Y. Inoue and A. Kusenko.
J. Cosmol. Astropart. Phys. **10**, 034 (2017).

[102] L. Chen, Q.-G. Huang, and K. Wang.
J. Cosmol. Astropart. Phys. **12**, 044 (2016).

[103] Y. Ali-Haïmoud and M. Kamionkowski.
Phys. Rev. D **95**, 043534 (2017).

[104] S. Clark, B. Dutta, Y. Gao, L. E. Strigari, and S. Watson.
Phys. Rev. D **95**, 083006 (2017).

[105] Julian Georg and Scott Watson.
J. High Energy Phys. **09**, 138 (2017).

[106] V. Poulin, P. D. Serpico, F. Calore, S.Clesse, and K. Kohri.
Phys. Rev. D **96**, 083524 (2017).

[107] T. Nakama, B. Carr, and J. Silk.
Phys. Rev. D **97**, 043525 (2018).

[108] B. Horowitz.
arXiv:1612.07264 [astro-ph.CO], (2016).

[109] E. Mediavilla, J. Jiménez-Vicente, J. A. Muñoz, H. Vives-Arias, and J. Calderón-Infante.
Astrophys. J. **836**, L18 (2017).

[110] F. Capela, M. Pshirkov, and P. Tinyakov.
Phys. Rev. D **87**, 123524 (2013).

[111] J. B. Muñoz, E. D. Kovetz, L. Dai, and M. Kamionkowski.
Phys. Rev. Lett. **117**, 091301 (2016).

[112] A. Kashlinsky.
Astrophys. J. **823**, L25 (2016).

[113] J.-O. Gong and N. Kitajima.
J. Cosmol. Astropart. Phys. **08**, 017 (2017).

[114] K. Inomata, M. Kawasaki, K. Mukaida, Y. Tada, and T. T. Yanagida.
Phys. Rev. D **95**, 123510 (2017).

[115] K. Schutz and A. Liu.
Phys. Rev. D **95**, 023002 (2017).

[116] N. Orlofsky, A. Pierce, and J. D. Wells.
Phys. Rev. D **95**, 063518 (2017).

[117] G. Chapline and P. H. Frampton.
J. Cosmol. Astropart. Phys. **11**, 042 (2016).

[118] L. Dai, T. Venumadhav, and K. Sigurdson.
Phys. Rev. D **95**, 044011 (2017).

[119] I. Cholis, E. D. Kovetz, Y. Ali-Haïmoud, S. Bird, M. Kamionkowski, J. B. Muñoz, and A. Raccanelli.
Phys. Rev. D **94**, 084013 (2016).

[120] T. Chiba and S. Yokoyama.
Prog. Theor. Exp. Phys. **2017**, 083E01 (2017).

[121] J. García-Bellido and S. Clesse.
arXiv:1710.04694 [astro-ph.CO], (2017).

[122] A. M. Green.
Phys. Rev. D **96**, 043020 (2017).

[123] M. Kawasaki, K. Mukaida, and T. T. Yanagida.
Phys. Rev. D **94**, 063509 (2016).

[124] J. M. Ezquiaga, J. García-Bellido, and E. Ruiz Morales.
Phys. Lett. B **776**, 345 (2018).

[125] S.-L. Cheng, W. Lee, and K.-W. Ng.
J. High Energy Phys. **02**, 008 (2017).

[126] M. Kawasaki, A. Kusenko, Y. Tada, and T. T. Yanagida.
Phys. Rev. D **94**, 083523 (2016).

[127] J. García-Bellido, M. Peloso, and C. Unal.
J. Cosmol. Astropart. Phys. **12**, 031 (2016).

[128] V. Domcke, F. Muia, M. Pieroni, and L. T. Witkowski.
J. Cosmol. Astropart. Phys. **07**, 048 (2017).

[129] K. Inomata, M. Kawasaki, K. Mukaida, Y. Tada, and T. T. Yanagida.
Phys. Rev. D **96**, 043504 (2017).

[130] J. García-Bellido and E. Ruiz Morales.
Phys. Dark Universe **18**, 47 (2017).

[131] K. Kannike, L. Marzola, M. Raidal, and H. Veermäe.
J. Cosmol. Astropart. Phys. **09**, 020 (2017).

[132] M. Drees and E. Erfani.
J. Cosmol. Astropart. Phys. **04**, 005 (2011).

[133] M. Drees and E. Erfani.
J. Cosmol. Astropart. Phys. **01**, 035 (2012).

[134] J. Georg, G. Şengör, and S. Watson.
Phys. Rev. D **93**, 123523 (2016).

[135] J. C. Niemeyer and K. Jedamzik.
Phys. Rev. D **59**, 124013 (1999).

[136] I. Musco, J. C. Miller, and L. Rezzolla.
Classical Quantum Gravity **22**, 1405 (2005).

[137] I. Musco, J. C. Miller, and A. G. Polnarev.
Classical Quantum Gravity **26**, 235001 (2009).

[138] I. Musco and J. C. Miller.
Classical Quantum Gravity **30**, 145009 (2013).

[139] T. Koike, T. Hara, and S. Adachi.
Phys. Rev. Lett. **74**, 5170 (1995).

[140] J. C. Niemeyer and K. Jedamzik.
Phys. Rev. Lett. **80**, 5481 (1998).

[141] T. Harada, C. M. Yoo, and K. Kohri.
Phys. Rev. D **88**, 084051 (2013).

[142] S. W. Hawking.
Commun. Math. Phy. **43**, 199 (1975); **46** 206 (1976).

[143] A. M. Green.
Phys. Rev. D **60**, 063516 (1999).

[144] M. Y. Khlopov, A. Barrau, and J. Grain.
Classical Quantum Gravity **23**, 1875 (2006).

[145] M. Lemoine.
Phys. Lett. B **481**, 333 (2000).

[146] J. B. Muñoz, E. D. Kovetz, A. Raccanelli, M. Kamionkowski, and J. Silk.
J. Cosmol. Astropart. Phys. **05**, 032 (2017).

[147] P. A. R. Ade *et al.* (Planck Collaboration).
Astron. Astrophys. **594**, A20 (2016). (XX Constraints on Inflation).

[148] J. García-Bellido, A. D. Linde, and D. Wands.
Phys. Rev. D **54**, R25 (1996).

[149] G. Germani and T. Prokopec.
Phys. Dark Universe **18**, 6 (2017).

[150] H. Motohashi and W. Hu.
Phys. Rev. D **96**, 063503 (2017).

[151] H. Di and Y. Gong.
J. Cosmol. Astropart. Phys. **07**, 007 (2018).

[152] G. Ballesteros and M. Taoso.
Phys. Rev. D **97**, 023501 (2018).

[153] Y. Shtanov and J. H. Traschen R. H. Brandenberger.
Phys. Rev. D **51**, 5438 (1995).

[154] L. Kofman, A. Linde, and A. A. Starobinsky.
Phys. Rev. Lett. **73**, 3195 (1994).

[155] L. Kofman, A. Linde, and A. A. Starobinsky.
Phys. Rev. D **56**, 3258 (1997).

[156] J. R. Ellis, J. E. Kim, and D. V. Nanopoulos.
Phys. Lett. B **145**, 181 (1984).

[157] M. Y. Khlopov and A. D. Linde.
Phys. Lett. B **138**, 265 (1984).

[158] M. Bolz, A. Brandenburg, and W. Buchmüller.
Nucl. Phys. B **606**, 518 (2001).

[159] R. Blumenhagen, J. P. Conlon, S. Krippendorf, S. Moster, and F. Quevedo.
J. High Energy Phys. **09**, 007 (2009).

[160] R. Allahverdi and A. Mazumdar.
J. Cosmol. Astropart. Phys. **10**, 008 (2006).

[161] P. Burda, R. Gregory, and I. G. Moss.
Phys. Rev. Lett. **115**, 071303 (2015).

[162] P. Burda, R. Gregory, and I. G. Moss.
J. High Energy Phys. **06**, 25 (2016).

[163] J. R. Espinosa, D. Racco, and A. Riotto.
Phys. Rev. Lett. **120**, 121301 (2018).

[164] M. L. Graesser and J. K. Osiński.
in preparation, (2020).

[165] W. H. Zurek.
Nature **317**, 505 (1985).

[166] W. H. Zurek.
Acta Phys. Polon. B **24**, 1301 (1993).

[167] W. H. Zurek.
Phys. Rept. **276**, 177 (1996).

[168] E. N. Parker.
Astrophys. J. **160**, 383 (1970).

[169] M. S. Turner, E. N. Parker, and T. J. Bogdan.
Phys. Rev. D **26**, 1296 (1982).

[170] H. Murayama and J. Shu.
Phys. Lett. B **686**, 162 (2010).

[171] C. G. Callan.
Phys. Rev. D **26**, 2058 (1982).

[172] V. A. Rubakov.
Nucl. Phys. B **203**, 311 (1982).

[173] K. Colwell and J. Terning.
J. High Energy Phys. **03**, 68 (2016).

[174] M. Tanabashi *et al.* (Particle Data Group).
Phys. Rev. D **98**, 030001 (2018). (116. Magnetic Monopoles).

[175] M. Tanabashi *et al.* (Particle Data Group).
Phys. Rev. D **98**, 030001 (2018). (2. Astrophysical Constants).

[176] B. Spokoiny.
Phys. Lett. B **315**, 40 (1993).

[177] M. Joyce.
Phys. Rev. D **55**, 1875 (1997).

[178] P. G. Ferreira and M. Joyce.
Phys. Rev. D **58**, 023503 (1998).

[179] M. Cicoli, K. Dutta, A. Maharana, and F. Quevedo.
J. Cosmol. Astropart. Phys. **08**, 006 (2016).

[180] M. A. G. Garcia and M. A. Amin.
Phys. Rev. D **98**, 103504 (2018).